Low Thrust Augmented Periodic Orbits in the Two- and Three-Body Problems

PhD Thesis

C. S. Arnot

Advanced Space Concepts Laboratory

Department of Mechanical and Aerospace Engineering

University of Strathclyde, Glasgow

October 5, 2018

This thesis is the result of the author's original research. It has been composed by the author and has not been previously submitted for examination which has led to the award of a degree.

Signed:

Date:

Acknowledgements

I would like to offer my sincere thanks to my supervisor, Professor Colin McInnes, for his limitless patience and guidance for the past three and a half (and a bit) years, and to the University of Glasgow's School of Engineering for hosting me as a Visiting Researcher for that time. I am deeply thankful to the University of Strathclyde and the Engineering and Physical Sciences Research Council, without whom I would never have had this opportunity, and to Professor Malcolm Macdonald, Professor James Biggs, and Dr. Robert McKay for their expert support and advice. To those close others who have supported me throughout my time here, advising me, giving technical help, or just lending an ear to my rants, please know that I am truly grateful - you know who you are. All of you have made this possible.

Abstract

Continuous low thrust propulsion can add considerable utility to spacecraft dynamics by enabling rich new families of thrust augmented orbits. With the aim of enabling such orbits for small, low-cost spacecraft with limited on-board sensing, new families of non-Keplerian orbits are generated in the Hill-Clohessy-Wiltshire approximation using position-only feedback.

The same strategy is also applied to the linearised dynamics around collinear libration points in the circular restricted three-body problem. In the Earth-Moon system, position-only feedback is used to stabilise the local dynamics, and interesting new multiply-periodic orbits are generated. The in-plane and out-of-plane natural frequencies are then synchronised, allowing the generation of stable halo-type orbits of arbitrary dimensions. An application for such orbits, an Earth-Moon L_2 communications relay, is also suggested. The propellant requirements for such orbits are shown to be modest and achievable with existing low thrust technology.

Continuous thrust is also used to produce artificial horseshoe orbits in a two-body system. Using the cylindrical-polar form of the Hill-Clohessy-Wiltshire approximation, low thrust manoeuvres are developed which allow for phased, nested constellations of spacecraft around a circular two-body orbit. Interesting new three-dimensional nested constellations can be enabled by the addition of out-of-plane thrust, offering reconfigurable coverage of specific regions of the Earth.

In the circular restricted three-body problem, constant thrust directed along the unit radius vector from each primary mass is applied to a spacecraft, modify-

ing the positions and nature of the five equilibrium points, and thereby changing the region in which horseshoe orbits can occur. In the 243 Ida binary asteroid system, it is found that acceleration directed towards the two primaries results in Lyapunov-stable L_4 and L_5 points, permitting horseshoe orbits.

In the 243 Ida system, a strategy is then proposed for finding periodic horseshoe orbits which rendezvous with the surface of the smaller primary. A search-and-filter method is employed to produce initial guesses for periodic horseshoe orbits, and these guesses are then refined using a numerical shooting method to find precisely periodic orbits. However, this method misses periodic orbits with more than two crossings of the axis connecting the primaries, and is therefore modified to provide guesses for horseshoe orbits with additional crossings. Using this strategy, two thrust augmented horseshoe orbits which rendezvous with the surface of the smaller primary are found, and the speed of the spacecraft at rendezvous is shown to be small. Such orbits offer interesting new opportunities for binary asteroid touch-and-go sampling.

Acronyms

AEP . . . . . Artificial Equilibrium Point

CRTBP . . . . . Circular Restricted Three-Body Problem

HCW . . . . . Hill-Clohessy-Wiltshire

NKO . . . . . Non-Keplerian Orbit

SEP . . . . . Solar Electric Propulsion

Contents

List of Figures

List of Tables

Chapter 1

Introduction

In this Thesis, a rich range of new types of orbits is generated through the application of continuous thrust in both the two-body Hill-Clohessy-Wiltshire (HCW) approximation and the circular restricted three-body problem (CRTBP). This Chapter presents a literature review of topics which provide a background and inspiration for this Thesis, including displaced non-Keplerian orbits, artificial equilibria, thrust augmented spacecraft relative motion, low thrust propulsion technology, and co-orbital motion in the CRTBP. Novel mission concepts are also described and scenarios are identified for which interesting new mission applications can be enabled. Emerging from this review, the objectives of the Thesis are defined in Section 1.3, and the Thesis structure and author's related publications are given in Chapter-by-Chapter form in Section 1.4.

1.1 Literature Review

1.1.1 Artificial Equilibria and Non-Keplerian Orbits

This Thesis will build upon the basic concept of using continuous thrust-induced acceleration to force spacecraft to follow orbits which would be impossible under natural, free-flying conditions. This concept has been considered by many past authors, and certain key advances relevant to this Thesis are presented in

this Subsection. More specifically, two branches of this concept, artificial equilibrium points (AEPs) and non-Keplerian orbits (NKOs), are described, and their relevance to this Thesis is defined.

Artificial Equilibria

In a dynamical system, equilibrium points are locations at which all forces acting upon a particle are balanced, such that a particle would remain stationary if it were placed precisely at one of these equilibria with zero initial velocity. Many dynamical systems, such as the CRTBP, naturally contain such equilibria [1]. However, if additional forces, such as thrust, are artificially added to a dynamical system, the locations of the equilibria may change or new equilibria may be generated. These new points are termed *artificial equilibrium points*.

In the restricted three-body problem, Dusek first proposed that AEPs could be created in the vicinity of libration points using continuous thrust [2]. Since then, many authors have investigated the generation of AEPs in three-body systems. Notably, McInnes et. al investiated the generation of AEPs in the CRTBP using solar sails, finding that the five natural libration points are part of a surface of AEPs parameterised by solar sail mass relative to area [3], and Morimoto et al. investigated the thrust requirements to turn any arbitrary point in a restricted three-body system into an AEP, finding the regions of stable AEPs in small mass-ratio systems, such as the Sun-Earth system, which are achievable with small control accelerations [4].

Later, Baig and McInnes studied the generation and nature of AEPs in the CRTBP using a combination of solar sails and solar electric propulsion (such as electrostatic ion thrusters), allowing for free selection of the sail lightness number (the ratio of maximum spacecraft acceleration to the Sun's local gravity) while minimising propellant use, finding that hybrid propulsion required much lower propellant mass than purely solar electric propulsion, and a smaller initial spacecraft mass than either a solar sail or solar electric spacecraft for a polar observa-

tion mission [6]. Bombardelli and Peláez investigated the stability of AEPs under minimum control in the CRTBP, showing that equilibrium is, in systems where the masses of the primaries are different by an order of magnitude, achievable when the spacecraft is nearly co-orbiting with the smaller primary. Furthermore, they showed that stability is achieved when the spacecraft's distance from the smaller primary is greater than a minimum value given by a function of the mass ratio and separation of the primaries [7]. Aliasi, Mengali, and Quarta investigated the generation of AEPs using a generalised sail model (which describes any propulsion system with only radial thrust which varies with distance from the central body) in the elliptic restricted three-body problem, finding that the AEPs exist only in the orbital plane of the primaries, and that the sail must periodically vary its acceleration to maintain any particular AEP [8]. In recent years, Lei and Xu studied invariant manifolds around unstable AEPs in the CRTBP, and used high-order series expansions of the manifolds to design transfer trajectories from the larger primary to the artificial L_1 and L_2 points [9]. De Almeida et al. investigated the use of a solar sail for displacing a spacecraft above or below the Sun-Earth L_3 point [10] and described the motion of a spacecraft around an AEP under perturbations [11]. Yang, Bai, and Li investigated the generation of AEPs close to an irregularly-shaped asteroid, linearising the motion close to the AEPs and deriving the pseudo-potential function for the system for topological and stability analysis [12]. This particular method will also be employed in Chapter 6 of this Thesis to analyse the effects of continuous thrust on the topology of the pseudo-potential of the CRTBP.

Non-Keplerian Orbits

Keplerian orbits, having the shape of a conic section with the barycentre of the two-body gravitational system at one of the section's foci, can be modified with continuous thrust to become non-Keplerian orbits. That is, the plane of the orbit can be artificially displaced using out-of-plane thrust such that it no longer con-

tains the barycentre. As such, NKOs are a closely-related concept to AEPs, since a displaced orbit can appear as an AEP in a rotating frame of reference. Displaced orbits could find useful application as displaced communications relays, avoiding occultation by bodies in the orbit plane (as first proposed by Forward [13]), or as displaced polar observation platforms (as proposed by McInnes [3,14]). Displacing the plane of an orbit in such a way was also suggested by Austin et al. for small displacements [15], and explored more prominently by Nock for in-situ observation of Saturn's rings [16]. Yashko and Hastings analysed the propulsion system requirements for satellite formations using NKOs [17], and McInnes investigated the existence and stability of displaced NKOs in the two-body problem [18] and the stability and control of such orbits [19], while Scheeres considered the stability of NKOs about small bodies [20]. Later, Xu and Xu performed analysis of the nonlinear dynamics of NKOs around a planet [21], Ceriotti and McInnes proposed sail-displaced NKOs for polar coverage of the Earth [22], and more recently McKay et al. performed a comprehensive survey of NKOs and their utility [23]. Of these authors, only Austin et al. considered the case of small displacements for spacecraft proximity operations, and no analysis of this problem was performed. Chapter 3 of this Thesis will build upon this concept by generating new types of thrust augmented NKOs in the linear HCW approximation of spacecraft motion relative to a circular two-body orbit, for the purposes of spacecraft formation flight and specific applications therein. Additionally, the work which is most influential on the derivation of the new non-Keplerian orbit types presented in this Thesis is that of McInnes [18], concerning the existence of NKOs in the two-body problem. The survey performed by McKay et al. [23] also serves as inspiration for the mission applications of the thrust augmented orbits generated, in Chapters 3 and 4.

As has been described, the mission applications of NKOs and AEPs depend on the existence of suitable propulsion technologies, such as solar sails, electric sails, and solar electric propulsion. These technologies are described in the following

Subsection.

1.1.2 Continuous Low Thrust

Non-Keplerian orbits and artificial equilibria require the application of continuous thrust-induced acceleration. While conventional chemical propulsion offers high thrust and low specific impulse, requiring operation in discreet impulses and essentially prohibiting such orbits, other propulsion technologies exist which offer continuous low thrust with relatively small or zero propellant expenditure. This Subsection broadly describes three such technologies (solar sails, electric sails, solar electric propulsion), along with their applicability to NKOs and AEPs. The decision to assume the use of generic low thrust propulsion throughout this Thesis is also described, and the choice of thruster parameters when performing propellant calculations is justified.

Solar Sails

Solar sails (which exploit solar radiation pressure for thrust) can be considered well suited to the maintenance of NKOs and AEPs since they provide continuous low thrust with no propellant requirement. For example, their use for the generation of non-Keplerian geostationary orbits was considered by Forward [5], Baig and McInnes [6], and Heiligers [24]. However, despite the zero propellant and power requirement, solar sails possess a number of inherent disadvantages. Solar sails cannot, for example, produce a thrust component directed towards the Sun, and although demonstrative missions have taken place (e.g. JAXA's IKAROS [25] and NASA's NanoSail-D2 [26]) the use of solar sails as primary spacecraft propulsion is limited by existing materials technology: reflectivity and mass relative to sail area govern the maximum acceleration which can be imparted to the spacecraft. Furthermore, the thrust produced by a solar sail decreases with distance from the Sun, and although the sail attitude can be varied to modify the direction of the thrust vector, this also varies the magnitude of the thrust [14].

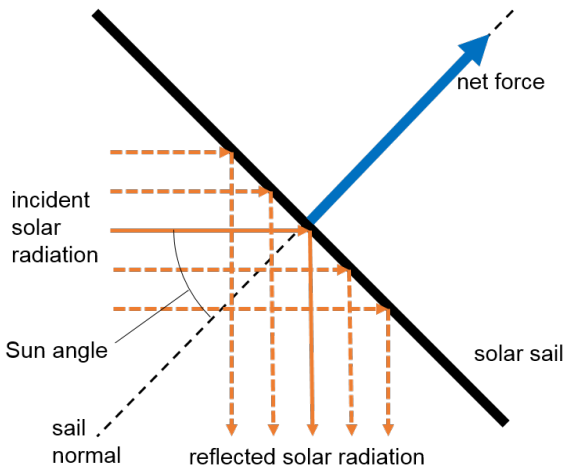

Figure 1.1: Basic principle of operation of a perfectly reflecting solar sail [14].

This in turn limits the regions of AEPs and types of NKOs which can be accessed by a spacecraft equipped only with a solar sail. A schematic which shows the basic principle of operation of a solar sail is given in Fig. 1.1, for a perfect reflector. It should be noted that perfect reflectors do not exist, and a portion of the incident solar radiation will be absorbed by the sail. This absorption causes an additional force coincident to the solar radiation, i.e. directly away from the Sun [14].

For the purposes of this Thesis, the inability to generate a component of thrust directed towards the Sun places too great a limitation on the analysis which will be performed, and so solar sails are not considered as the means of propulsion herein.

Electric Sails

Electric sails, first proposed by Janhunen [27], differ from solar sails in that they operate by using an electric field to gather momentum from solar wind charged particles instead of by exploiting solar radiation pressure. A schematic of an electric sail is shown in Fig. 1.2, where the rotation of the spacecraft is used to deploy and maintain the radial configuration of the wires. Although the dynamic pressure offered by the solar wind is three orders of magnitude smaller than that

of solar radiation pressure at 1 AU, the effective area of the electric sail could be made far larger than a solar sail with equal mass. This is due to the electric sail consisting of radially placed wires, each generating a surrounding electric field which extends into and interacts with the charged solar wind. The performance of such sails in comparison to solar sails was first analysed by Mengali, Quarta, and Janhunen [28], finding that for a given interplanetary mission the electric sail potentially offers greater payload mass fraction, and greater thrust magnitude at a given distance from the Sun. Electric sails were subsequently proposed by Mengali and Quarta as a means of accessing NKOs [29], specifically for solar polar observation. Recently, Wang et al. developed a new methodology for the analysis of the formation flight of electric sails operating in NKOs, and proposed a control strategy for such sail formations [30, 31]. Electric sails, however, possess similar limitations to solar sails, including that they cannot produce a component of thrust directed towards the Sun. An additional disadvantage is that they cannot operate within a planet's magnetosphere [27], and so cannot be used in proximity to the Earth.

Similarly to solar sails, the limitations described above are considered too great for the kind of generalised derivations in this Thesis, and so electric sails will also not be assumed as the spacecraft's means of propulsion. A more generic form of low thrust propulsion is therefore sought, which can point and produce thrust equally in all directions.

Solar Electric Propulsion

The pointing limitation of solar and electric sails is absent from electric propulsion such as electrostatic ion thrusters. This type of propulsion electrically accelerates inert propellants such as Xenon to very high exhaust velocities to offer high specific impulse, with low thrust output and high electrical power requirements [32]. For example, the QinetiQ T5 ion thruster produces thrust in the $5-25$ mN range, with specific impulse of $1900-3000$ s, for a power input of $200-700$ W [33]. A

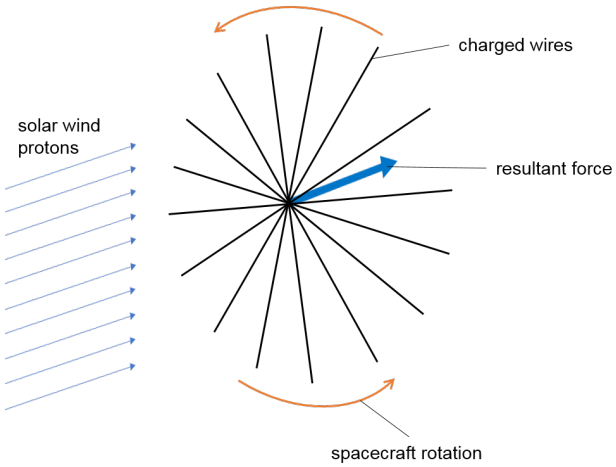

Figure 1.2: Schematic of an electric sail, where the rotation of the spacecraft is used to maintain the radial configuration of the charged wires [27].

schematic of the operation of a gridded electrostatic ion thruster is shown in Fig. 1.3. An electron gun (hollow cathode) is used to bombard the Xenon propellant and strip it of electrons, and the resulting positive ions are accelerated electrostatically between two oppositely charged grids. The electrons emitted by the internal electron gun are collected by the anode (positively charged) grid, and the positive ions in the exhaust are then neutralised by a second, external electron gun to avoid charge imbalance with the body of the spacecraft [35]. Power is normally generated by solar photovoltaic cells, and so this form of propulsion is often termed *solar electric propulsion* (SEP). The dependence on photovoltaic power is perhaps the primary disadvantage of electric propulsion, since photovoltaic panels of considerable mass must be carried and since the available power decreases with distance from the Sun. Furthermore, although the requirement is relatively small, such propulsion still requires propellant.

As stated earlier, the use of hybrid solar sail-solar electric propulsion has also been considered by a number of authors for the generation of NKOs and AEPs (e.g. [24], [6]), to expand the regions of available orbits by permitting a component of thrust in the direction of the Sun. Such propulsion benefits from reduced propellant expenditure and correspondingly longer mission lifetimes when

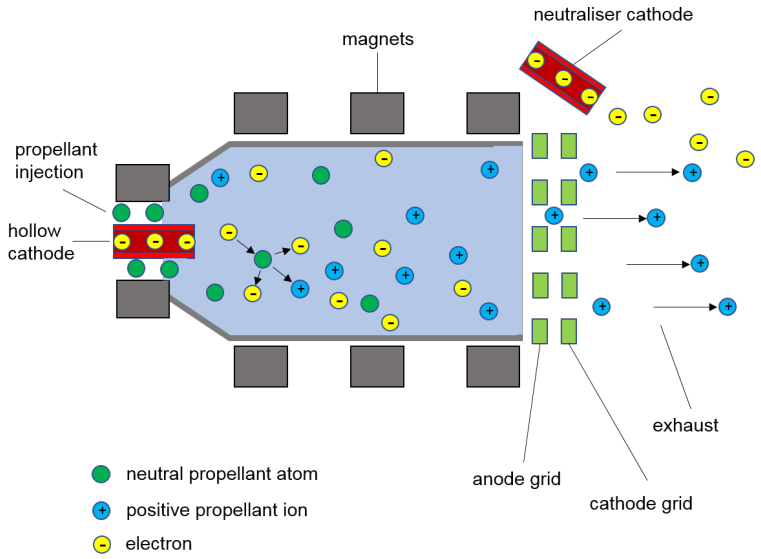

Figure 1.3: Schematic of a gridded electrostatic ion thruster, where electron bombardment is used to ionise a propellant which is then accelerated by the charged grids. The magnets surrounding the plasma generator enhance the efficiency of the ionisation process [35].

compared with pure solar electric propulsion. However, in this Thesis, the use of generic low thrust propulsion which can point and thrust in any direction will be assumed in order to simplify the derivation and generalise the analysis of new orbit types. Propellant expenditure calculations will be made by assuming the use of electrostatic ion thrusters with a specific impulse of 3000 s, comparable to the QinetiQ T5 thruster [34]. It will be assumed that this type of thruster can be precisely throttled, since many of the new thrust augmented orbit types require acceleration which is proportional to position and since the spacecraft's mass will change with propellant expenditure. Furthermore, in practice, the specific impulse of electrostatic ion thrusters varies with the thrust output [34]. This particular behaviour will be neglected in this Thesis.

1.1.3 Spacecraft Relative Motion and Formation Flight

This Thesis will consider, amongst other concepts, the use of continuous low thrust to augment the relative motion between two spacecraft for the purposes

of formation flight. This Subsection describes the basic concept of formation flight and gives an overview of the advances in guidance and control of spacecraft formations, indicating how the work in this Thesis relates to and builds upon these advances.

The NASA Goddard Space Flight Center (GSFC) defines formation flight as "the tracking or maintenance of a desired relative separation, orientation, or position between or among spacecraft [36]." The need for coordinated proximity operations between spacecraft was initially driven by the goal of on-orbit rendezvous and docking. Although Clohessy and Wiltshire had already proposed a guidance strategy for such a rendezvous in 1960 [37], on-orbit rendezvous remained a challenge and was not successfully attempted until the Gemini 6 spacecraft rendezvoused with Gemini 7 in 1965. Difficulties encountered during previous rendezvous attempts were primarily due to the unintuitive nature of the relative orbital mechanics when compared with aircraft formation flight, since thrust towards or away from a target in a similar orbit will also change the chaser's altitude. It was noted by the Gemini 4 crew, who failed in their manual attempt to rendezvous with a spent booster, that "it keeps falling, it's probably three or four miles away, and we just can't close on it," despite spending half of their orbit and attitude maintenance propellant during the attempt [38]. Proper rendezvous procedures were developed shortly thereafter, with the result that Gemini 6 performed a rendezvous and remained close to Gemini 7 for approximately 20 minutes by performing station-keeping manoeuvres [39], in effect becoming the first mission to demonstrate spacecraft formation flight.

Perhaps one of the earliest recognitions of the potential utility of spacecraft formation flight, beyond the scope of spacecraft rendezvous and docking, was a space-based interferometer proposed by Sholomitsky, Prilutsky, and Rodin [40]. A similar concept was also proposed by Labeyrie [41], and the space-based interferometer concept has perhaps most prominently been developed in the form of ESA's Laser Interferometer Space Antenna (LISA) mission (due to launch in

2034), which will consist of three spacecraft flying in a precise equilateral triangle with sides 2.5 million km long in order to detect and measure gravitational waves [42,43], and the technology demonstration mission which precedes it (LISA Pathfinder, launched in 2015) [44]. In the nearer term, ESA's third Project for On-Board Autonomy (PROBA-3) mission (due to launch in 2020) aims to use a two-spacecraft formation to perform solar coronagraphy: one spacecraft will precisely occult the Sun, while the other images the solar corona [45]. Furthermore, several missions demonstrating formation flight have flown in recent years, including the ESA Cluster II (launched in 2000) and NASA Magnetospheric Multiscale (launched in 2015) missions, both of which perform measurements of the Earth's magnetosphere using a four-spacecraft tetrahedral formation [46, 47]. Both of these formations fly on highly elliptical orbits and maintain a tetrahedral formation throughout, while the Chapter of this Thesis which concerns spacecraft formation flight (Chapter 3) assumes a circular reference orbit and generates thrust augmented orbits which offer dynamic formations.

The guidance and control of many different formation flying concepts have been comprehensively surveyed for applications such as hyperspectral sensing (the collection of information from a wide range of the electromagnetic spectrum) and fractionated spacecraft (a formation of spacecraft, in which each individual spacecraft performs the function of one or more subsystems of a traditional spacecraft, allowing robustness to equipment failures and operational flexibility) [48,49]. Until recent years, such concepts have generally assumed the use of conventional chemical propulsion for relative motion control through the application of discrete impulses. The low specific impulse and high thrust offered by this type of thruster impose limitations on spacecraft formations, since the available Δv is low and the spacecraft is restricted to following free-flying trajectories between impulses. It has therefore been proposed that the continuous low thrust offered by modern electrostatic thrusters could add versatility to spacecraft formation flight [15]. The thrust required for formation keeping is generally small, and so several con-

cepts for efficient electrostatic microthrusters have been developed [32, 50]. As an alternative, formation control using inter-spacecraft Coulomb forces has been investigated by several authors (e.g. [51–54]). Other authors considered the use of active control to stabilise the motion of a spacecraft relative to a reference halo orbit in the Hill and restricted three-body problems, notably producing a circular relative trajectory with applications in formation flight for stellar interferometry [55, 56], and later, Cielaszyk and Wie presented a numerical method for halo orbit determination, designing a linear state-feedback controller in which nonlinearities are considered as persistent disturbance inputs, for computing a fuel-efficient nominal path around a libration point [57]. Actively controlled formation flight in a two-body system has also been considered by several authors, such as Bando and Ichikawa [58], where full-state feedback control has been used to force a spacecraft onto an arbitrary singly-periodic reference orbit relative to an elliptical orbit. Similarly, Arnot et al. used position-only feedback instead of full-state feedback to modify the natural frequencies of linearised spacecraft motion relative to a circular two-body reference orbit, resulting in the generation of multiply and singly-periodic relative orbits with applications such as on-orbit inspection [59,60]. The same method was also applied to generate stable multiply-periodic relative orbits around a collinear libration point using continuous thrust [61]. This work will form the core of Chapters 3 and 4, where a range of new spacecraft orbits for formation flight will be derived.

1.1.4 Halo Orbits and Co-orbital Motion

A further concept which will be explored in this Thesis is the use of continuous thrust to augment the motion of a spacecraft which is orbiting within the CRTBP. This Subsection defines halo orbits and co-orbital motion, and indicates how this Thesis will build upon these concepts through the addition of thrust.

A schematic of the CRTBP is given in Fig. 1.4, indicating the relative positions of the two primary masses and the five libration points. The CRTBP is

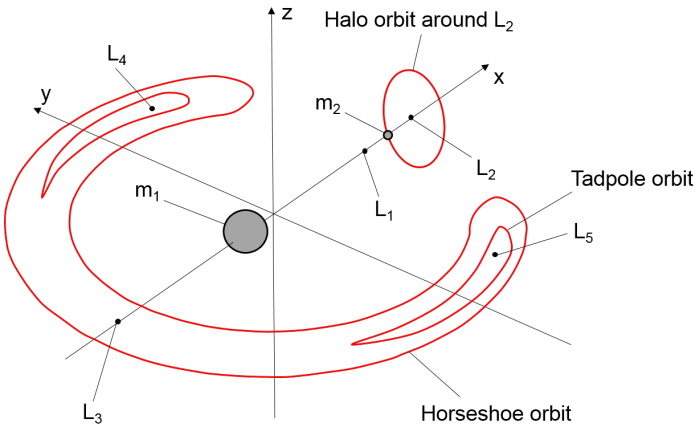

Figure 1.4: Schematic of the CRTBP, including horseshoe, tadpole, and halo orbits.

a frame of reference which rotates about the mutual centre of mass of the two primaries. Three kinds of orbits are also shown: *halo*, *tadpole*, and *horseshoe* orbits. Halo orbits are families of periodic orbits around the collinear libration points (L_1, L_2, or L_3), first derived analytically by Farquhar [62] who proposed that they be used for a lunar far-side communications relay. Howell performed a numerical analysis of these orbits, discovering that families of halo orbits exist for all mass ratios and that certain ranges of these were also stable [63]. A number of halo-orbiting missions have flown, the first being NASA and ESA's International Sun-Earth Explorer-3/International Cometary Explorer (ISEE-3/ICE, launched in 1978) which was placed in orbit around the Sun-Earth L_1 point [64], and more recently the LISA Pathfinder mission which was also placed into a halo orbit around Sun-Earth L_1 [44]. The use of conventional propulsion with discreet impulses is normally assumed for the control and maintenance of these orbits, and the use of continuous low thrust for the generation of new halo orbits has been investigated by some authors (e.g. Baig [96]), however the use of thrust proportional to position relative to a libration point has apparently not been considered. Inspired by this, in Chapter 4 of this Thesis, the thrust-induced acceleration required to synchronise the in-plane and out-of-plane frequencies of motion of a spacecraft around a collinear libration point will be derived in order to produce

halo-type orbits of arbitrary dimensions.

Tadpole and horseshoe orbits are forms of *co-orbital motion*, which can be defined as the motion of one or more small bodies under their mutual gravitational influence and that of two massive primaries, where the inertial-frame orbit period of the small bodies is close to or the same as that of the two primaries' mutual orbit. Such motion has been investigated for more than a century by many authors, initially due to observation of the librations of the Trojan asteroids around the L_4 and L_5 points of the Sun-Jupiter system. These objects offered the only real examples of motion of this kind, and so authors primarily considered tadpole orbits (encircling only L_4 or L_5) which the Trojans followed. A related class of orbits, called horseshoe orbits (encompassing L_3, L_4, and L_5), were also predicted to exist in the CRTBP [65–67], but their existence was not confirmed until the Voyager mission observed the two co-orbiting satellites of Saturn, Janus and Epimethus, following such orbits [68–70].

The detailed dynamics of horseshoe and tadpole orbits were principally investigated by Dermott and Murray, who proposed a method for estimating the long-term stability of such orbits by considering that a particle in such an orbit would be lost due to a random walk of the semi-major axis of the orbit after each pair of encounters with the smaller primary, and provided a function for the time scale in which this would occur. It was suggested that systems with very small mass ratios could maintain horseshoe orbits for long time scales, and that systems with larger mass ratios could maintain satellites in horseshoe orbits for far shorter time scales (such as the Sun-Jupiter system, for approximately 10^6 years), which could account for the lack of Trojan asteroids with horseshoe orbits [71, 72]. This definition of stability is not the same as that which will be used throughout this Thesis, since herein it is generally used to mean stability (in the sense of Lyapunov) of the linearised dynamics around an equilibrium point. In Chapter 6 of this Thesis, the work of Dermott and Murray will be combined with that of Dusek [2], to show how the existence of horseshoe orbits is linked to

the positions and stability nature of the five equilibrium points in the CRTBP, and how the application of conservative acceleration in the form of continuous thrust changes these points and therefore the domain of existence of horseshoe orbits.

Other authors have investigated families of periodic horseshoe orbits (e.g. [73–75]) using numerical methods resembling that proposed by Howell [63]. These numerical methods will serve as a foundation for the numerical search for thrust augmented horseshoe orbits in the CRTBP in Chapter 7 of this Thesis. Simplified models exploiting the apparent symmetry of the CRTBP to compute periodic horseshoe orbits were proposed by Broucke and Konopliv [76], who also noted the similarity of certain aspects of the CRTBP in polar coordinates to the HCW approximation. This served as inspiration for Arnot and McInnes, who used low-thrust transfers to replicate certain aspects of co-orbital motion in the cylindrical-polar HCW approximation in order to produce nested artificial horseshoe orbits for phased constellations of spacecraft [77]. This particular work will form the core of Chapter 5, where the full derivation of the new orbits will be detailed.

1.1.5 Small Spacecraft

The concept of small spacecraft is also central to this Thesis, since a major motivation for the strategies for generating new orbit types is the technological limitations which such spacecraft face. This Subsection describes the concept of small spacecraft, giving examples of the current mission applications and technological challenges faced by such spacecraft.

CubeSats are miniaturised spacecraft composed of multiples of $10 \times 10 \times 10$ cm, 1 kg, units, such that, for example, a 3U CubeSat consists of three such units. They therefore generally belong to the category of *nanosatellites* (spacecraft with a wet mass of 1 to 10 kg), and due to their use of off-the-shelf components they have offered cost-effective space access for not only the on-orbit testing and qualification of space hardware, but also for universities and developing nations to

develop their own space programs [78]. The number of CubeSat launches per year is increasing, aided by the miniaturisation of technology and new design approaches, including more efficient launch strategies for constellations [79]. Recent successful nanosatellite missions such as SMDC-ONE (US Army) [80], the CanX series (University of Toronto) [81, 109, 131], STRaND-1 (University of Surrey/SSTL) [82], and WNISAT (Weathernews Inc.) [83] have demonstrated how such spacecraft can operate individually, while large constellations of nanosatellites have also been successfully proven (e.g. the Planet Labs Flock constellation [84]) with further constellations planned (e.g. the Sky and Space Global 200-satellite telecommunications constellation [85]).

However, the small size and mass of nanosatellites still pose design challenges. Computing power is often limited when compared with larger satellites, and the relatively low budget associated with most nanosatellite missions also ultimately limits the complexity and functionality of flight hardware. The development of thrust augmented orbits for small spacecraft should therefore take into account the limitations of such spacecraft. Miniaturised electrostatic thrusters for nanosatellite applications already exist [50], and so the application of continuous thrust to such spacecraft is feasible.

In this context, new families of orbits which have only simple pointing requirements (these pointing requirements will herein be termed *steering laws*, and they will indicate the direction in which the spacecraft must apply thrust) will have value, particularly if the sensing and control of such orbits can be accomplished with simple and well-established hardware. For example, using a camera and computer vision, it is possible to accurately measure the distance and relative attitude between a chasing nanosatellite and a target,using strategies such as the relative state estimator designed for this purpose by Tweddle and Saenz-Otero and tested with a monochrome camera on the Synchronised Position, Hold, Engage, and Reorient Experimental Satellites (SPHERES) aboard the International Space Station [86]. Sansone et al. also demonstrated the concept more recently

using an infra-red camera, however this particular approach required the use of a light source on the chase spacecraft and retro-reflective markers on the target, and as such was only demonstrated at very close range (¡1 m). Within operating range, the system achieved a relative position accuracy of better than 5 mm, and a relative attitude accuracy of between 2° and 5° [87]. Furthermore, computer vision based systems operate by analysing individual images at discrete time steps, such that estimation of linear and angular velocities presents a difficult challenge. Computer vision-based systems are therefore well suited to applications such as on-orbit inspection and servicing, however applications with higher accuracy requirements and greater separation between spacecraft (such as stellar interferometry or hyperspectral sensing by a formation of spacecraft) will require the use of different relative position and attitude determination systems.

Despite the challenges in obtaining high accuracy, cameras are still a versatile choice of sensor for a small spacecraft with stringent mass limitations. For an application such as on-orbit inspection, a camera could perform three functions: observation of the target, attitude determination, and relative position determination. Additionally, the challenges inherent in rate estimations will be avoided throughout this Thesis through the assumption of position-only feedback control, allowing implementation aboard camera-equipped spacecraft, and only the radial unit vectors from the two primary masses of the CRTBP will be required for the steering laws in Chapters 6 and 7.

1.2 Research Motivation

In 2010, NASA published a detailed study of on-orbit servicing, concluding that on-orbit servicing infrastructure was an essential and economical supporting step for future space missions [88]. It can also be concluded that on-orbit inspection is a necessary precursor to servicing, since it would allow for advance detection and identification of failures on-board a satellite. In geostationary orbit, for example,

many satellites could be inspected by a single small satellite, or formations of small satellites, in order to determine the need for servicing. Woffinden proposed a number of free-flying strategies for on-orbit inspection in which the natural relative motion between target and chase spacecraft are exploited [89], and Erdner proposed [92] a 15 nanosatellite constellation capable of inspecting the entire geostationary ring in less than a single year for space situational awareness. However, the necessity of ballistic orbits imposes limitations on inspection mission concepts. It is proposed in this Thesis that these limitations can be effectively addressed with the introduction of continuous low thrust.

One major limitation of ballistic formation flight in two-body orbits is that both the in-plane and out-of-plane oscillations of a spacecraft have the same natural period, which is equal to the period of the formation target's orbit. By making the system closed-loop and applying controlling thrust, it is possible to modify these natural periods. Due to the decoupling of the in-plane and out-of-plane motion for small displacements, it is possible to engineer a case where the periods are distinct, and to cause the spacecraft to follow, as an example, a helical trajectory around a target. Such a trajectory would be advantageous for on-orbit inspection as it would allow for a detailed three-dimensional sweep of a target. Science missions employing hyperspectral imaging or interferometric sensing could also benefit from such trajectories, as a formation of lenses could be made to rotate around a sensing unit, deriving a scanning ability from a plurality of small satellites instead of a larger, more costly single spacecraft. However, such applications would require greater relative navigation sensing accuracy than cameras can provide, due to the need for accurate scientific measurement baselines. A number of authors have proposed relative navigation systems with greater accuracy, such as Lee et al. who proposed relative navigation with combined laser and smoothed GPS range measurements, finding angular measurement accuracy of greater than 0.001° at distances of more than 30 km [90], or the system proposed by Renga et al. which combines carrier-phase differential GPS with local

inter-spacecraft range measurements, yielding sub-centimetre accuracy for formation baseline separations of 1-2 km [91].

Past authors have generally used a top-down engineering approach, designing active controllers which force a spacecraft onto a pre-determined reference trajectory (e.g. [55, 56, 58]). In this Thesis, it is instead proposed to generate rich new families of orbits without a reference trajectory. For the motion of a spacecraft relative to a target on a two-body orbit, it is proposed here that position-only feedback can be used to modify the natural frequencies of the linearised dynamics by directly manipulating the system eigenvalues, thereby producing novel and interesting stable relative orbits. As described in Section 1.1.5, the use of position-only feedback instead of full state feedback would allow for relative sensing using only a camera and on-board image processing. This assumption is justified by the goal of providing access to useful new trajectories for small, low-cost spacecraft. The use of position-only feedback mitigates the difficulties in implementing accurate relative velocity sensing on-board such a spacecraft, and also avoids the need for estimating the time derivative of the position (a method which is inherently prone to noise errors), whilst still enabling interesting new relative orbits.

Furthermore, it is proposed that the concept of using position-only feedback to modify the natural frequencies of motion can also be applied to the circular restricted three-body problem. Though the problem is normally nonlinear, the motion of a spacecraft in proximity to a libration point can be linearised, and therefore thrust proportional to position can be implemented. This can be used both to force the system to become linearly stable and to modify the natural frequencies of spacecraft librations. Additionally, it is proposed that the in-plane and out-of-plane motion can be coupled to yield a singly-periodic halo-type orbit of arbitrary dimensions around the libration point, which could find application in providing a constantly visible communications relay for lunar far-side missions if applied to the Earth-Moon L_2.

The use of continuous low thrust for spacecraft relative motion need not be

limited to proximity operations. Further utility can be derived from this concept in the form of nested constellations of small spacecraft around a central orbit, for example the geostationary ring, to provide concentrations of spacecraft over certain longitudes at particular times according to demand. Inspiration for such phased constellations is drawn from past authors who proposed reconfigurable constellations [98, 99], and from co-orbital horseshoe orbits in the CRTBP, where an object is transferred between a higher and lower orbit periodically by the gravitational influence of the smaller primary mass. If continuous low thrust is substituted for this gravitational influence, then it is proposed that certain aspects of horseshoe orbits can be replicated in a two-body system for the purposes of providing interesting new phased constellations.

The concept of a small spacecraft equipped with low thrust propulsion and cameras for attitude sensing can be extended to include deep space exploration missions. While co-orbital motion in the presence of continuous thrust, unlike the zero-thrust case, is a largely unexplored problem, it can be envisaged that the addition of thrust could make horseshoe orbits operationally advantageous for certain mission architectures. For applications such as binary asteroid surface sampling, it is proposed that low thrust can be used to generate three-body horseshoe orbits which rendezvous with the surface of one of the asteroids, returning to visit the same sites periodically. In order to achieve this, it is first necessary to analyse the effect of continuous thrust on the generation of horseshoe orbits, which can be achieved through selection of a set of steering laws which can be compared against each other. If cameras are assumed for attitude sensing, then steering laws for which the thrust is always directed along the unit radius vector from either of the two asteroids are, in principle, relatively simple to implement. The problem can be further simplified by keeping the thrust-induced acceleration constant, avoiding the need for throttling the propulsion system if the specific impulse is assumed to be high and the corresponding spacecraft mass change is small. With this as a foundation, a method can then be sought for finding

periodic thrust augmented horseshoe orbits which rendezvous with one of the asteroids in a binary pair.

Certain elements of the above scenarios could be achieved using solar sails for propulsion, however, as stated in Section 1.1, solar sails have limitations such as an inability to direct a component of thrust in the Sun-ward direction, and zero thrust in eclipse periods. Therefore, the work in this Thesis assumes the use of continuous thrust such as that provided by electrostatic thrusters, which although they normally depend on photovoltaic power from the Sun, are not subject to the limitation in thrust direction. Modern electrostatic thrusters can produce continuous thrust in the μN and mN range with a specific impulse on the order of 3000 s, using propellants such as Xenon and possessing operating lifetimes of several years [15, 32, 34, 50], with the caveat that they generally have high input power requirements (e.g. the QinetiQ T5 thruster, which produces 20 mN of thrust for 700 W of electrical power [33]).

1.3 Thesis Objectives

This Section describes the objectives of the Thesis, as derived from the literature review of Section 1.1 and the research motivation of Section 1.2. The objectives are defined as follows:

1. In the HCW approximation of motion relative to a target on a circular two-body orbit, to apply thrust proportional to the relative displacement of a spacecraft in order to modify the natural frequencies of motion and thereby produce a rich range of new types of relative orbits which are accessible for small, low-cost spacecraft with only limited on-board sensing.

2. In the CRTBP, to apply thrust proportional to the displacement of a spacecraft relative to a collinear libration point, modifying the natural frequencies of motion to generate new types of stable singly- and multiply-periodic or-

bits, including thrust augmented lissajous- and halo-type orbits about the libration point.

3. In the cylindrical-polar form of the HCW approximation, to use low thrust propulsion and simple thrust commands to replicate certain aspects of three-body horseshoe orbits in a two-body system, thereby accessing new nested and phased orbits for spacecraft constellations.

4. In the CRTBP, to analyse the effects of constant thrust, directed towards either or both of the primary bodies (using an example binary asteroid system), upon the positions and stability properties of the system equilibria and the domain of existence of horseshoe orbits.

5. In the CRTBP, to propose a method for finding periodic thrust augmented horseshoe orbits which graze the surface of the smaller asteroid in a binary pair, facilitating touch-and-go sampling of the asteroid surface.

1.4 Thesis Structure and Related Authored Papers

This Section details the structure of the Thesis herein, outlining the contents of each Chapter and the associated objective. Related papers which were authored or co-authored by the author of this Thesis are also detailed, and indications are made as to how these papers relate to the Chapters.

The Thesis is structured as follows. Chapter 2 introduces the key dynamical models which are the technical foundations of the research presented, including descriptions of the Hill-Clohessy-Wiltshire approximation and the circular restricted three-body problem.

1.4.1 Chapter 3

Chapter 3 addresses Objective 1 (as described in Section 1.3). New types of thrust augmented relative orbits are generated in the two-body HCW approximation using position-only feedback to directly modify the eigenvalues (and therefore natural frequencies) of the linearised dynamics, allowing for interesting singly- and multiply-periodic trajectories to be developed. Only proportional control is employed, with no reference trajectory, and this simplicity is intended to facilitate access to such new orbits for small, low-cost spacecraft with limited on-board sensing and computational power.

The Chapter relates to the papers:

- C. S. Arnot, C. R. McInnes, Low thrust augmented spacecraft formation-flying for on-orbit inspection, *66th International Astronautical Congress*, IAC-15-C1.8.1.x28589, 12-16 October 2015 [59]

- C. S. Arnot, C. R. McInnes, Low thrust augmented spacecraft formation-flying, *25th International Symposium on Space Flight Dynamics: ISSFD 2015*, Munich, Germany, 19-23 October 2015 [60]

and to the two-body HCW sections of:

- C. S. Arnot, C. R. McInnes, R. J. McKay, M. Macdonald, J. Biggs, Orbit period modulation for relative motion using continuous low thrust in the two-body and restricted three-body problems, *Celestial Mechanics and Dynamical Astronomy*, vol. 130, no. 2, February 2018 [61]

The co-author McInnes provided supervision and guidance throughout the development of the research and the authoring of all three papers, while the co-authors McKay, Macdonald, and Biggs provided the initial idea of modifying the natural frequency of one axis of motion in the HCW approximation with continuous thrust, and offered advice during the writing of the journal paper. The author of this Thesis performed all research and authored each paper.

1.4.2 Chapter 4

Chapter 4 addresses Objective 2, employing a similar approach to Chapter 3, applied instead to the linearised dynamics around a libration point in the CRTBP. The eigenvalues of the system are modified using thrust proportional to position in order to generate stable orbits around the otherwise unstable collinear libration points. Modified-period Lissajous orbits are produced, and the feedback gains required for synchronisation of the in-plane and out-of-plane natural frequencies are derived, allowing stable, singly-periodic halo-type orbits around a libration point to be attained. Such orbits could be used to provide, for example, a constantly-visible communications relay for lunar far-side missions, extending Farquhar's original concept [62].

The Chapter relates to the CRTBP sections of the paper:

- C. S. Arnot, C. R. McInnes, R. J. McKay, M. Macdonald, J. Biggs, Orbit period modulation for relative motion using continuous low thrust in the two-body and restricted three-body problems, *Celestial Mechanics and Dynamical Astronomy*, vol. 130, no. 2, February 2018 [61]

for which the co-author McInnes provided supervision and guidance, while the co-authors McKay, Macdonald, and Biggs provided the initial idea of modifying the natural frequency of one axis of motion with continuous thrust in the HCW approximation (and so were not involved in the CRTBP sections). The author of this Thesis performed all research and authored the paper.

1.4.3 Chapter 5

Chapter 5 addresses Objective 3. In this Chapter, certain aspects of co-orbital horseshoe orbits are replicated in the HCW approximation, rendered in cylindrical-polar form, in order to develop the simple low thrust commands required to implement synchronised or phased nested constellations of spacecraft around a circular reference orbit.

The Chapter relates to the conference paper:

- C. S. Arnot, C. R. McInnes, Artificial horseshoe orbits using low thrust propulsion, *67th International Astronautical Congress*, IAC-16-C1.1.2x34607, 26-30 September 2016 [77]

for which the co-author McInnes provided supervision and guidance, while the author of this Thesis performed all research and authored the paper.

1.4.4 Chapter 6

Chapter 6 addresses Objective 4, investigating the effect of constant low thrust directed along the unit radius vector from each primary mass in the CRTBP on the existence of horseshoe orbits, through the analysis of the modified locations and stability properties of the equilibrium points in a particular binary asteroid system (243 Ida). The key accelerations at which horseshoe orbits become possible or impossible are identified for three separate steering laws, along with the regions in which other types of co-orbital motion exist (tadpole and crescent-shaped orbits).

The Chapter relates to the research in the submitted manuscript:

- C. S. Arnot, C. R. McInnes, Thrust-augmented horseshoe orbits in the circular restricted three-body problem, submitted to *Celestial Mechanics and Dynamical Astronomy*, May 2018 [93]

for which the co-author McInnes provided supervision and guidance, and the author of this Thesis performed all research and authored the paper.

1.4.5 Chapter 7

Chapter 7 addresses Objective 5, applying the principles established in Chapter 6 to propose a method for finding periodic thrust augmented horseshoe orbits which

graze the surface of the smaller primary, yielding new opportunities for touch-and-go sampling of binary asteroid systems. First, a search-and-filter technique is employed, modified from that used to find Lyapunov orbits, to find periodic horseshoe orbits. Analysis is then performed to locate those orbits which have close approaches to the smaller primary. It is shown that the use of thrust simplifies this process by widening the region in which horseshoe orbits can occur, and two members of a family of surface-grazing thrust augmented horseshoe orbits are presented. It is shown that the acceleration and Δv required for these particular orbits are modest and achievable with existing propulsion technology, and that the speed of the spacecraft relative to the smaller primary at rendezvous is small.

The Chapter also relates to the research in the submitted manuscript:

- C. S. Arnot, C. R. McInnes, Thrust-augmented horseshoe orbits in the circular restricted three-body problem, submitted to *Celestial Mechanics and Dynamical Astronomy*, May 2018 [93]

for which the co-author McInnes provided supervision and guidance, and the author of this Thesis performed all research and authored the paper.

1.4.6 Chapter 8

Finally, in Chapter 8, conclusions are drawn regarding the entirety of the Thesis, and future avenues of research are recommended.

Chapter 2

Dynamical Models

This Chapter describes the fundamental concepts and dynamical models which form the foundations of the investigations undertaken throughout the Thesis. The Hill-Clohessy-Wiltshire (HCW) approximation of spacecraft motion relative to a target point on a circular reference orbit is described in Section 2.1, along with the conditions for bounded motion, the types of relative orbits which occur in such a system, and the applications thereof. The circular restricted three-body problem is described in Section 2.2, including the derivation of the Jacobi integral (the sole integral of motion in the CRTBP), and the locations and nature of the five equilibrium points.

2.1 The Hill-Clohessy-Wiltshire Equations

The two-body problem describes the motion of two particles which interact gravitationally only with each other. It is the only natural gravitational problem for which a general closed-form solution has been found. Assuming that one of the masses is infinitesimally small in comparison to the other, then the barycentre of the system will be at the centre of the large mass, and only the small mass will orbit. If a further infinitesimal mass is added to the system, both small masses will orbit the massive body without interacting gravitationally with each other,

and the relative motion between them is a result only of the differences between their orbits relative to the central massive body. Let the first infinitesimal mass be called the *target spacecraft*, and the second be the *chase spacecraft*. Since, in this Thesis, the focus is on the motion of a chase spacecraft relative to a target (a spacecraft or a point), it is useful to define a frame of reference centred on the target, and rotating with it around the central massive body. A schematic of such a reference frame is given in Fig. 2.1. Assuming that the target's orbit is circular, the linearised equations of motion of the chase spacecraft relative to the target are the well-known Hill-Clohessy-Wiltshire equations, given as [37]

$$\ddot{x} = 3n^2 x + 2n\dot{y} \tag{2.1a}$$

$$\ddot{y} = -2n\dot{x} \tag{2.1b}$$

$$\ddot{z} = -n^2 z \tag{2.1c}$$

where n is the angular velocity of the rotating frame, the x-axis points in the radial direction, the y-axis points in the direction of the target's motion (the *along-track* direction), and the z-axis follows the orbit angular momentum vector and is therefore out of the plane of the target's orbit. The angular velocity is given by

$$n = \sqrt{\frac{GM}{r_0^3}} \tag{2.2}$$

where G is the Newtonian gravitational constant, M is the mass of the massive central body, and r_0 is the radius of the target's orbit around the massive body. The target's orbit is herein termed the *reference orbit*.

It can be shown that the HCW equations permit the closed-form solution [37]

$$x(t) = (4 - 3\cos nt)x_0 + \frac{\sin nt}{n}\dot{x}_0 + \frac{2}{n}(1 - \cos nt)\dot{y}_0 \tag{2.3a}$$

$$y(t) = \frac{2\dot{x}_0}{n}\cos nt + \left(6x_0 + \frac{4\dot{y}_0}{n}\right)\sin nt - (6nx_0 + 3\dot{y}_0)t - \frac{2\dot{x}_0}{n} + y_0 \tag{2.3b}$$

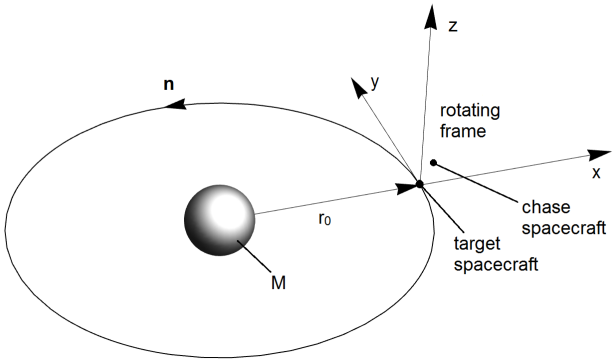

Figure 2.1: Rotating reference frame on a circular orbit.

$$z(t) = z_0 \cos nt + \frac{\dot{z}_0}{n} \sin nt \tag{2.3c}$$

This analysis is key to proximity operations between spacecraft and formation flight, since for any initial position (x_0, y_0, z_0) and velocity ($\dot{x}_0$, $\dot{y}_0$, $\dot{z}_0$), the state of the spacecraft after time t can be found. The new relative orbits which will be generated in Chapter 3 using the HCW approximation can be considered formation-flying orbits, since they assume the existence of a target spacecraft about which the chase spacecraft will move.

2.1.1 Condition for Bounded Motion

The HCW equations were initially derived as the basis of a terminal guidance system for satellite rendezvous, however they are also applied usefully to spacecraft formation flight. For such purposes, it is useful to find initial conditions for which the chase spacecraft's motion remains bound relative to the target. It can be seen by examining Eq. (2.3b) that the third term is secular and therefore becomes unbound with time. This can be avoided by selecting $\dot{y}_0 = -2nx_0$. With this condition, the motion of the chase spacecraft will describe an ellipse in the x-y plane with the major axis aligned with the y-axis. It is also evident from examining the remaining periodic terms that the amplitude of the y-axis motion will be exactly twice that of the x-axis motion. Figure 2.2 shows this bound

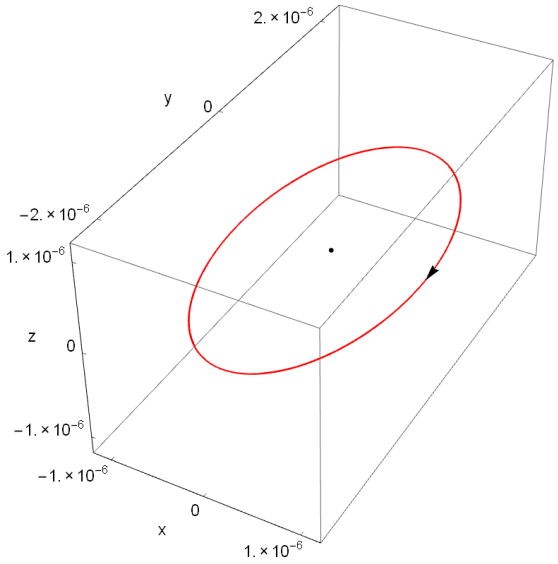

Figure 2.2: Bounded ballistic relative orbit in the HCW frame. The units have been normalised by the reference orbit radius. The black point represents the target spacecraft, and the arrow indicates the direction of motion of the chase spacecraft where $(x_0,\ y_0,\ z_0) = (10^{-6},\ 0,\ 0)$ and $(\dot{x}_0,\ \dot{y}_0,\ \dot{z}_0) = (0,\ -2nx_0,\ 0)$.

relative orbit, which was integrated numerically using Wolfram Mathematica's NDSolve function, and plotted using the ParametricPlot3D function.

Although circular motion in the x-y plane is not possible under free-flying conditions, a projected circular orbit (PCO) can be obtained in the y-z plane by selecting z_0 such that the y- and z-axis amplitudes are equal. In recent years, the feasibility of such orbits on a nanosatellite scale has been demonstrated by the University of Toronto Institude for Aerospace Studies (UTIAS) Canadian Advanced Nanospace Experiment (CanX) mission, with the CanX-4 and CanX-5 spacecraft. Using GPS carrier-phase differential techniques for relative navigation, the two spacecraft successfully entered into along-track formations at ranges of 1000 m and 500 m, and PCO formations at 100 m and 50 m range [109, 131].

2.2 The Circular Restricted Three-Body Problem

The circular restricted three-body problem (CRTBP) has been amongst the most studied problems in astrodynamics. It describes the motion of an infinitesimally small mass as it gravitationally interacts with two larger masses which themselves orbit the system barycentre in a circle. First formulated in order to model the motion of the Moon around the Earth in the presence of the gravitational influence of the Sun [111], the CRTBP has been found useful for describing the dynamics of many other celestial systems, from the motion of asteroids in the Sun-Jupiter system [65] to the dynamics of the narrow rings of certain planets in the solar system [112, 113].

A schematic of the CRTBP in the plane of motion of the two primaries is given in Fig. 2.3. The x-axis coincides with the line connecting the centres of the two primaries, and the barycentre of the system is found at the origin. Thus, the reference frame is rotating with the two primaries around the barycentre. Using the conventional formulation of the problem, the unit of length is the separation of the two primaries. The mass of the third body, m_3 is infinitesimal, and so the unit of mass is chosen such that $m_1 + m_2 = 1$. The mass of the smaller primary is chosen to be $m_2 = \mu$, such that the larger primary mass can then be given as $m_1 = 1 - \mu$, while m_1 is located at a distance μ from the barycentre and m_2 is located at a distance $1 - \mu$. The time unit of the system is chosen such that both the angular velocity of the rotating frame, ω_F, and the gravitational constant of the system, G, are unity, indicating that the period of the orbit of the two primaries is $T_F = 2\pi$.

The equations of motion of the CRTBP are given in Cartesian form as [111]

$$\ddot{x} - 2\dot{y} = x - \frac{\mu(x - 1 + \mu)}{r_2^3} - \frac{(1 - \mu)(\mu + x)}{r_1^3} = \frac{\partial \Omega}{\partial x} \tag{2.4a}$$

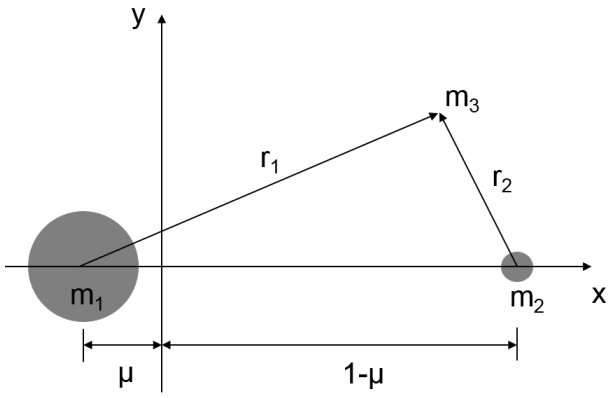

Figure 2.3: Schematic of the CRTBP.

$$\ddot{y} + 2\dot{x} = y - \frac{\mu y}{r_2^3} - \frac{(1-\mu)y}{r_1^3} = \frac{\partial \Omega}{\partial y} \tag{2.4b}$$

$$\ddot{z} = -\frac{(1-\mu)z}{r_1^3} - \frac{\mu z}{r_2^3} = \frac{\partial \Omega}{\partial z} \tag{2.4c}$$

where Ω is the sum of the gravitational and centrifugal potential (termed the *pseudo-potential*), and r_1 and r_2 are the distances of the spacecraft from m_1 and m_2, respectively. It can be shown that these distances are given by

$$r_1 = \sqrt{(x+\mu)^2 + y^2 + z^2} \tag{2.5a}$$

$$r_2 = \sqrt{(x-1+\mu)^2 + y^2 + z^2} \tag{2.5b}$$

and Ω is given by

$$\Omega = \frac{1}{2}(x^2 + y^2) + \left(\frac{1-\mu}{r_1} + \frac{\mu}{r_2}\right) \tag{2.6}$$

2.2.1 The Lagrange Points

In common with many dynamical systems, the CRTBP possesses points at which all forces acting upon the particle are balanced, called *equilibrium points*, *libration points*, or *Lagrange points*. The three equilibrium points which exist along the axis connecting the two primaries were first discovered by Euler (termed the *collinear points*), and two further points were later found by Lagrange at vertices

of equilateral triangles (termed the *triangular points*), symmetric about the x-axis, for which the primaries form the other two vertices [1].

The equilibrium points are found at all locations where $\frac{\partial\Omega}{\partial x} = \frac{\partial\Omega}{\partial y} = \frac{\partial\Omega}{\partial z} = 0$ and by selecting $\ddot{x} = \ddot{y} = \ddot{z} = \dot{x} = \dot{y} = \dot{z} = 0$ the equations of motion become

$$-x = -\frac{\mu(x-1+\mu)}{r_2^3} - \frac{(1-\mu)(\mu+x)}{r_1^3} \tag{2.7a}$$

$$-y = -\frac{\mu y}{r_2^3} - \frac{(1-\mu)y}{r_1^3} \tag{2.7b}$$

$$0 = -\frac{(1-\mu)z}{r_1^3} - \frac{\mu z}{r_2^3} \tag{2.7c}$$

whereupon it can immediately be seen that $z = 0$ and so any equilibrium points must be located in the orbit plane. The triangular points are found by selecting $r_1 = r_2 = 1$, such that Eq. (2.7a) and (2.7b) become identities showing that the points exist at the vertices of equilateral triangles (L_4 is found at $(\frac{1}{2} - \mu, \frac{\sqrt{3}}{2}, 0)$ and L_5 at $(\frac{1}{2} - \mu, -\frac{\sqrt{3}}{2}, 0)$).

The three collinear points are located by adding the further condition $y = 0$, such that the three equations are reduced to one, given as

$$x = \frac{\mu(x-1+\mu)}{|x+\mu|^3} + \frac{(1-\mu)(\mu+x)}{|x-1+\mu|^3} \tag{2.8}$$

Algebraic operations are then performed to yield a quintic expression in terms of x, which is solved numerically to locate the three collinear points, and has no more than three real roots for $0 \leq \mu \leq 1$.

The locations of the five equilibrium points are shown in Fig. 2.4 for a mass ratio equal to that of the Earth-Moon system. The locations were found using Mathematica's NSolve function, and the Figure created using the Plot function. The usual naming convention for the equilibrium points is: L_1, L_2, and L_3 are the collinear points in the intervals $(1-\mu) > x > -\mu$, $\infty > x > (1-\mu)$, and $-\mu > x > -\infty$, respectively, L_4 is the triangular point ahead of the smaller

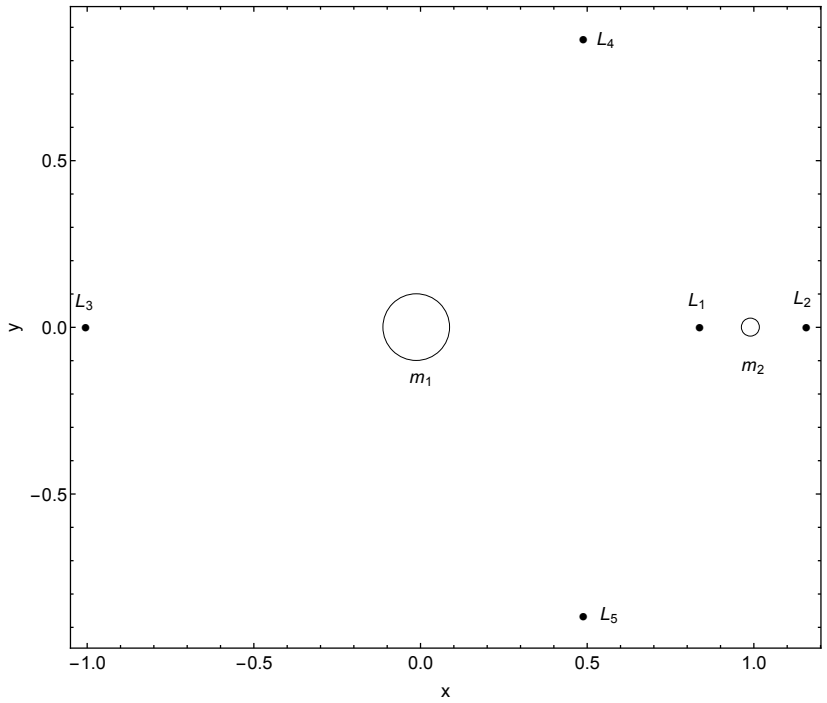

Figure 2.4: Locations of the primaries and equilibrium points of the CRTBP with $\mu = 0.01213$ (equivalent to the Earth-Moon system).

primary in the direction of rotation, and L_5 is the triangular point behind the smaller primary in the direction of rotation.

It can be shown through linearisation of the dynamics of the problem close to a Lagrange point that the collinear points are unstable, but numerous missions have placed spacecraft in the vicinity of the L_1 and L_2 points of the Sun-Earth system, such as the Solar and Heliospheric Observatory (SOHO) [114] and Advanced Composition Explorer (ACE) [115] at L_1, and ESA's Gaia spacecraft at L_2, requiring only modest station-keeping efforts. The triangular points are linearly stable for $\mu \leq 0.03852$ [110]. This stability is evidenced in the solar system by the large populations of Trojan asteroids which librate around the Sun-Jupiter L_4 and L_5 ($\mu = 9.536 \times 10^{-4}$). Furthermore, objects are not limited to solely orbiting one or other of the triangular points. Horseshoe-shaped orbits, which encompass L_3, L_4, and L_5, are also possible, as noted in Section 1.1.4.

2.2.2 The Jacobi Integral

In order to obtain a general solution to the CRTBP, six integrals of motion would be required. Only one exists, called the *Jacobi integral*, and it is the only scalar constant of motion within the CRTBP.

The equations of motion in Eq. (2.4) can be given in the form

$$\ddot{x} - 2\dot{y} = \frac{\partial \Omega}{\partial x} \tag{2.9a}$$

$$\ddot{y} + 2\dot{x} = \frac{\partial \Omega}{\partial y} \tag{2.9b}$$

$$\ddot{z} = \frac{\partial \Omega}{\partial z} \tag{2.9c}$$

Equations (2.9a), (2.9b), and (2.9c) can be multiplied by $\dot{x}$, $\dot{y}$, and $\dot{z}$, respectively, and the summation of all three gives

$$\dot{x}\ddot{x} + \dot{y}\ddot{y} + \dot{z}\ddot{z} = \frac{\partial \Omega}{\partial x}\dot{x} + \frac{\partial \Omega}{\partial y}\dot{y} + \frac{\partial \Omega}{\partial z}\dot{z} \tag{2.10}$$

This expression may then be integrated to yield

$$\dot{x}^2 + \dot{y}^2 + \dot{z}^2 = 2\Omega - C \tag{2.11}$$

where C is a constant of integration. Therefore, the Jacobi integral can be written as

$$C = 2\Omega - v^2 = (x^2 + y^2 + z^2) - (\dot{x} + \dot{y} + \dot{z}) + \frac{2 - 2\mu}{r_1} + \frac{2\mu}{r_2} \tag{2.12}$$

where v is the velocity of the particle with respect to the rotating frame [110].

This integral is useful for finding the accessible regions of motion within the CRTBP, as by choosing $v = 0$, it is possible to find the critical boundaries which a particle possessing a particular value of C cannot cross. These boundaries, termed the *zero-velocity curves* of the system, are shown in Fig. 2.5 for a system with a mass ratio equal to the Earth-Moon system. This Figure was generated

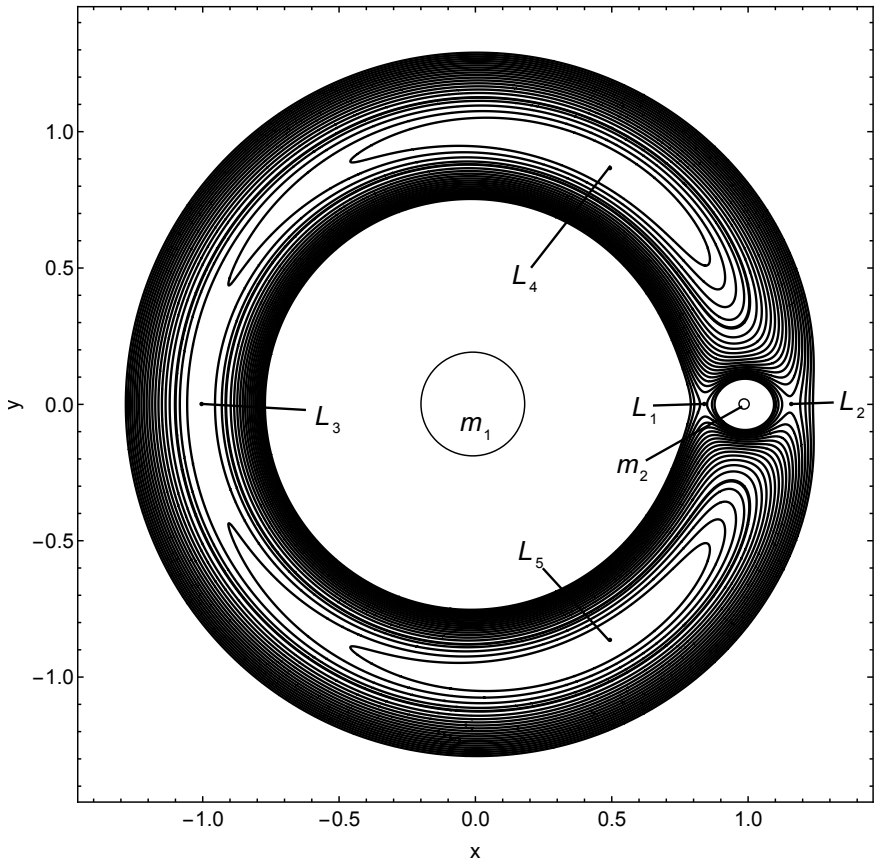

Figure 2.5: Zero-velocity curves of the CRTBP, for $\mu = 0.01213$ (equivalent to the Earth-Moon system) and $3 \leq C \leq 3.21$.

using Mathematica's ContourPlot function.

Chapter 3

Forced Relative Motion in the Hill-Clohessy-Wiltshire Approximation

This Chapter addresses Objective 1 as described in Section 1.3, by aiming to generate rich new families of relative orbits for spacecraft formation flight using the two-body HCW approximation. Section 3.1 describes the dynamics of the HCW approximation when augmented with thrust terms, Section 3.2 describes how artificial static equilibria and a circular relative orbit can be achieved, and Section 3.3 derives the closed-loop feedback gains required to modify the natural frequency of the out-of-plane motion and shows how this can be used to transfer between oppositely displaced non-Keplerian orbits. Section 3.4 derives the thrust commands necessary to generate a circular relative orbit of any radius, orientation, or period, and shows how this can be combined with the modified out-of-plane motion to generate a cylindrical relative orbit and a Sun-vector tracking orbit. Finally, Section 3.5 offers conclusions for the research presented in this Chapter.

It is proposed here that position feedback can be used to modify the natural frequencies of the linearised dynamics through direct manipulation of the system eigenvalues and to thereby produce interesting and novel stable relative orbits.

Whereas past authors have generally used a top-down engineering approach, designing active controllers with which to force a spacecraft onto a predetermined reference trajectory (e.g. [55,56,58]), this work instead seeks to generate rich new families of orbits with position-only feedback and without a reference trajectory, thereby deriving utility from simple control strategies. As discussed in Section 1.2, the assumption of the use of only position feedback instead of full state feedback is justified by the goal of providing access to useful new trajectories for small, low-cost spacecraft equipped with only position sensing relative to a target spacecraft (e.g. [87]). The use of position-only feedback mitigates the difficulties inherent in the implementation of accurate relative velocity sensing aboard such a spacecraft, and also avoids the need for taking the time derivative of the position vector (a method which is prone to noise errors). This strategy still permits attainment of relative orbits in two-body systems with potential future applications for space-based interferometry, hyperspectral sensing, and on-orbit inspection.

The Chapter builds on initial work [59] concerning forced motion relative to a circular two-body reference orbit, comprising the systematic derivation and exploration of new families of forced relative orbits using linearised dynamics derived from the two-body problem. Using a state-space method, position feedback control is then used to manipulate the eigenvalues (and therefore the natural frequencies) of the system to produce interesting new relative orbits. A particular aim of this Chapter is to generate relative orbits with potential future applications for on-orbit inspection and servicing - an area where the advantages of modifying the frequencies of periodic motion are numerous.

3.1 Equations of Motion

As stated in Section 2.1, the motion of a chase spacecraft relative to a target on a circular two-body reference orbit can be described by the linear Hill-Clohessy-Wiltshire equations. With the target at the origin of the rotating frame as shown

in Fig. 2.1, the x-axis follows the radius vector from the central mass through the target, the z-axis follows the orbital angular momentum vector, and the y-axis points in the along-track direction of the target's motion around the central body. This reference frame forms the environment in which new relative orbits are generated throughout this Chapter.

The well known HCW equations of Eq. (2.1), augmented with continuous thrust terms, are given by

$$\ddot{x} = 3n^2 x + 2n\dot{y} + u_x \tag{3.1a}$$

$$\ddot{y} = -2n\dot{x} + u_y \tag{3.1b}$$

$$\ddot{z} = -n^2 z + u_z \tag{3.1c}$$

where u_x, u_y, and u_z are the thrust-induced acceleration terms, and n is again the angular velocity of the rotating frame. Assuming that the mass of the spacecraft is small with respect to the Earth, the angular velocity is given by Eq. (2.2).

To apply thrust terms to the HCW equations, the dynamics from Eq. (3.1a-3.1c) are first converted to the state-space form

$$\dot{\boldsymbol{x}} = \boldsymbol{A}\boldsymbol{x} + \boldsymbol{B}\boldsymbol{u} \tag{3.2}$$

where $\boldsymbol{x} = [x \;\; y \;\; z \;\; \dot{x} \;\; \dot{y} \;\; \dot{z}]^T$, and

$$\boldsymbol{A} = \begin{bmatrix} 0 & 0 & 0 & 1 & 0 & 0 \\ 0 & 0 & 0 & 0 & 1 & 0 \\ 0 & 0 & 0 & 0 & 0 & 1 \\ 3n^2 & 0 & 0 & 0 & 2n & 0 \\ 0 & 0 & 0 & -2n & 0 & 0 \\ 0 & 0 & -n^2 & 0 & 0 & 0 \end{bmatrix} \tag{3.3}$$

$$\boldsymbol{B} = \begin{bmatrix} 0 & 0 & 0 \\ 0 & 0 & 0 \\ 0 & 0 & 0 \\ 1 & 0 & 0 \\ 0 & 1 & 0 \\ 0 & 0 & 1 \end{bmatrix} \tag{3.4}$$

A strategy is now proposed whereby the thrust-induced acceleration is proportional to the displacement in the radial, along-track, and out-of-plane axes only. The acceleration-law is therefore defined by

$$\boldsymbol{u} = -\boldsymbol{K}\boldsymbol{x} \tag{3.5}$$

where the feedback gain matrix $\boldsymbol{K}$ is given by

$$\boldsymbol{K} = \begin{bmatrix} K_{11} & 0 & 0 & 0 & 0 & 0 \\ 0 & K_{22} & 0 & 0 & 0 & 0 \\ 0 & 0 & K_{33} & 0 & 0 & 0 \end{bmatrix} \tag{3.6}$$

The upper bound of the input acceleration can be easily defined therefore in terms of the maximum displacement along each axis, as

$$\boldsymbol{u}_{max} = \begin{bmatrix} |u_{xmax}| \\ |u_{ymax}| \\ |u_{zmax}| \end{bmatrix} = \begin{bmatrix} K_{11}x_{max} \\ K_{22}y_{max} \\ K_{33}z_{max} \end{bmatrix} \tag{3.7}$$

The control acceleration can therefore be bounded through the appropriate selection of the maximum displacement along each axis, which is in turn generally determined from the initial conditions.

Now, set $\boldsymbol{A_c} = \boldsymbol{A} - \boldsymbol{B}\boldsymbol{K}$, which has eigenvalues $\boldsymbol{\lambda}$ and corresponding eigenvectors $\boldsymbol{V}$. The characteristic polynomial $p(\lambda)$ of the matrix $\boldsymbol{A_c}$ can be given as

$$p(\lambda) = \det(\boldsymbol{A_c} - \lambda \boldsymbol{I}) = \begin{vmatrix} -\lambda & 0 & 0 & 1 & 0 & 0 \\ 0 & -\lambda & 0 & 0 & 1 & 0 \\ 0 & 0 & -\lambda & 0 & 0 & 1 \\ 3n^2 - K_{11} & 0 & 0 & -\lambda & 2n & 0 \\ 0 & -K_{22} & 0 & -2n & -\lambda & 0 \\ 0 & 0 & -n^2 - K_{33} & 0 & 0 & -\lambda \end{vmatrix} \tag{3.8}$$

The eigenvalues are the roots of $p(\lambda)$, and are therefore found to be

$$\boldsymbol{\lambda} = \begin{bmatrix} -\frac{\sqrt{-K_{11}-K_{22}-n^2-\sqrt{(K_{11}-K_{22})^2+2(K_{11}+7K_{22})n^2+n^4}}}{\sqrt{2}} \\ \frac{\sqrt{-K_{11}-K_{22}-n^2-\sqrt{(K_{11}-K_{22})^2+2(K_{11}+7K_{22})n^2+n^4}}}{\sqrt{2}} \\ -\frac{\sqrt{-K_{11}-K_{22}-n^2+\sqrt{(K_{11}-K_{22})^2+2(K_{11}+7K_{22})n^2+n^4}}}{\sqrt{2}} \\ \frac{\sqrt{-K_{11}-K_{22}-n^2+\sqrt{(K_{11}-K_{22})^2+2(K_{11}+7K_{22})n^2+n^4}}}{\sqrt{2}} \\ -\sqrt{-K_{33}-n^2} \\ \sqrt{-K_{33}-n^2} \end{bmatrix} \tag{3.9}$$

Since the eigenvalues represent the natural frequencies of the system, modifying $\boldsymbol{K}$ therefore directly modifies these frequencies. Feedback gains K_{11} and K_{22} both affect the first two conjugate pairs of eigenvalues corresponding to the in-plane motion, and K_{33} only affects a single decoupled pair of eigenvalues, corresponding to the z-axis motion. This key idea of modifying the natural frequencies of the system through position-only feedback is used to produce interesting and novel relative trajectories in the two-body problem in this Chapter, and in the circular restricted three-body problem in Chapter 4.

Stable oscillatory behaviour occurs when the eigenvalues are imaginary, so it is useful to find the corresponding range of gains for this behaviour. Considering the second, fourth, and sixth elements of Eq. (3.9), (λ_2, λ_4, and λ_6), since these eigenvalues each form one half of a conjugate pair, plots indicating the regions in

which these eigenvalues are real, complex, and imaginary are given in Fig. 3.1. These Figures were generated using Mathematica's RegionPlot function. The eigenvalue λ_6 is considered separately since it is only affected by a single gain, K_{33}. Unstable regions are found where the real parts of the eigenvalues are greater than zero. For λ_2, it can be seen that the imaginary region covers approximately three quarters of the $K_{11} - K_{22}$ values, but that the imaginary region of λ_4 only covers a subset of these. Thus, for stable in-plane oscillatory motion, gains of approximately $K_{11} \geq 2.97n^2$ and $K_{22} \geq 0$ should generally be selected. It should also be noted that a small imaginary region close to $K_{11} = K_{22} = 0$ exists, which includes the free-flying case at one of its boundaries. It can be seen from Fig. 3.1c that the out-of-plane motion is stable and oscillatory for $K_{33} > -n^2$.

The state transition matrix, $\boldsymbol{\Phi}$, which can be used to find the general solution to Eq. (3.2), is given by

$$\boldsymbol{\Phi} = \boldsymbol{W}(t)\boldsymbol{W}^{-1}(0) \tag{3.10}$$

where $\boldsymbol{W}(t)$ is the fundamental solution matrix which satisfies

$$\dot{\boldsymbol{W}}(t) = \boldsymbol{A}(t)\boldsymbol{W}(t) \tag{3.11}$$

The fundamental solution to the system is given as [126]

$$\boldsymbol{W}(t) = \boldsymbol{V} \begin{bmatrix} e^{\lambda_1 t} & 0 & \cdots & 0 \\ 0 & e^{\lambda_2 t} & \cdots & 0 \\ \vdots & & \ddots & \vdots \\ 0 & \cdots & & e^{\lambda_6 t} \end{bmatrix} \tag{3.12}$$

Note that, in the case where the eigenvalues are complex, it is necessary to take the real and imaginary parts of the complex solution separately to find the real fundamental solution to the system, $\boldsymbol{W_r}(t)$. The general solution to Eq. (3.2), including control inputs, can then be found from

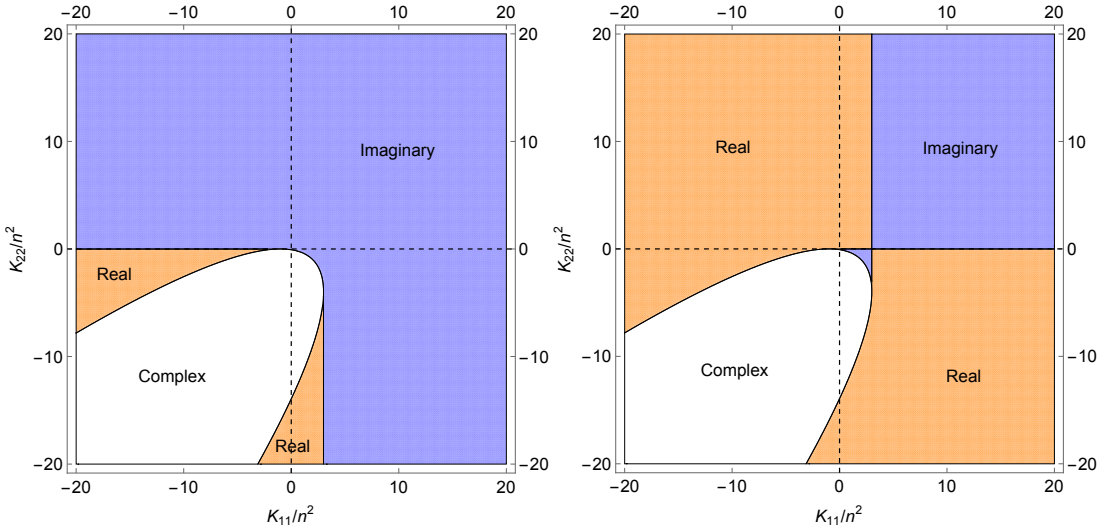

(a) Behaviour of λ_2.

(b) Behaviour of λ_4.

(c) Behaviour of λ_6.

Figure 3.1: Regions for which λ_2, λ_4, and λ_6 are purely imaginary, purely real, and complex.

$$\boldsymbol{x}(t) = \boldsymbol{W_r}(t)\boldsymbol{W_r}^{-1}(0)\boldsymbol{x}(0) + \boldsymbol{W_r}(t)\int_{t_0}^{t} \boldsymbol{W_r}^{-1}(\tau)\boldsymbol{B}\boldsymbol{u}\, d\tau \tag{3.13}$$

In the case that $K_{11} = K_{22} = K_{33} = 0$, the time domain solution to the system is equal to the well known closed-form solution to the HCW equations of Eq. (2.3), given in matrix form as

$$\begin{bmatrix} x(t) \\ y(t) \\ z(t) \\ \dot{x}(t) \\ \dot{y}(t) \\ \dot{z}(t) \end{bmatrix} = \begin{bmatrix} S_1 & S_2 \end{bmatrix} \begin{bmatrix} x_0 \\ y_0 \\ z_0 \\ \dot{x}_0 \\ \dot{y}_0 \\ \dot{z}_0 \end{bmatrix} \tag{3.14}$$

where

$$S_1 = \begin{bmatrix} 4 - 3\cos nt & 0 & 0 \\ 6(\sin nt - nt) & 1 & 0 \\ 0 & 0 & \cos nt \\ 3n\sin nt & 0 & 0 \\ -6(1 - \cos nt) & 0 & 0 \\ 0 & 0 & -n\sin nt \end{bmatrix}$$

$$S_2 = \begin{bmatrix} \frac{1}{n}\sin nt & \frac{2}{n}(1 - \cos nt) & 0 \\ -\frac{2}{n}(1 - \cos nt) & \frac{1}{n}(4\sin nt - 3nt) & 0 \\ 0 & 0 & \frac{1}{n}\sin nt \\ \cos nt & 2\sin nt & 0 \\ -2\sin nt & 4\cos nt - 3 & 0 \\ 0 & 0 & \cos nt \end{bmatrix}$$

Since the aim of this work is to modify the natural frequencies of the system and thereby generate novel orbits, it is necessary that at least one of the gains

is non-zero, and so the solution in Eq. (3.14) cannot be used in its entirety. However, part of this solution will be used in certain Δv calculations later in this Chapter.

3.2 Artificial Static Equilibria and a Simple Circular Relative Orbit

An interesting case to demonstrate the eigenvalue-based approach is that of the generation of artificial static equilibria in the rotating frame of reference using continuous thrust, since, if zero initial velocity is *not* assumed (for a truly static solution), it is useful to characterise the type and frequency of motion followed by the spacecraft. Such equilibria in the rotating frame are equivalent to type III non-Keplerian orbits when viewed from an inertial frame [18].

Consider the state vector $\boldsymbol{x} = [x, y, z, \dot{x}, \dot{y}, \dot{z}]^T$ in which $\dot{x}$, $\dot{y}$, and $\dot{z}$ must be zero for a static displacement. Since $\boldsymbol{u} = -\boldsymbol{K}\boldsymbol{x}$, the system state equation is $\dot{\boldsymbol{x}} = \boldsymbol{A}\boldsymbol{x} + \boldsymbol{B}(-\boldsymbol{K}\boldsymbol{x})$. With zero initial velocity ($\dot{x}_0 = \dot{y}_0 = \dot{z}_0 = 0$) the system state is held constant by selecting the feedback gains as

$$\boldsymbol{K} = \begin{bmatrix} 3n^2 & 0 & 0 & 0 & 0 & 0 \\ 0 & 0 & 0 & 0 & 0 & 0 \\ 0 & 0 & -n^2 & 0 & 0 & 0 \end{bmatrix} \tag{3.15}$$

With reference to Fig. 3.1, the motion should be stable, with all non-zero eigenvalues being imaginary. Indeed, the eigenvalues of the system are found to be

$$\boldsymbol{\lambda} = \begin{bmatrix} -2in \\ 2in \\ 0 \\ 0 \\ 0 \\ 0 \end{bmatrix} \tag{3.16}$$

If the initial velocity is zero, there are no oscillations and the spacecraft remains fixed at its initial position. However, with non-zero initial velocity, since the coefficient of both λ_1 and λ_2 is 2, the forced natural frequency of the motion in the x-y plane is twice the unforced natural frequency. Since $K_{22} = 0$, for static formations in the rotating frame, the along-track position is arbitrary as it does not affect the required thrust.

For zero thrust, bounded in-plane motion is always elliptical, and apparent circular motion is only possible in the y-z plane (the projected circular orbit, as described in Section 2.1). Interestingly, with the feedback gains in Eq. (3.15) ($u_x = -3n^2x$, $u_y = 0$, $u_z = n^2z$) the in-plane motion of the spacecraft can be made circular simply by selecting the appropriate initial velocity along the x- and y-axes. Recalling the condition for bounded motion in the HCW equations as given in Section 2.1 ($\dot{y}_0 = -2nx_0$) it is necessary only to add the condition $\dot{x}_0 = 2ny_0$, and the result is a circular trajectory in the x-y plane. As already indicated, the relative orbit period is half of the reference orbit period. Furthermore, in this case the gain K_{33} is arbitrary because the z-axis motion is decoupled and the circular trajectory exists only in the x-y plane, and so the circular relative orbit is achieved using thrust in only the radial direction. An example of this type of relative motion is shown in Fig. 3.2, where the target is on a geostationary Earth orbit (GEO) ($r_0 = 42157 \times 10^3$ m, $x_0 = 100$ m, $y_0 = z_0 = 0$, $\dot{x}_0 = \dot{z}_0 = 0$, $\dot{y}_0 = -2nx_0$). The orbit was integrated using Mathematica's NDSolve, Fig. 3.2a was created using ParametricPlot3D, and Fig. 3.2b was created using Plot.

All subsequent graphs of relative orbits and thrust-induced acceleration in this Chapter were generated in this way, and assume a target on a geostationary orbit.

In the case of zero initial velocity, i.e. for a static formation, the Δv required to maintain the formation is simple to calculate. Since with zero initial velocity $u_x = -3n^2x$ is constant, and assuming independent body-mounted thrusters on each axis, it is possible to find

$$\Delta v_x = 3n^2 x\tau \tag{3.17}$$

where τ is the duration for which the formation is maintained. Similarly, since $u_z = n^2 z$ is also constant, we can find

$$\Delta v_z = n^2 z\tau \tag{3.18}$$

Using the example of a target point in geostationary orbit, with Eq. (3.17) and (3.18), the Δv accumulated for a chase spacecraft positioned for one sidereal day in a 100 m z-axis statically displaced non-Keplerian orbit is 0.046 ms^{-1}, and for a 100 m x-axis displacement is 0.138 ms^{-1}. Assuming the use of electrostatic ion thrusters with a specific impulse of 3000 s, for a nanosatellite with initial mass of 10 kg, this amounts to a propellant expenditure of only 1.56×10^{-5} kg and 4.69×10^{-5} kg, respectively. For a full year of operation, with independent axis-aligned thrusters, the total propellant expenditure would be approximately 23 g. Considering that even a 3U CubeSat could feasibly carry in excess of 1.5 kg of Xenon propellant [116], this expenditure is very small.

3.3 Modulation of the Out-of-Plane Period

Having considered the in-plane behaviour of the system under the feedback gains of Eq. (3.15), the out-of-plane motion is now considered. When $K_{33} = -n^2$ with some non-zero z_0, the chase spacecraft is fixed in a displaced non-Keplerian

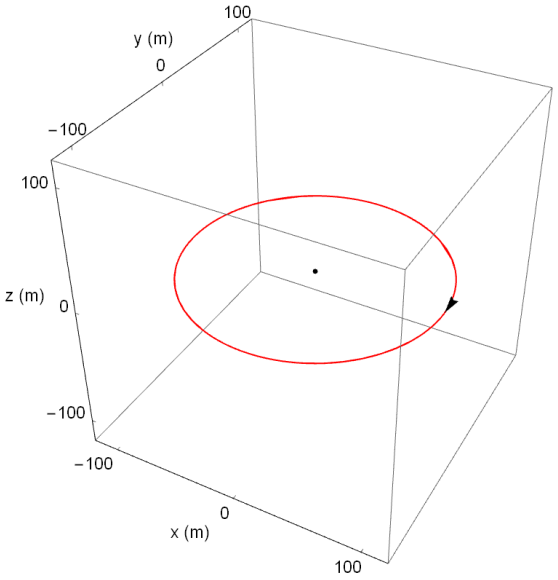

(a) Chase spacecraft trajectory.

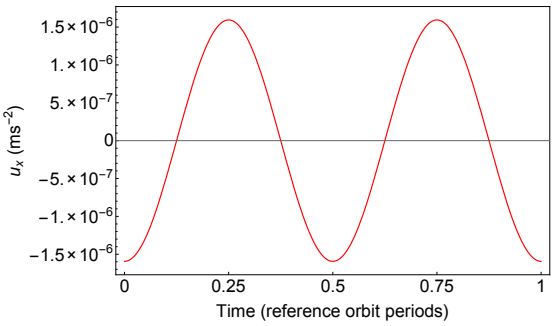

(b) Thrust-induced acceleration.

Figure 3.2: In-plane circular relative orbit achieved with single axis thrust around a geostationary target. In (a), the trajectory of the chase spacecraft is shown in red, the target is the black point, and the arrow indicates the direction of chase spacecraft motion. In (b) the required thrust-induced acceleration along the x-axis is shown. Initial conditions are $r_0 = 42157 \times 10^3$ m, $x_0 = 100$ m, $y_0 = z_0 = 0$, $\dot{x}_0 = \dot{z}_0 = 0$, $\dot{y}_0 = -2nx_0$.

orbit whose plane does not contain the two-body centre of mass. Oppositely, when $K_{33} = 0$, we have the ballistic case, and the spacecraft oscillates along the z-axis with a period equal to the reference orbit period. A z-displaced static formation can therefore be considered a periodic relative orbit with infinite out-of-plane period. As noted by Arnot and McInnes [59], it is possible to modify the period of the periodic z-axis motion by making the z-axis thrust proportional to displacement. The period of motion along the z-axis is now modified by changing the out-of-plane thrust component.

To begin, it is necessary to substitute $K_{33} = -n^2$ with $K_{33} = -\psi^2$, so that the eigenvalue corresponding to the out-of-plane motion, λ_6 in Eq. (3.9), becomes

$$\lambda_6 = \sqrt{\psi^2 - n^2} \tag{3.19}$$

It follows that $u_z = \psi^2 z$, and

$$\boldsymbol{A_c} = \begin{bmatrix} 0 & 0 & 0 & 1 & 0 & 0 \\ 0 & 0 & 0 & 0 & 1 & 0 \\ 0 & 0 & 0 & 0 & 0 & 1 \\ -K_{11} + 3n^2 & 0 & 0 & 0 & 2n & 0 \\ 0 & -K_{22} & 0 & -2n & 0 & 0 \\ 0 & 0 & \psi^2 - n^2 & 0 & 0 & 0 \end{bmatrix} \tag{3.20}$$

An augmented angular frequency, Ω, is now defined by

$$\Omega^2 = (n^2 - \psi^2) \tag{3.21}$$

and so

$$\Omega = \frac{n}{k} \tag{3.22}$$

in which k represents the number of reference orbit periods in which the thrust augmented relative motion completes a single out-of-plane cycle. Therefore, k can

be considered the augmented period coefficient, so that the period of the z-axis motion is $T_z = kT$. Through use of out-of-plane thrust, the period of the z-axis motion can now be freely chosen.

Substituting Eq. (3.22) into (3.21), it is possible to rearrange for ψ such that

$$\psi = n\sqrt{1 - \left(\frac{1}{k^2}\right)} \tag{3.23}$$

It can then be shown from Eq. (3.1c) that the new equation of out-of-plane motion is given by

$$\ddot{z} = -\frac{n^2 z}{k^2} \tag{3.24}$$

which is a harmonic oscillator whose natural frequency can now be selected through the coefficient of the out-of-plane thrust law. The maximum input acceleration for this type of relative orbit is given simply by $|u_{zmax}| = \psi^2 z_0$, assuming that the initial velocity is zero.

An example of thrust augmented z-axis motion is shown in Fig. 3.3a and 3.3c, where $k = 3$ and $k = 1/3$, respectively, $x_0 = z_0 = 100$ m, $r_0 = 42157 \times 10^3$ m and $\dot{y}_0 = -2nx_0$. These plots

Clearly, when $k = 1$, the thrust-induced acceleration in the z-direction is zero, corresponding to ballistic motion. However, when $k < 1$, the thrust is non-zero and in the opposite direction to the case $k > 1$. In addition, the frequency of oscillation in the z-direction is greater than the unforced frequency. When $k \to \infty$, the expression for the thrust acceleration simplifies to $u_z = n^2 z$, so that $K_{33} = -n^2$, and the z-axis displacement becomes fixed: that is, the trajectory is equivalent to static equilibria in the rotating frame.

To calculate the Δv required to maintain this type of continuously forced orbit, the third row of Eq. (3.14) must be considered, which describes the unforced out-of-plane position of the chase spacecraft. Since $\dot{z}_0 = 0$ and the frequency of the out-of-plane motion is now defined by Ω, the out-of-plane displacement simplifies

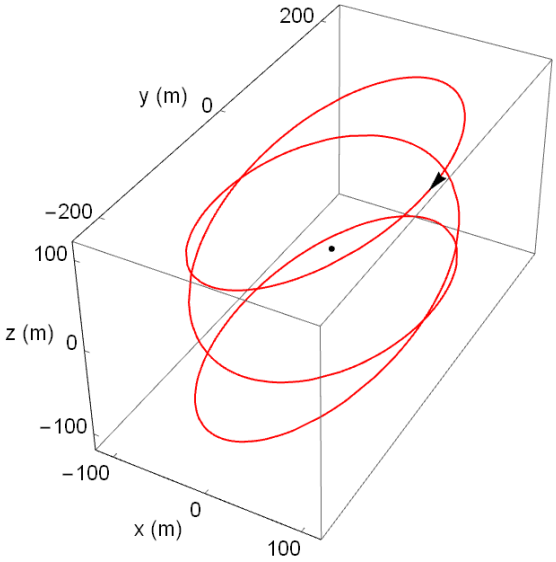

(a) $T_z = 3T$.

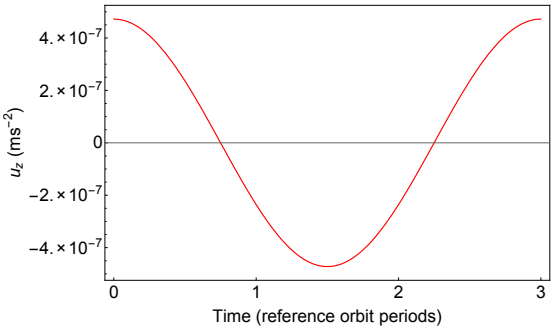

(b) Thrust-induced acceleration for $T_z = 3T$.

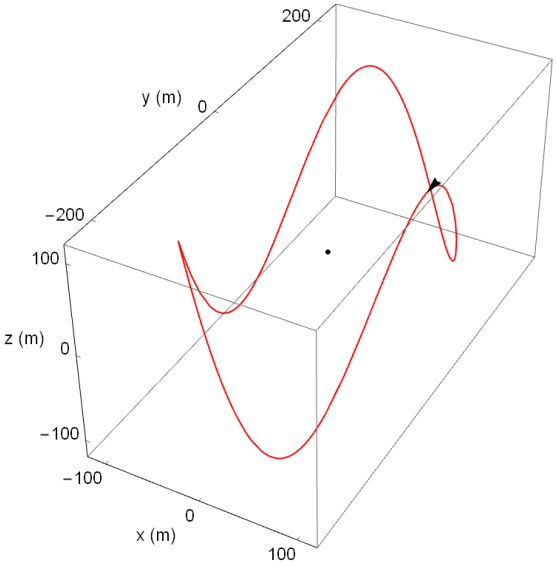

(c) $T_z = T/3$.

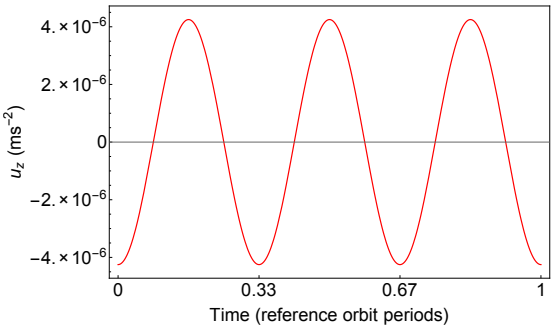

(d) Thrust-induced acceleration for $T_z = T/3$.

Figure 3.3: Relative orbits with modified out-of-plane natural frequency. Figure (a) shows the trajectory of the chase spacecraft for $k = 3$, (b) shows the required out-of-plane acceleration for $k = 3$, (c) shows the trajectory of the spacecraft for $k = 1/3$, and (d) shows the required out-of-plane acceleration for $k = 1/3$. Initial conditions are $r_0 = 42157 \times 10^3$ m, $x_0 = z_0 = 100$ m, $y_0 = 0$, $\dot{x}_0 = \dot{z}_0 = 0$, and $\dot{y}_0 = -2nx_0$

to

$$z(t) = z_0 \cos \Omega t \tag{3.25}$$

It follows that the thrust command, u_z, becomes

$$u_z = \psi^2 z_0 \cos \Omega t \tag{3.26}$$

To find the Δv accumulated over multiple orbit periods, the magnitude of the acceleration must be considered since the direction of the out-of-plane thrust changes direction at every plane crossing. This requires description as a piecewise function, such that

$$|u_z| = \begin{cases} \psi^2 z_0 \cos \Omega t \text{ if } \cos \Omega t \geq 0 \\ -\psi^2 z_0 \cos \Omega t \text{ if } \cos \Omega t < 0 \end{cases} \tag{3.27}$$

The integral then takes the form [59]

$$\Delta v_z = \psi^2 z_0 \left[\eta \int_{t=0}^{t=T_z} |\cos \Omega t| dt + \int_{t=\eta T_z}^{t=\varepsilon+\eta T_z} |\cos \Omega t| dt \right] \tag{3.28}$$

where η is the integer number of complete z-axis motion periods which have elapsed and ε is the additional time over the integer number of periods. Thus, the expression for accumulated Δv becomes

$$\Delta v_z = \psi^2 z_0 \left[\frac{4\eta}{\Omega} + \int_{t=\eta T_z}^{t=\varepsilon+T_z} |\cos \Omega t| dt \right] \tag{3.29}$$

Equation (3.29) can be integrated for all positive integer values of η, and for $0 \leq \varepsilon < T_z$.

3.3.1 Patching Between Non-Keplerian Orbits

Transfers between displaced non-Keplerian orbits can be achieved simply in the rotating frame using low or zero thrust. It can be envisaged that the ability to patch, or transfer, between oppositely displaced orbits for small or zero Δv

could be operationally advantageous for applications such as on-orbit inspection by offering a change in vantage point from which to view the target. For an initially displaced orbit using $K_{33} = -n^2$, the feedback may simply be disabled for half of a reference orbit period, at which point the feedback is reapplied. The result is then that the chase spacecraft is placed on an oppositely-displaced non-Keplerian orbit. Furthermore, it is possible to modulate the out-of-plane period for this transfer using the method proposed in Section 3.3 ($u_z = \psi^2 z$), allowing modification of the transfer time. Depending on ψ, transfers between displaced orbits could complete in longer or shorter periods than the natural out-of-plane period.

In an on-orbit inspection scenario, further utility may be drawn from the thrust augmented transfer trajectory since it can be adjusted to avoid interference with, or obstruction of, the target's sensor payload or communications antennae. The zero-thrust patching trajectory, where the feedback is disabled for the duration of the transfer, is the most feasible to perform with existing technology, since an accurately throttled propulsion system is not required: while the thrust output of an electrostatic thruster can be throttled through the control of the voltage between the two charged grids, this also impacts the specific impulse of the thruster [33]. All patching manoeuvres proposed here assume accurate measurement of the relative displacement of the chase spacecraft, since any error will result in oscillations around the intended equilibrium point. However, any oscillations will be stable, assuming correct selection of the feedback gains (based on accurate knowledge of the target spacecraft's mean motion, n) such that λ_6 does not become real.

Figure 3.4 shows four example transfers around a geostationary target ($r_0 = 42157 \times 10^3$ m, $x_0 = z_0 = 100$ m, $y_0 = 0$, $\dot{x}_0 = \dot{z}_0 = 0$, $\dot{y} = -2nx_0$), three of which use low thrust to modify the out-of-plane natural frequency (Fig. 3.4a, 3.4e, 3.4g), and one of which is a simple zero-thrust transfer (Fig. 3.4c). The required thrust-induced acceleration in the out-of-plane direction is also given for

each case.

3.4 The Cylindrical Relative Orbit

Now that a means of modulating the frequency of the out-of-plane motion has been found, an interesting and novel application can be envisaged: on orbit inspection of a target by a chase spacecraft using continuous thrust to modify its relative orbit period. The concept of on-orbit inspection has been explored by other authors, however the use of continuous low thrust has generally not been considered in this context. Using continuous thrust, a chase spacecraft on an inspection mission can actively force its relative motion to enable operationally advantageous non-Keplerian inspection trajectories. Perhaps the most interesting example is that of a small spacecraft tasked to inspect multiple satellites on the geostationary ring, and so previous work has considered the use of a thrust augmented relative orbit in which the chase spacecraft tracks the sun vector around a target in geostationary orbit [59]. Such a trajectory enables use of constant-angle illumination to facilitate visual inspection. Here the more general case of a cylindrical relative orbit is considered, which makes use of thrust augmented in-plane and out-of-plane motion to produce an orbit with two distinct modified periods.

A cylindrical relative orbit can be achieved by using the circular in-plane orbit already described (using $K_{11} = 3n^2$ and $K_{22} = 0$) combined with out-of-plane orbit period modulation ($K_{33} = -\psi^2$). Selecting an appropriate out-of-plane period, the result is that the chase spacecraft performs a helical sweep around the target as it oscillates between z_0 and $-z_0$ with an in-plane period of $0.5T$. However, although it is possible to freely select the out-of-plane period, this type of trajectory has a fixed in-plane period. A circular relative orbit whose period and orientation can also be freely selected would be of greater operational advantage. As stated in Section 1.1, Bando and Ichikawa [58] showed that circular

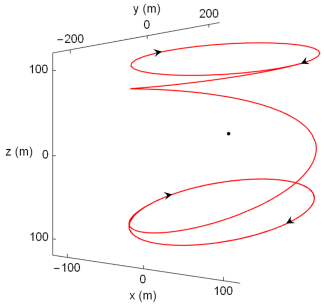

(a) $k = 3$

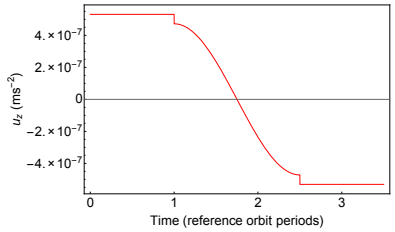

(b) $k = 3$

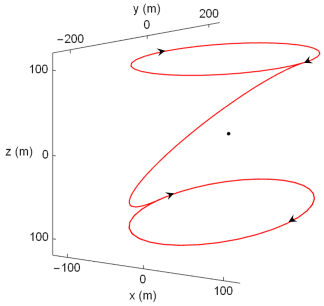

(c) $k = 1$

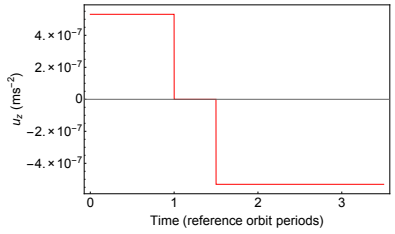

(d) $k = 1$

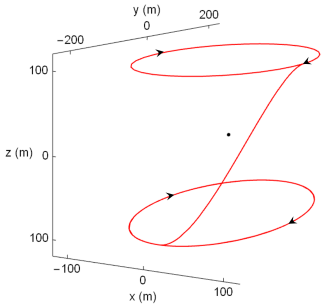

(e) $k = 0.5$

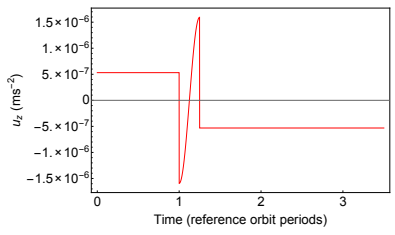

(f) $k = 0.5$

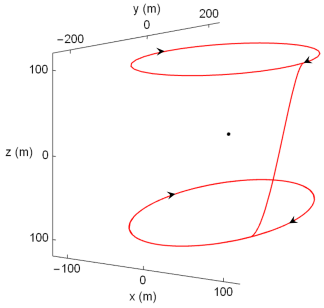

(g) $k = 0.2$

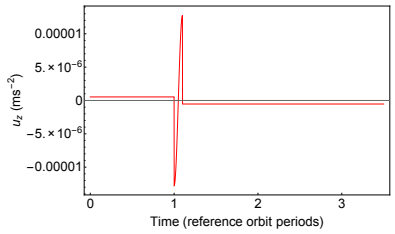

(h) $k = 0.2$

Figure 3.4: Patching between displaced non-Keplerian orbits using low thrust. Figures (a-d) show the trajectory (red) of the chase spacecraft. Figures (e-h) show the required thrust-induced acceleration. Initial conditions are $r_0 = 42157 \times 10^3$ m, $x_0 = z_0 = 100$ m, $y_0 = 0$, $\dot{x}_0 = \dot{z}_0 = 0$, $\dot{y} = -2nx_0$.

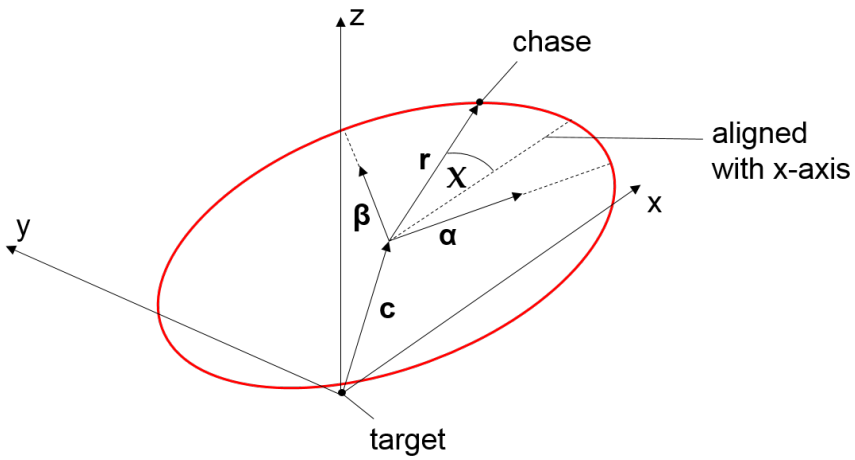

Figure 3.5: Parametrically described circular relative orbit in the HCW reference frame.

and elliptical relative orbits of arbitrary frequency were achievable using active control, however a useful analytical description of such a family of orbits has apparently not been presented in the literature and is derived parametrically as follows.

To produce a circular trajectory about the target spacecraft, consider first a three-dimensional circle as shown in Fig. 3.5. It is described parametrically by the unit vector $\boldsymbol{\alpha} = [\alpha_1, \alpha_2, \alpha_3]^T$, which is coincident with the circle's transformed x-axis (transformed from the x-axis of the rotating frame and fixed with respect to the circle), and the unit vector $\boldsymbol{\beta} = [\beta_1, \beta_2, \beta_3]^T$, which is coincident with the transformed y-axis of the circle. The vector describing the position of the circle's centre in the rotating frame is $\boldsymbol{c} = [c_1, c_2, c_3]^T$, $\boldsymbol{r}$ is the radius vector of the circle, and χ is the angle between the radius vector and the x-axis as measured in the anticlockwise direction about the circle's central axis. It is taken that $\chi = -\gamma nt$ (negative because the motion of the chase spacecraft in the x-y-plane is clockwise), where γ is the ratio of the target spacecraft's Keplerian orbit period to that of the circular relative orbit in the rotating frame (for example, if $\gamma = 1$, the period of the circular motion is equal to that of the Keplerian orbit of the target spacecraft), and where n and t have their usual meaning. The inclusion of

γ permits the modification of the period of the relative orbit, so that

$$\boldsymbol{r} = \boldsymbol{c} + r\cos(\chi)\boldsymbol{\alpha} + r\sin(\chi)\boldsymbol{\beta} \tag{3.30}$$

The first and second derivatives of Eq. (3.30) are found to be

$$\dot{\boldsymbol{r}} = r\gamma n\sin(\chi)\boldsymbol{\alpha} - r\gamma n\cos(\chi)\boldsymbol{\beta} \tag{3.31}$$

$$\ddot{\boldsymbol{r}} = -r(\gamma n)^2\cos(\chi)\boldsymbol{\alpha} - r(\gamma n)^2\sin(\chi)\boldsymbol{\beta} \tag{3.32}$$

It follows that, in this case, $\dot{\boldsymbol{x}} = [\dot{\boldsymbol{r}}, \ddot{\boldsymbol{r}}]^T$. Then, referring to Eq. (3.2), the acceleration input $\boldsymbol{u} = [u_x, u_y, u_z]^T$ is recalled. Thus, it can be shown that

$$\dot{\boldsymbol{x}} = \begin{bmatrix} \dot{x} \\ \dot{y} \\ \dot{z} \\ 3n^2x + 2n\dot{y} + u_x \\ -2n\dot{x} + u_y \\ -n^2z + u_z \end{bmatrix} = \begin{bmatrix} r\gamma n\sin(\chi)\alpha_1 - r\gamma n\cos(\chi)\beta_1 \\ r\gamma n\sin(\chi)\alpha_2 - r\gamma n\cos(\chi)\beta_2 \\ r\gamma n\sin(\chi)\alpha_3 - r\gamma n\cos(\chi)\beta_4 \\ -r(\gamma n)^2\cos(\chi)\alpha_1 - r(\gamma n)^2\sin(\chi)\beta_1 \\ -r(\gamma n)^2\cos(\chi)\alpha_2 - r(\gamma n)^2\sin(\chi)\beta_2 \\ -r(\gamma n)^2\cos(\chi)\alpha_3 - r(\gamma n)^2\sin(\chi)\beta_3 \end{bmatrix} \tag{3.33}$$

The input acceleration $\boldsymbol{u}$ can then be obtained as

$$\boldsymbol{u} = \begin{bmatrix} n^2(-r(\alpha_1(\gamma^2+3) - 2\beta_2\gamma)\cos\gamma nt + r(2\alpha_2\gamma + \beta_1(\gamma^2+3))\sin\gamma nt - 3c_1 \\ -n^2r\gamma((2\alpha_1 - \beta_2\gamma)\sin\gamma nt + (\alpha_2\gamma + 2\beta_1)\cos\gamma nt) \\ n^2(-\alpha_3r(\gamma^2-1)\cos\gamma nt + \beta_3r(\gamma^2-1)\sin\gamma nt + c_3 \end{bmatrix} \tag{3.34}$$

Using u_x from Eq. (3.34), it can be shown that the single axis thrust case described earlier is a special case of the general thrust equations. Since this case (using $u_x = -3n^2x$) is a circle in the x-y plane and centred at the origin, $\boldsymbol{\alpha} = [1,0,0]^T$, $\boldsymbol{\beta} = [0,1,0]^T$, and $\boldsymbol{c} = [0,0,0]^T$, so that $\boldsymbol{u}$ simplifies to

$$\boldsymbol{u} = \begin{bmatrix} -n^2 r(\gamma^2 - 2\gamma + 3)\cos\gamma nt \\ -n^2 r\gamma(2-\gamma)\sin\gamma nt \\ 0 \end{bmatrix} \tag{3.35}$$

where $r\cos\gamma nt \equiv x$. Therefore, in order for the first row of Eq. (3.35) to be equivalent to $u_x = -3n^2x$, it is clear that $\gamma = 2$. Interestingly, we note that with $\gamma = 2$, it follows that $u_y = 0$ and as required, $u_x = -3n^2 r\cos 2nt \equiv -3n^2x$, which is equivalent to the earlier state feedback case where $K_{11} = 3n^2$. This provides a particularly simple steering law with a useful application. The value of γ also correctly indicates that the period of the in-plane motion is $0.5T$. From Eq. (3.35), it is deduced that the maximum input acceleration in each axis is given by $|u_{xmax}| = -n^2 r(\gamma^2 - 2\gamma + 3)$ and $|u_{ymax}| = -n^2 r\gamma(2-\gamma)$ for the x-axis and y-axis, respectively.

The general case thrust commands of Eq. (3.34) can be used to produce a circular relative orbit with arbitrary dimension, orientation and frequency. However, for the cylindrical relative orbit, the circle is only required in the x-y plane, and so the vectors $\boldsymbol{\alpha}$ and $\boldsymbol{\beta}$ are coincident with the HCW x- and y-axes in this case. The two unit vectors $\boldsymbol{\alpha}$ and $\boldsymbol{\beta}$ are $[1,0,0]^T$ and $[0,1,0]^T$ respectively. The circle's centre is $c = [0,0,z]$. Now, using the in-plane thrust components defined in Eq. (3.35) and the out-of-plane gain $K_{33} = -\psi^2$, the natural frequencies of the circular in-plane motion and oscillatory out-of-plane motion can be freely modified. As before, the z-axis position varies sinusoidally between the maximum and minimum displacement. An example cylindrical relative orbit achieved using this approach is shown in Fig. 3.6 ($x_0 = z_0 = 100$ m, $y_0 = \dot{x}_0 = \dot{z} = 0$, $\dot{y}_0 = -nx_0$), with non-dimensional axes.

The Δv required to maintain the cylindrical orbit is found by integrating the three thrust acceleration components and summing the result, assuming independent body-mounted thrusters. Taking the x and y components from Eq. (3.35),

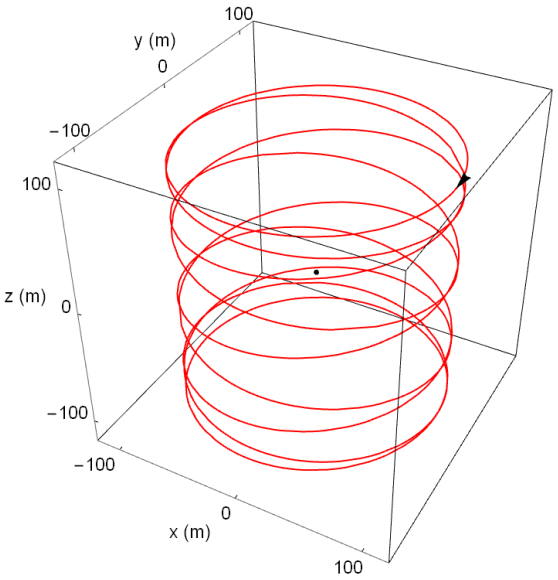

(a) Cylindrical relative orbit.

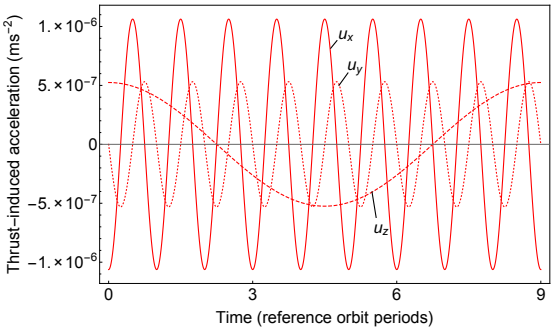

(b) Required acceleration.

Figure 3.6: Cylindrical relative orbit with $\gamma = 1$ and $k = 9$. Figure (a) shows the trajectory of the chase spacecraft, and (b) shows the required thrust-induced acceleration. Initial conditions are $r_0 = 42157 \times 10^3$ m, $x_0 = z_0 = 100$ m, $y_0 = \dot{x}_0 = \dot{z} = 0$, $\dot{y}_0 = -nx_0$.

the moduli are

$$|u_x| = \begin{cases} |-n^2 r(\gamma^2 - 2\gamma + 3)| \cos \gamma nt \text{ if } \cos \gamma nt \geq 0 \\ -n^2 r(\gamma^2 - 2\gamma + 3) \cos \gamma nt \text{ if } \cos \gamma nt < 0 \end{cases} \tag{3.36a}$$

$$|u_y| = \begin{cases} |-n^2 r\gamma(2 - \gamma)| \sin \gamma nt \text{ if } \sin \gamma nt \geq 0 \\ -n^2 r\gamma(2 - \gamma) \sin \gamma nt \text{ if } \sin \gamma nt < 0 \end{cases} \tag{3.36b}$$

The integrals then become

$$\Delta v_x = |-n^2 r(\gamma^2 - 2\gamma + 3)| \left[q \int_{t=0}^{t=T_{xy}} |\cos \gamma nt| dt + \int_{t=qT_{xy}}^{t=\upsilon+qT_{xy}} |\cos \gamma nt| dt \right] \tag{3.37a}$$

$$\Delta v_y = |-n^2 r\gamma(2 - \gamma)| \left[q \int_{t=0}^{t=T_{xy}} |\sin \gamma nt| dt + \int_{t=qT_{xy}}^{t=\upsilon+qT_{xy}} |\sin \gamma nt| dt \right] \tag{3.37b}$$

where Δv_x and Δv_y are the components of $\Delta \boldsymbol{v}$ in the x- and y-directions respectively, T_{xy} is the period of the x-y planar motion, q is the integer number of x-y planar motion periods which have elapsed, and υ is the additional time over the integer number of x-y motion periods. Integrating, the expressions for $\Delta \boldsymbol{v}$ become

$$\Delta v_x = |-n^2 r(\gamma^2 - 2\gamma + 3)| \left[\frac{4q}{\gamma n} + \int_{t=qT_{xy}}^{t=\upsilon+qT_{xy}} |\cos \gamma n t| dt \right] \tag{3.38a}$$

$$\Delta v_y = |-n^2 r\gamma(2-\gamma)| \left[\frac{4q}{\gamma n} + \int_{t=qT_{xy}}^{t=\upsilon+qT_{xy}} |\sin \gamma n t| dt \right] \tag{3.38b}$$

The z-axis component of $\Delta \boldsymbol{v}$ is as given in Eq. (3.29). Equations (3.38a) and (3.38b) can be integrated for all positive integer values of q, and for $0 \leq \upsilon < T_{xy}$.

3.4.1 The Sun Vector Tracking Orbit

A specific application of the cylindrical relative orbit is a relative orbit in which the chase spacecraft continuously tracks the Sun vector around a target spacecraft in geostationary Earth orbit. Such an orbit would allow for a continuous inspection of a target with constant-angle solar illumination, remote power collection, solar shielding, for astronomy, or hyperspectral sensing of the Sun with separate collector and detectors.

In the rotating frame centred on a target in geostationary orbit, the Sun vector will appear to track around the target in the x-y plane with a period of one solar day. Since the period of the geostationary orbit is one sidereal day, there will be a small angular lag of approximately one degree per day which will sum to one full rotation over one year. Furthermore, it should be noted that the geostationary orbit plane is inclined with respect to the ecliptic plane, so that the apparent declination of the solar radiation will vary with a period of one year. Assuming that the Earth's orbit is circular, it can be shown that the solar declination will vary sinusoidally. From the perspective of the target, the Sun vector will oscillate

along the z-axis. This implies that a chase spacecraft which tracks the Sun vector about the target will also be required to oscillate along the z-axis with a period of one year. Schematics illustrating this concept are shown in Fig. 3.7.

The required acceleration components to produce a Sun vector tracking orbit can be found by applying the strategy from Section 3.4. Since the circular in-plane orbit of the chase spacecraft is centred at the origin, it is possible to use the in-plane acceleration as defined by Eq. (3.35), where the difference in length of solar and sidereal days is accounted for by selecting $\gamma = 0.99727$. The out-of-plane feedback gain is $K_{33} = -\psi^2$, where $\psi = n\sqrt{1-(1/k^2)}$ and $k = 365.25$ to extend the out-of-plane period to that of the Julian year. The orbit produced by these acceleration commands is given in Fig. 3.8a.

The Δv required to maintain a Sun vector tracking orbit can be calculated from Eq. (3.38a), Eq. (3.38b), and Eq. (3.29), which yield the Δv in the x, y, and z directions, respectively. For an orbit with a 100 m in-plane radius, 43.3 m maximum out-of-plane displacement (as seen in Fig. 3.7e, using $z_0 = x_0 \tan(23.4^o)$), and independent axis-aligned thrusters, the total Δv for a full year of operation would be 36.7 m s^{-1}. This would amount to 12.5 g of propellant for a 10 kg nanosatellite equipped with electrostatic thrusters with specific impulse of 3000 s.

3.5 Conclusions

Continuous low thrust can augment the capabilities of spacecraft formations by permitting relative motion on forced Keplerian and non-Keplerian orbits. Simple control strategies based only on position feedback can be applied to generate rich new families of relative orbits using the Hill-Clohessy-Wiltshire approximation. Only position feedback is required, permitting the implementation of such strategies on-board small, low-cost spacecraft. The other main contributions offered by this Chapter are the parametric derivation of the thrust commands required

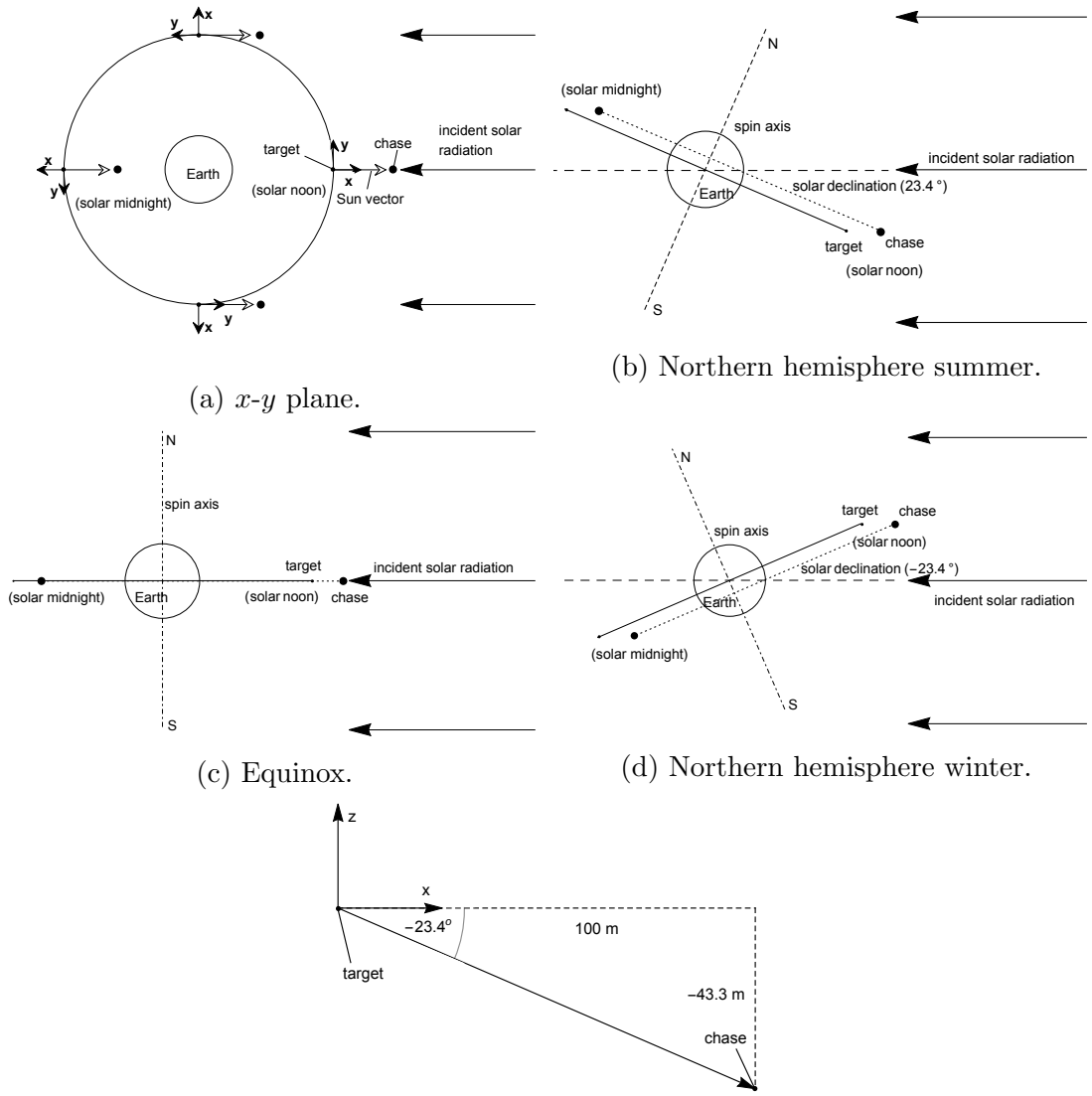

(a) x-y plane.

(b) Northern hemisphere summer.

(c) Equinox.

(d) Northern hemisphere winter.

(e) Example spacecraft position at Northern hemisphere midwinter.

Figure 3.7: Schematics of the position of chase spacecraft relative to target in a Sun vector tracking orbit.

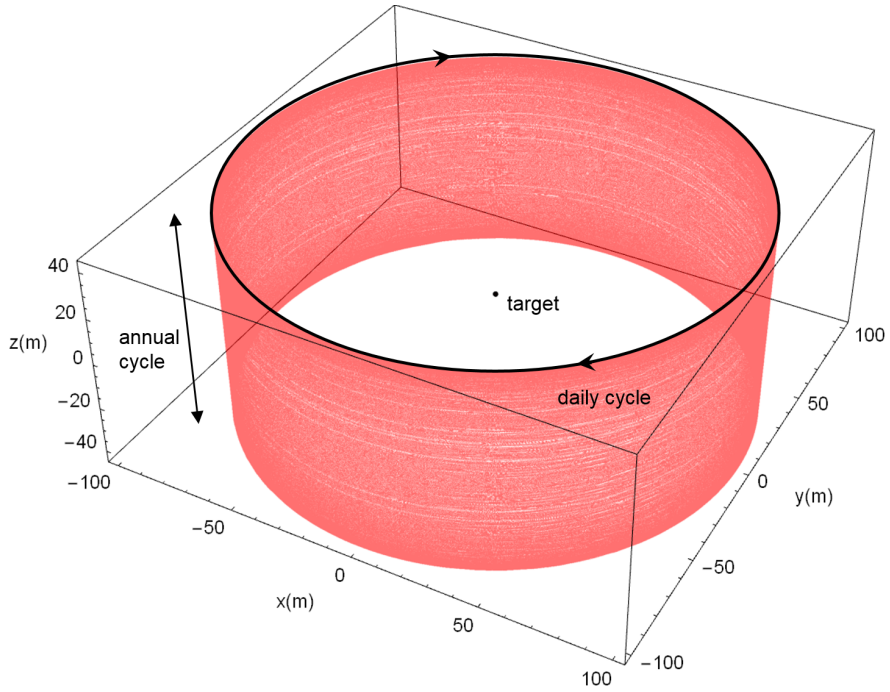

(a) Orbit simulated for one year.

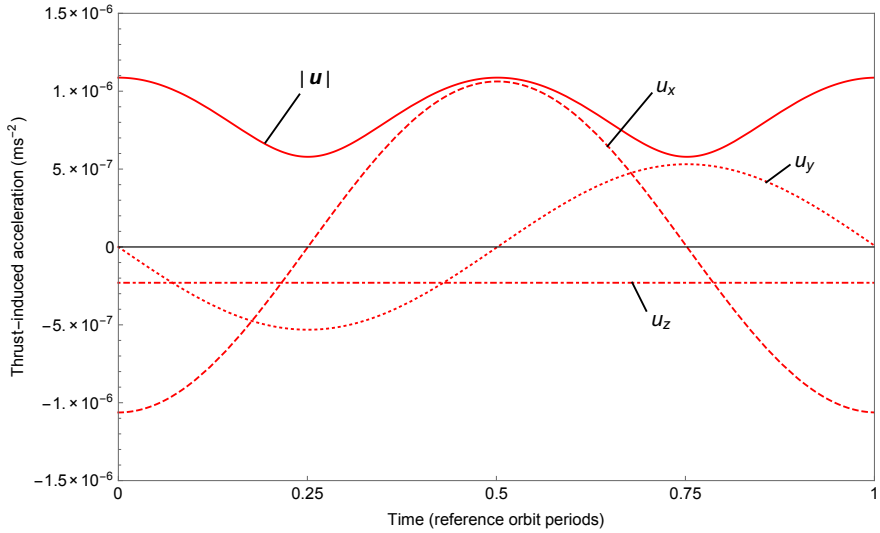

(b) Thrust-induced acceleration for one day.

Figure 3.8: Sun vector tracking orbit around a geostationary target. In (a) the red trajectory is the orbit, simulated for one year. In (b), the required thrust-induced acceleration over one day of operation is shown. Initial conditions are $r_0 = 42157 \times 10^3$ m, $x_0 = 100$ m, $y_0 = 0$, $z_0 = x_0 \tan(23.4^o)$, $\dot{x}_0 = 0$, $\dot{y}_0 = -\gamma x_0 n$, and $\dot{z}_0 = 0$.

for a forced circular orbit of arbitrary radius, orientation, and period relative to a target on a circular reference orbit, and the use of thrust to modify the natural frequency of out-of-plane motion. Cylindrical relative orbits, including an orbit in which a chase spacecraft continuously tracks the Sun vector about a target, have been developed, with potential future applications in on-orbit inspection, space situational awareness, and solar observation. The propellant requirements for these new orbits are small if modern electrostatic thruster technology is used. Technological challenges exist in the accurate measurement of inter-spacecraft distance, and in the throttling of electric propulsion systems without reductions in specific impulse. In the out-of-plane direction, small errors in position measurement or thrust-induced acceleration should generally result in small oscillations around the desired path or equilibrium point, which will remain stable with correct selection of the feedback gain.

The strategy proposed in this Chapter for modifying the natural frequencies of motion will be applied to the linearised dynamics in the vicinity of a libration point in the CRTBP in Chapter 4, and the specific method for modifying the out-of-plane natural frequency will be applied to artificial horseshoe orbits in Chapter 5.

Chapter 4

Forced Relative Motion in the Vicinity of Libration Points

This Chapter addresses Objective 2 as described in Section 1.3, by aiming to generate new and useful types of stable, thrust augmented singly- and multiply-periodic trajectories around libration points in the CRTBP, applying a similar approach to that of Chapter 3, using position-only feedback to modify the eigenvalues of the linearised dynamical system. Section 4.1 describes the linearised dynamics in the vicinity of a libration point, and Section 4.2 derives the state-space form of the system under position-only feedback and shows how the local dynamics at the Earth-Moon L_2 point can be made stable through modification of the system eigenvalues, generating new multiply-periodic relative orbits around the libration point. Section 4.3 describes how the in-plane and out-of-plane natural frequencies of motion can be synchronised with thrust, such that singly-periodic halo-type orbits around the libration point can be achieved, and finally Section 4.4 offers conclusions for the Chapter.

Whereas Chapter 3 generated orbits with potential applications such as on-orbit inspection, this Chapter aims to identify the range of feedback gains for which stable oscillatory motion exists around an otherwise unstable collinear Lagrange point. The multiply-periodic relative orbits which result from this

closed-loop stability present interesting new opportunities for missions at Lagrange points, offering new multi-spacecraft formations for applications such as astronomy, solar observation, and telecommunications. The stable, multiply-periodic trajectories could be exploited for periodically reforming formations of spacecraft, allowing, for example, the simultaneous measurement of aspects of the Earth's magnetotail around the Sun-Earth L_2 point [117]. Or, at the Earth-Moon L_2 point, a formation of spacecraft could be used as a fractionated telescope positioned with the Sun always at the same relative angle, using stable multiply-periodic orbits to achieve a scanning capability.

A further objective of this Chapter is to derive the feedback gains required to synchronise the in-plane and out-of-plane frequencies to produce a three-dimensional, singly-periodic orbit with potential utility as an Earth-Moon L_2 communications relay with constant visibility from the Earth. Such an orbit provides a useful alternative to naturally-occurring halo orbits, since it offers arbitrary dimensions and relative orbit period. A special case of this kind of orbit, controlled using solar radiation pressure, was investigated by Tanaka and Kawaguchi [95], and can further be considered an extension of Farquhar's original concept for a halo-orbiting lunar far-side communications relay [62].

4.1 Equations of Motion

The frame of reference used in this Chapter is the same as that which was defined in Section 2.2, the geometry of which was provided in Fig. 2.4. Following the convention defined in Section 2.2, the spacecraft's position vector is normalised using the radius of the mutual circular orbit followed by the two primaries, and the time is normalised by the orbit period. The orbit period is taken to be 2π and the normalised time is t. The origin of the system is at the barycentre of the two primary masses, the x-axis is aligned with the vector connecting the two primary masses (m_1 and m_2) and the y-axis is perpendicular to it such that the

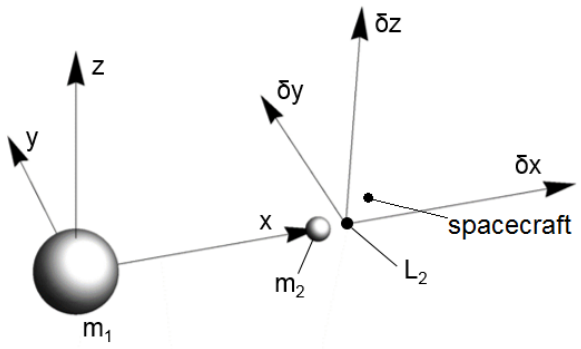

Figure 4.1: Schematic of the frame of reference centred on L_2.

x-y plane is the plane of the mutual orbit of the two primary masses and the z-axis completes the triad. However, since the aim is to examine the motion of a spacecraft relative to a Lagrange point with low thrust propulsion, it is useful to place the origin of the system at the Lagrange point in question, L_i ($i = 1$ to 5). Using this new origin, the δx-axis is aligned with the x-axis, the δy-axis is aligned with the y-axis, and the δz-axis again completes the right-hand coordinate system. A schematic of this reference frame is given in Fig. 4.1, using L_2 as an example.

The linearised equations of motion relative to the Lagrange point are given by [62]

$$\delta\ddot{x} = 2\delta\dot{y} + (2\sigma_i + 1)x \tag{4.1a}$$

$$\delta\ddot{y} = (1 - \sigma_i)y - 2\delta\dot{x} \tag{4.1b}$$

$$\delta\ddot{z} = -\sigma_i\delta z \tag{4.1c}$$

where

$$\sigma_i = \frac{\mu}{|l_i(\mu) - 1 + \mu|^3} + \frac{(1-\mu)}{|l_i(\mu) + \mu|^3} \tag{4.2}$$

in which $l_i(\mu)$ is the distance of the Lagrange point from the system barycentre. The mass ratio μ is given by

$$\mu = \frac{m_2}{m_1 + m_2} \tag{4.3}$$

The distance of the collinear Lagrange point from the system barycentre is found using the method in Section 2.2 (specifically, Eq. (2.8)), by solving

$$l_i(\mu) = \frac{1-\mu}{r_1^3}(l_i(\mu) + \mu) + \frac{\mu}{r_2^3}(l_i(\mu) - 1 + \mu) \tag{4.4}$$

4.2 State-Space System

Now that the linearised equations of motion have been defined, it is possible to generate the state-space form of the system. This allows the same analysis performed in Chapter 3 to be applied to the motion of a spacecraft around a Lagrange point. In particular, the state-space form will be used to find the eigenvalues of the closed-loop system, and the ranges of feedback gains which produce stable oscillatory motion at the Lagrange point can be identified.

The general state-space form of Eq. (4.1) has the same construction as Eq. (3.2), where $\boldsymbol{x} = [\delta x\ \delta y\ \delta z\ \delta\dot{x}\ \delta\dot{y}\ \delta\dot{z}]^T$, $\boldsymbol{u}$ has the same form as Eq. (3.5), and $\boldsymbol{K}$ is identical to Eq. (3.6). The system matrix $\boldsymbol{A}$ has the new form

$$\boldsymbol{A} = \begin{bmatrix} 0 & 0 & 0 & 1 & 0 & 0 \\ 0 & 0 & 0 & 0 & 1 & 0 \\ 0 & 0 & 0 & 0 & 0 & 1 \\ 2\sigma_i + 1 & 0 & 0 & 0 & 2 & 0 \\ 0 & 1-\sigma_i & 0 & -2 & 0 & 0 \\ 0 & 0 & -\sigma_i & 0 & 0 & 0 \end{bmatrix} \tag{4.5}$$

and $\boldsymbol{B}$ is identical to Eq. (3.4). Using the relation $\boldsymbol{A_c} = \boldsymbol{A} - \boldsymbol{BK}$ which has eigenvalues $\boldsymbol{\lambda}$ and eigenvectors $\boldsymbol{V}$, the general eigenvalues of the closed-loop system are found to be

$$\boldsymbol{\lambda} = \begin{bmatrix} -\frac{\sqrt{-2-K_{11}-K_{22}+\sigma_i-\sqrt{K_{11}^2+8(K_{22}-\sigma_i)-2K_{11}(-4+K_{22}+3\sigma_i)+(K_{22}+3\sigma_i)^2}}}{\sqrt{2}} \\ \frac{\sqrt{-2-K_{11}-K_{22}+\sigma_i-\sqrt{K_{11}^2+8(K_{22}-\sigma_i)-2K_{11}(-4+K_{22}+3\sigma_i)+(K_{22}+3\sigma_i)^2}}}{\sqrt{2}} \\ -\frac{\sqrt{-2-K_{11}-K_{22}+\sigma_i+\sqrt{K_{11}^2+8(K_{22}-\sigma_i)-2K_{11}(-4+K_{22}+3\sigma_i)+(K_{22}+3\sigma_i)^2}}}{\sqrt{2}} \\ \frac{\sqrt{-2-K_{11}-K_{22}+\sigma_i+\sqrt{K_{11}^2+8(K_{22}-\sigma_i)-2K_{11}(-4+K_{22}+3\sigma_i)+(K_{22}+3\sigma_i)^2}}}{\sqrt{2}} \\ -\sqrt{-K_{33}-\sigma_i} \\ \sqrt{-K_{33}-\sigma_i} \end{bmatrix} \tag{4.6}$$

Thus, in similar fashion to the linearised two-body problem, it is possible to modify the natural frequencies of the in-plane and out-of-plane motion independently by using $\boldsymbol{K}$. For the Earth-Moon L_2 point ($\mu = 0.01213$, $\sigma_2 = 3.19097$) the regions where the eigenvalues are purely imaginary, real, or complex are shown in Fig. 4.2. Mathematica's RegionPlot function was used to generate these Figures. The regions are similar to those of the two-body system, however unlike the two-body case the region boundaries are dependent on σ_i and so the stable region boundary changes at different Lagrange points and with different μ.

With reference to Fig. 4.2, it is worth noting that, unlike within the two-body HCW system, the in-plane motion around the Earth-Moon L_2 point is naturally unstable. With K_{11} and K_{22} both zero, λ_4 is positive and real. Therefore, in order to design useful, stable, oscillatory relative trajectories around a Lagrange point, it is necessary to apply feedback gains such that the eigenvalues become purely imaginary. For the Earth-Moon L_2 point, the relative in-plane motion will be stable and oscillatory when gains of approximately $K_{11} > 2.28\sigma_2$ and $K_{22} > -0.65\sigma_2$ are selected.

For arbitrary initial conditions, with K_{11} and K_{22} in the stable region, interesting doubly-periodic trajectories are produced. An example of this is shown in Fig. 4.3, where $K_{11} = K_{22} = 10\sigma_2$ and the initial velocity is zero. Since the z-axis motion is decoupled, it is not shown here. These Figures were generated using Mathematica's NDSolve and ParametricPlot functions.

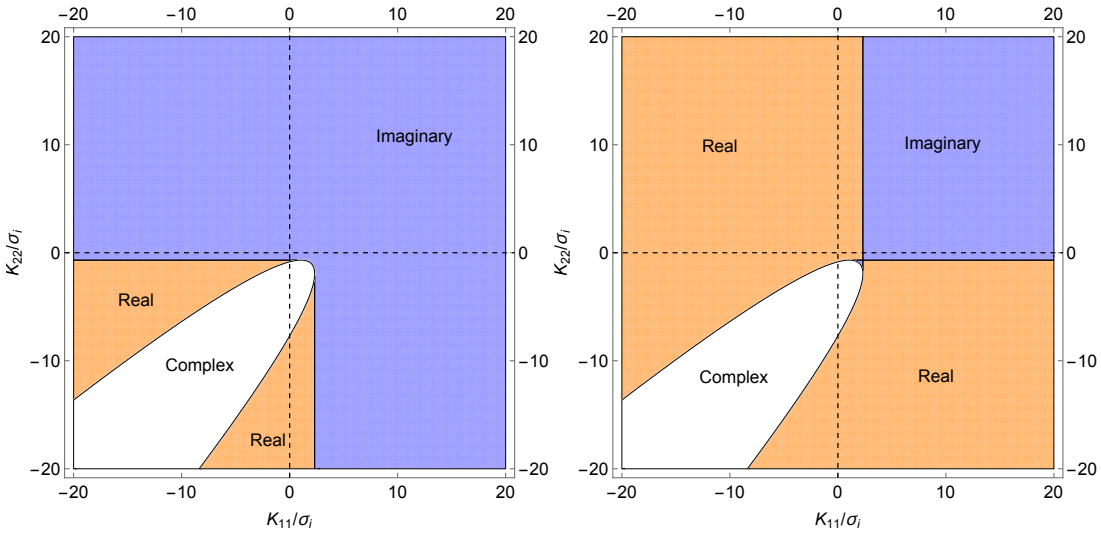

(a) Behaviour of λ_2. (b) Behaviour of λ_4.

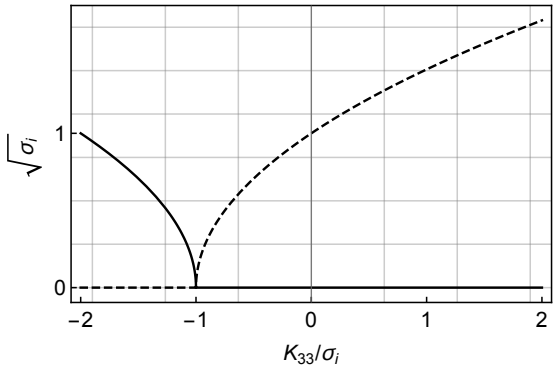

(c) Behaviour of λ_6.

Figure 4.2: Regions for which λ_2, λ_4, and λ_6 are purely imaginary, purely real, and complex, for Earth-Moon L_2 point ($\sigma_2 = 3.19097$).

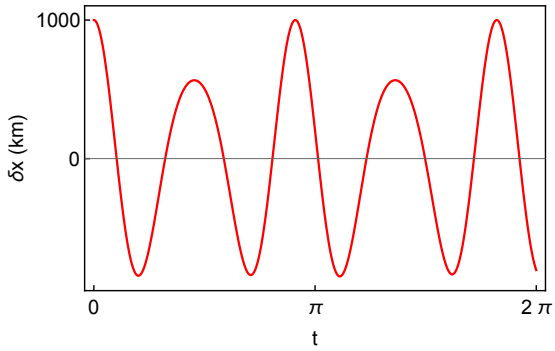

(a) δx-axis position over time.

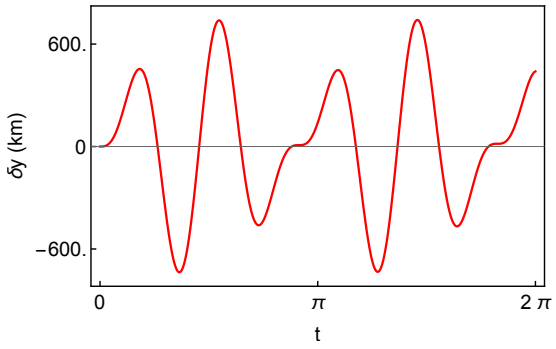

(b) δy-axis position over time.

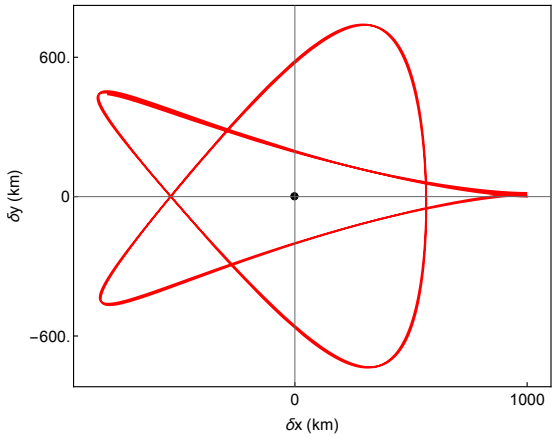

(c) $\delta x - \delta y$ plane.

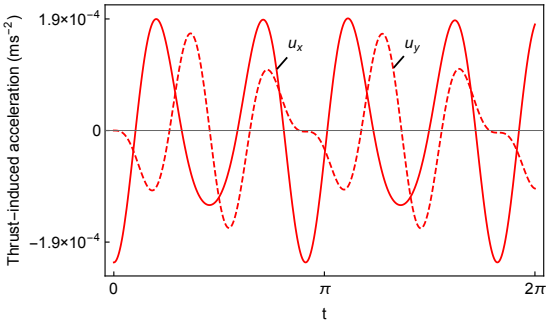

(d) Required thrust-induced acceleration.

Figure 4.3: In-plane trajectory for the doubly-periodic case, using $K_{11} = K_{22} = 10\sigma_2$, for Earth-Moon L_2 ($\sigma_2 = 3.19097$). Initial conditions are $\delta x_0 = 1000$ km, $\delta y_0 = \delta \dot{x}_0 = \delta \dot{y}_0 = 0$. The black point indicates the location of L_2.

4.3 Synchronisation of the In-Plane and Out-of-Plane Natural Frequencies

In the zero-thrust CRTBP, 3-dimensional periodic orbits about the collinear Lagrange points exist, called halo orbits. These orbits are described in Section 1.1, and a schematic of a halo orbit around the L_2 point of the CRTBP is shown in Fig. 1.4. Halo orbits are useful for certain mission architectures, however in this Section a different approach is used to generate three-dimensional periodic orbits. This approach requires feedback gains to be selected such that the in-plane and out-of-plane natural frequencies are equal, and permits the generation of pseudo-halo orbits of arbitrary dimensions and natural frequency. Although there are usually two distinct in-plane modes of oscillation, initial conditions may be selected such that the in-plane motion becomes singly-periodic, and therefore dependent on a single eigenvalue. The procedure for finding the required initial conditions is as follows.

Let $\boldsymbol{p}_j + i\boldsymbol{q}_j$ be the eigenvector corresponding to eigenvalue λ_j, and consider only the two in-plane eigenvalues λ_2 and λ_4 (since the out-of-plane motion is decoupled) such that $j = (2, 4)$. Recalling that the eigenvalue λ_j is equivalent to the natural frequency ω_j, it can be shown that the three dimensional periodic solution is found from [96]

$$\begin{bmatrix} \delta x \\ \delta y \\ \delta \dot{x} \\ \delta \dot{y} \end{bmatrix} = \cos(\omega_2 t)[A\boldsymbol{p}_2 + B\boldsymbol{q}_2] + \sin(\omega_2 t)[B\boldsymbol{p}_2 - A\boldsymbol{q}_2] + \cos(\omega_4 t)[C\boldsymbol{p}_4 + D\boldsymbol{q}_4] + \sin(\omega_4 t)[D\boldsymbol{p}_4 - C\boldsymbol{q}_4] \tag{4.7}$$

for arbitrary constants A, B, C, and D. By setting $t = 0$, the initial conditions

are found from Eq. (4.7) as

$$\begin{bmatrix} \delta x_0 \\ \delta y_0 \\ \delta \dot{x}_0 \\ \delta \dot{y}_0 \end{bmatrix} = \begin{bmatrix} -2\omega_2 B - 2\omega_4 D \\ A(h+\omega_2^2) + C(h+\omega_4^2) \\ 2\omega_2^2 A + 2\omega_4^2 C \\ \omega_2(h+\omega_2^2)B + \omega_4(h+\omega_4^2)D \end{bmatrix} \tag{4.8}$$

where $h = 2\sigma_i + 1$. The constants A, B, C, and D are then found to be

$$\begin{bmatrix} A \\ B \\ C \\ D \end{bmatrix} = \begin{bmatrix} -\frac{-h\delta\dot{x}_0 - \delta\dot{x}_0\omega_4^2 + 2\delta y_0\omega_4^2}{2h(\omega_2^2-\omega_4^2)} \\ -\frac{-2\delta\dot{y}_0 - h\delta x_0 - \delta x_0\omega_4^2}{2\omega_2(\omega_2^2-\omega_4^2)} \\ -\frac{-h\delta\dot{x}_0 - \delta\dot{x}_0\omega_2^2 + 2\delta y_0\omega_2^2}{2h(\omega_4^2-\omega_2^2)} \\ -\frac{-2\delta\dot{y}_0 - h\delta x_0 - \delta x_0\omega_2^2}{2\omega_4(\omega_4^2-\omega_2^2)} \end{bmatrix} \tag{4.9}$$

In order to remove the real modes of the motion, it is necessary that $C = D = 0$. The initial conditions required for this can then be found by substituting $C = 0$ and $D = 0$ into Eq. (4.7), such that

$$\delta x = -2\omega_2 B\cos(\omega_2 t) + 2\omega_2 A\sin(w_2 t) \tag{4.10a}$$

$$\delta y = A(h+\omega_2^2)\cos(\omega_2 t) + B(h+\omega_2^2)\sin(\omega_2 t) \tag{4.10b}$$

Constants A and B can be found in terms of the initial conditions by substituting $t = 0$ into Eq. (4.10), yielding

$$A = \frac{\delta y_0}{h+\omega_2^2} \tag{4.11a}$$

$$B = \frac{\delta x_0}{-2\omega_2} \tag{4.11b}$$

The required initial velocities are found by substituting Eq. (4.11) into Eq.(4.8), such that

$$\begin{bmatrix} \delta\dot{x}_0 \\ \delta\dot{y}_0 \end{bmatrix} = \begin{bmatrix} \frac{2\delta y_0 \omega_2^2}{h+\omega_2^2} \\ \frac{-\delta x_0 (h+\omega_2^2)}{2} \end{bmatrix} \tag{4.12}$$

Equation (4.11) can then be substituted into Eq. (4.10), so a periodic solution [96] which depends on a single natural frequency ω_2 is found as

$$\delta x(t) = -A_{\delta x} \cos(\omega_2 t + \phi) \tag{4.13a}$$

$$\delta y(t) = k A_{\delta x} \sin(\omega_2 t + \phi) \tag{4.13b}$$

in which $k = \frac{(\omega_2^2+h)}{2\omega_2}$, $A_{\delta x}$ is the amplitude of the δx-axis motion, and ϕ is the phase angle. Both K_{11} and K_{22} can now be varied to change the natural frequency and δy-axis amplitude of the elliptical relative orbit around the Lagrange point. The out-of-plane motion, which is always periodic, has solution

$$\delta z(t) = A_{\delta z} \sin(\omega_6 t + \phi_z) \tag{4.14}$$

where $A_{\delta z}$ is the δz-axis amplitude, ϕ_z is the phase angle, and ω_6 is the out-of-plane natural frequency which can be modified by changing K_{33}. The periodic in-plane motion generated by these initial conditions is shown in Fig. 4.4, where $K_{11} = K_{22} = 10\sigma_2$, $x_0 = 1000$ km, $y_0 = 0$, and the initial velocity is given by Eq. (4.12). These Figures were generated using Mathematica's NDSolve and ParametricPlot functions.

It can then be shown that 3-dimensional periodic orbits are achieved when ω_2/ω_6 is a rational number, and quasi-periodic Lissajous trajectories are obtained when ω_2/ω_6 is irrational. An example of a thrust augmented Lissajous trajectory is shown in Fig. 4.5, where $K_{11} = K_{22} = 10\sigma_2$ and $K_{33} = 0$. These Figures were generated using Mathematica's NDSolve and ParametricPlot functions.

To achieve 3-dimensional periodic orbits of arbitrary dimensions, as opposed to searching for naturally occurring halo orbit solutions, it is useful to apply thrust to synchronise the in-plane and out-of-plane natural frequencies. It is

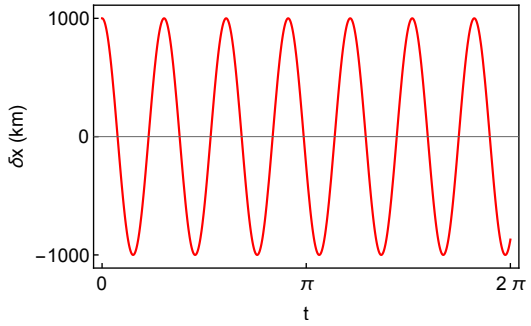

(a) δx-axis position over time.

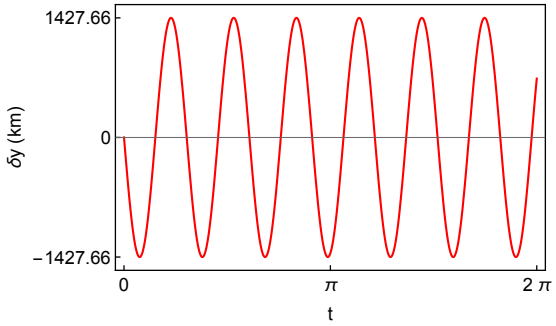

(b) δy-axis position over time.

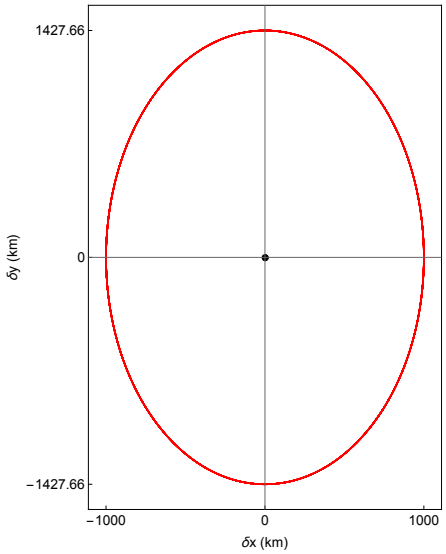

(c) $\delta x - \delta y$ plane.

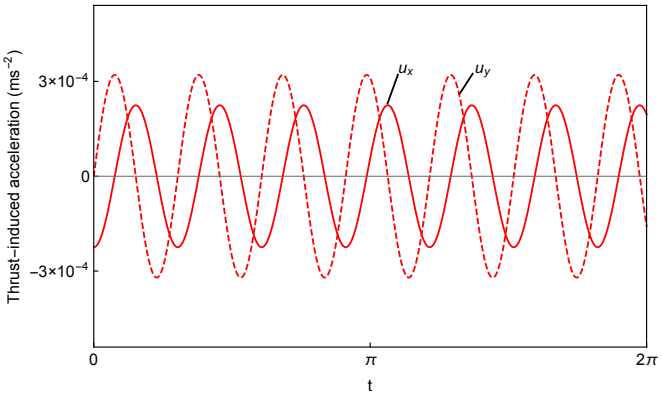

(d) Required acceleration.

Figure 4.4: Periodic in-plane trajectory, using $K_{11} = K_{22} = 10\sigma_2$. Figures (a) and (b) show the δx and δy positions of the spacecraft over time, (c) shows the orbit in the $\delta x - \delta y$ plane, and (d) shows the required thrust-induced acceleration. Initial conditions are $\delta x_0 = 1000$ km, $\delta y_0 = 0$, $\delta \dot{x}_0 = 2(\delta y_0 \omega_2^2)/(2\sigma_i - K_{11} + 1 + \omega_2^2)$, and $\delta \dot{y}_0 = -\delta x_0(2\sigma_i - K_{11} + 1 + \omega_2^2)/2$. The black point indicates the location of L_2.

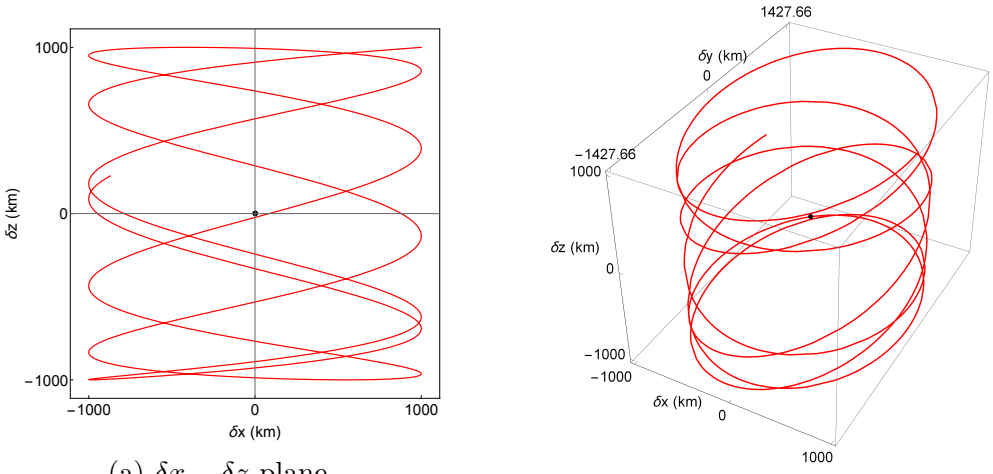

(a) $\delta x - \delta z$ plane.

(b) 3-D trajectory.

Figure 4.5: Thrust augmented Lissajous trajectory about Earth-Moon L_2 point, using $K_{11} = K_{22} = 10\sigma_2$ and $K_{33} = 0$. Initial conditions are $\delta x_0 = \delta z_0 = 1000$ km, $\delta y_0 = 0$, $\delta \dot{x}_0 = 2(\delta y_0 \omega_2^2)/(2\sigma_i - K_{11} + 1 + \omega_2^2)$, $\delta \dot{y}_0 = -\delta x_0(2\sigma_i - K_{11} + 1 + \omega_2^2)/2$, and $\delta \dot{z}_0 = 0$. The black point indicates the location of L_2.

most simply achieved by properly selecting the out-of-plane feedback gain (K_{33}), since λ_6 depends only on K_{33}. In Eq. (4.6), choosing $\lambda_6 = \lambda_2$ for $\omega_6 = \omega_2$, yields

$$K_{33} = \frac{2 + K_{11} + K_{22} - 3\sigma_i + \sqrt{K_{11}^2 + 8(K_{22} - \sigma_i) - 2K_{11}(-4 + K_{22} + 3\sigma_i) + (K_{22} + 3\sigma_i)^2}}{2} \tag{4.15}$$

This produces a tilted periodic orbit with a potential application in providing an L_2 communications relay for the far side of the Moon with respect to the Earth, as an extension of the concept first proposed by Farquhar in 1968 [62]: instead of out-of-plane phase-jump control impulses, continuous low thrust with out-of-plane gain defined by Eq. (4.15) is used to control the out-of-plane natural frequency of the spacecraft, preventing occultation behind the Moon. Constant line-of-sight with the Earth is achieved by ensuring that $A_{\delta x}$ and $A_{\delta z}$ are greater than the radius of the cone-shaped occluded region behind the Moon as viewed from the Earth. A schematic showing the configuration of this kind of orbit in the Earth-Moon system is given in Fig. 4.6. The in-plane and 3-dimensional

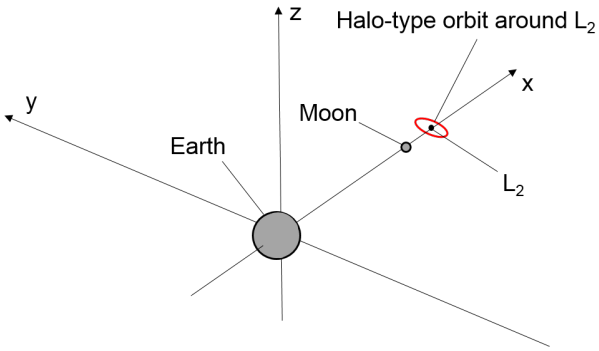

Figure 4.6: Schematic of the Earth-Moon system and thrust augmented halo-type orbit. Note that this schematic is not to scale.

trajectories of a spacecraft on such an orbit around the Earth-Moon L_2 are shown in Fig. 4.7, for $A_{\delta x} = A_{\delta z} = 1800$ km. These Figures were generated using Mathematica's NDSolve and ParametricPlot functions. For this example orbit, with zero thrust in the in-plane directions, the peak thrust-induced acceleration in the δz-axis is 3.56 μm s^{-2}. The required Δv_z for one year of operation is 74.4 m s^{-1}, corresponding to a 25 g propellant expenditure for a spacecraft with initial mass of 10 kg, equipped with electrostatic thrusters of $I_{sp} = 3000$ s. It has already been stated in Chapter 3 that this is a very small quantity of Xenon, since even a 3 kg nanosatellite could feasibly carry 1.5 kg of this propellant [116].

4.4 Conclusions

The method proposed in Chapter 3, where continuous low thrust propulsion is used to generate rich new families of stable relative orbits, can be applied to the circular restricted three body problem. The dynamics of a spacecraft relative to a libration point can be linearised, and this linearisation allows direct modification of the natural frequencies of motion through manipulation of the system eigenvalues, again using position-only feedback. The dynamics close to the collinear Lagrange points, though unstable under zero-thrust conditions, can be made stable in this way, allowing both quasi- and multiply-periodic orbits to

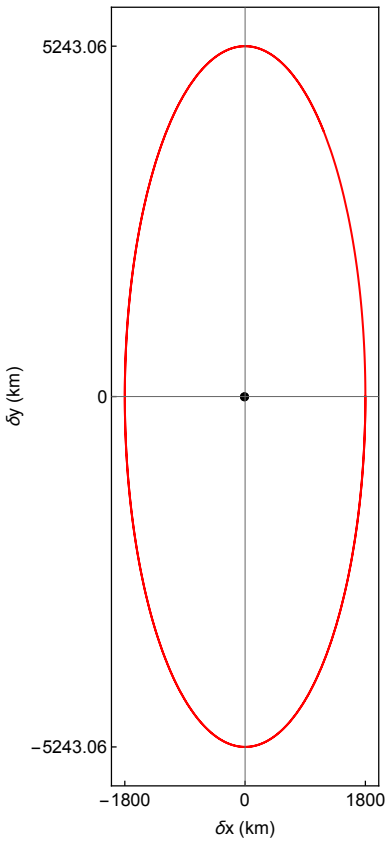

(a) In-plane trajectory.

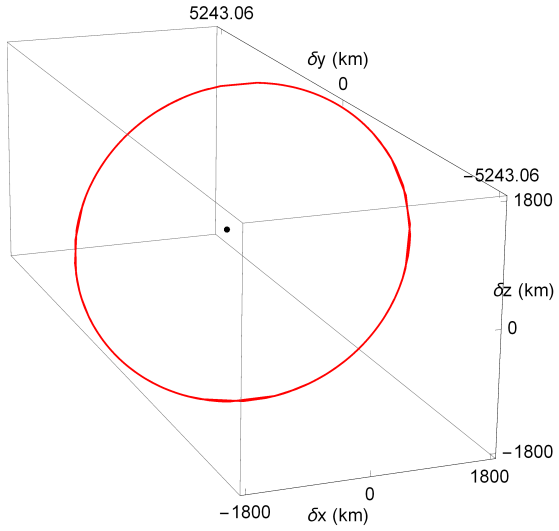

(b) Three-dimensional trajectory.

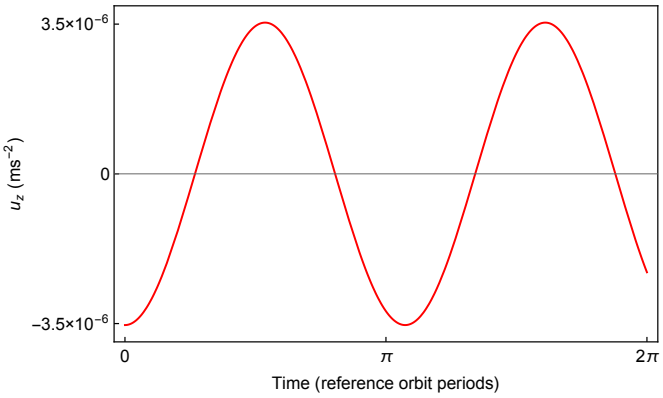

(c) Required acceleration.

Figure 4.7: Trajectory around Earth-Moon L_2 point when $\omega_2 = \omega_6$, using $K_{11} = K_{22} = 0$, and K_{33} is given by Eq. (4.15). Figure (a) shows the in-plane trajectory of the spacecraft, (b) shows the three-dimensional trajectory, and (c) shows the required thrust-induced acceleration. Initial conditions are $\delta x_0 = \delta z_0 = 1800$ km, $\delta y_0 = 0$, $\delta \dot{x}_0 = 2(\delta y_0 \omega_2^2)/(2\sigma_i - K_{11} + 1 + \omega_2^2)$, $\delta \dot{y}_0 = -\delta x_0(2\sigma_i - K_{11} + 1 + \omega_2^2)/2$, and $\delta \dot{z}_0 = 0$. The black point indicates the location of L_2.

be designed. Furthermore, the in-plane and out-of-plane natural frequencies can be synchronised using continuous thrust, such that a stable, singly-periodic 3-dimensional orbit around a libration point can be generated. This orbit, if at the Earth-Moon L_2 point, could provide a constantly visible communications relay for lunar far-side missions. As in Chapter 3, the use of simple control strategies requiring only position feedback would permit implementation on-board small, low-cost spacecraft. Additionally, the propellant requirements for these new orbit families are generally small, assuming the use of modern electrostatic thrusters.

Chapter 5

Artificial Horseshoe Orbits in the Hill-Clohessy-Wiltshire Approximation

This Chapter addresses Objective 3 as described in Section 1.3, by developing a method for replicating certain aspects of three-body co-orbital motion by using low thrust in the two-body HCW approximation, in order to provide access to new and interesting phased spacecraft constellations. Section 5.1 gives the thrust augmented HCW equations of motion in cylindrical-polar form, Section 5.2 describes a strategy for generating a horseshoe orbit in the HCW approximation using thrust along a single axis and derives the necessary thrust commands, Section 5.3 derives the thrust commands along two axes for the generation of a horseshoe orbit with circular inner and outer orbits, and Section 5.4 applies the modified out-of-plane motion of Chapter 3 to these horseshoe orbits, showing that considerable utility can be added to the concept with this addition. Section 5.5 offers a discussion of the applications of the new relative orbits, and finally Section 5.6 provides conclusions for the Chapter. The basic concept of a horseshoe orbit has been described in Chapter 1, and a schematic of a horseshoe orbit in the CRTBP was shown in Fig. 1.4.

5.1 Equations of Motion

The work presented in this Chapter is based on the cylindrical-polar form of the HCW equations. The cylindrical-polar form of the HCW approximation is used since the along-track coordinate of the Cartesian form is a straight axis and therefore diverges from the reference orbit if along-track displacement is large. In the cylindrical-polar form, $\delta\theta$ describes only a change in polar angle with respect to the target point on the circular reference orbit, and so is correct for any change in along-track displacement. Broucke and Konopliv used these equations to generate approximate models of the motion of Saturn's co-orbital satellites, Janus and Epimethus [97]. The equations are given in cylindrical coordinates δr, $\delta\theta$, and δz and augmented with thrust terms as [110]

$$\delta\ddot{r} = 2nr_0\delta\dot{\theta} + 3n^2\delta r + u_r \tag{5.1a}$$

$$\delta\ddot{\theta} = \frac{-2n\delta\dot{r} + u_\theta}{r_0} \tag{5.1b}$$

$$\delta\ddot{z} = -n^2\delta z + u_z \tag{5.1c}$$

where n and r_0 have their usual meaning as the mean motion and radius of the reference orbit, and u_r, u_θ, and u_z are the thrust-induced accelerations in the radial, along-track, and out-of-plane directions, respectively. A schematic of this frame of reference is provided in Fig. 5.1. Since Eq. (5.1c) is decoupled from the other two equations, it is possible to consider the in-plane and out-of-plane motion separately, as was shown in Chapter 3.

The general solution to Eq. (5.1) when the thrust-induced acceleration is zero is given as [110]

$$\delta r(t) = -\left(\frac{2}{n}r_0\delta\dot{\theta}_0 + 3\delta r_0\right)\cos(nt) + \frac{\delta\dot{r}_0}{n}\sin(nt) + 4\delta r_0 + \frac{2}{n}r_0\delta\dot{\theta}_0 \tag{5.2a}$$

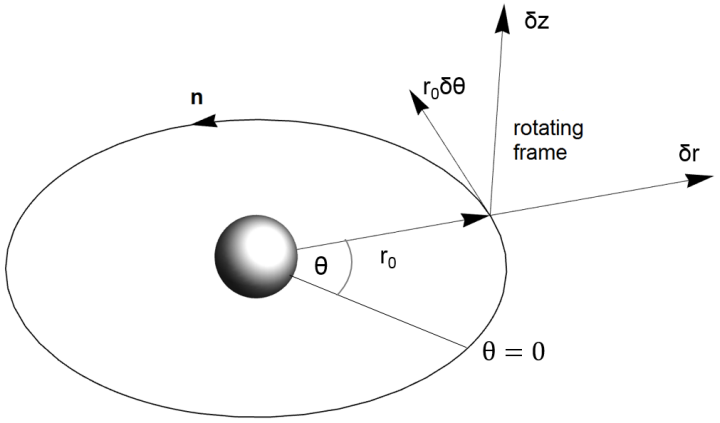

Figure 5.1: Schematic of the rotating frame of reference with cylindrical-polar form.

$$\delta\theta(t) = \delta\theta_0 - \left(3\delta\dot{\theta}_0 + \frac{6n\delta r_0}{r_0}\right)t + \left(\frac{4\delta\dot{\theta}_0}{n} + \frac{6\delta r_0}{r_0}\right)\sin(nt) + \frac{2\delta\dot{r}_0}{nr_0}\cos(nt) - \frac{2\delta\dot{r}_0}{nr_0} \tag{5.2b}$$

$$\delta z(t) = \delta z_0 \cos(nt) + \frac{\delta\dot{z}_0}{n}\sin(nt) \tag{5.2c}$$

The solution for the velocity terms is then given as

$$\delta\dot{r}(t) = (2r_0\delta\dot{\theta}_0 + 3n\delta r_0)\sin(nt) + \delta\dot{r}_0\cos(nt) \tag{5.3a}$$

$$\delta\dot{\theta}(t) = \delta\dot{\theta}_0 + \frac{2n}{r_0}(\delta r_0 - \delta r) \tag{5.3b}$$

$$\delta\dot{z}(t) = -\delta z_0 n\sin(nt) + \delta\dot{z}_0\cos(nt) \tag{5.3c}$$

5.2 Transfers Using Single-Axis Thrust

A horseshoe orbit in the CRTBP can be considered in a simplified form as two orbits, one of greater and one of lesser semi-major axis, connected by two arcs during which the gravity of the smaller primary applies an along-track acceler-

ation (or deceleration) to the particle. Such behaviour can be replicated in the HCW approximation.

In essence, this orbit will be comprised of two symmetric transfer manoeuvres, one to lower the orbit and another to raise it again, connected by two free-flying trajectories. The manoeuvres will use constant thrust-induced acceleration in the $\delta\theta$-direction only. Such an orbit can be described analytically, using the free-flying solution given in Eq. (5.2) for the inner and outer orbits, and a solution for the position with constant along-track acceleration for the two manoeuvres. The solution with constant acceleration can be obtained as follows.

Assuming only along-track thrust, $u_r = u_z = 0$, it is possible to rewrite Eq. (5.1b) as

$$\frac{d}{dt}(r_0\delta\dot{\theta} + 2n\delta r) - u_\theta = 0 \tag{5.4}$$

which can be immediately integrated to yield

$$\delta\dot{\theta}(t) = \delta\dot{\theta}_0 + \frac{2n}{r_0}(\delta r_0 - \delta r) + \frac{u_\theta t}{r_0} \tag{5.5}$$

This can then be substituted into Eq. (5.1a) to give

$$\delta\ddot{r} = 2nr_0\Big(\delta\dot{\theta}_0 + \frac{2n}{r_0}(\delta r_0 - \delta r) + \frac{u_\theta}{r_0}\Big) + 3n^2\delta r \tag{5.6}$$

which is a simple harmonic oscillator with a forcing term. This can be solved in the usual manner [110], with homogeneous and particular solutions, to find the complete radial solution including u_θ, given as

$$\begin{aligned}\delta r(t) = \frac{1}{n^2}\Big(&2n(u_\theta t + r_0\delta\dot{\theta}_0 + 2n\delta r_0) - n(2r_0\delta\dot{\theta}_0 + 3n\delta r_0)\cos(nt) \\ &+ (n\delta\dot{r}_0 - 2u_\theta)\sin(nt)\Big)\end{aligned} \tag{5.7}$$

This is then substituted into Eq. (5.5) and integrated to find the along-track

solution, which is

$$\delta\theta(t) = \frac{1}{2n^2 r_0}\Big(u_\theta(8-3n^2t^2) - 2n(2\delta\dot{r}_0 + n(3r_0t\delta\dot{\theta}_0 + 6nt\delta r_0 - r_0\delta\theta_0)) + (4n\delta\dot{r}_0 - 8u_\theta)\cos(nt) + 4n(2r_0\delta\dot{\theta}_0 + 3n\delta r_0)\sin(nt)\Big) \tag{5.8}$$

Taking the derivative of Eq. (5.7) yields the solution for radial velocity as

$$\delta\dot{r}(t) = \frac{1}{n^2}\Big(2n(u_\theta t + 2n\delta r_0 + r_0\delta\dot{\theta}_0) + (n\delta\dot{r}_0 - 2u_\theta)\sin(nt) - n\cos(nt)(3n\delta r_0 + 2r_0\delta\dot{\theta})\Big) \tag{5.9}$$

Now that the full set of free-flying and powered arc solutions have been obtained, they will be used to describe the four sections of the orbit. The state of the system at each transition between free-flying and powered arcs must be defined. There are five transitions (including the initial state), so that the time of each transition can be denoted by t_i where $i = 0$ - 4. Thus, the spacecraft will perform the following sequence:

- At $t = t_0$, the spacecraft is injected with initial conditions corresponding to a free-flying circular orbit of greater radius than the reference orbit, and thrust is enabled such that $u_\theta \neq 0$. It can be seen by substituting $u_\theta = \delta\dot{x}_0 = 0$ into Eq. (5.7) that the necessary initial along-track velocity is $\delta\dot{\theta}_0 = -3n\delta r_0/2r_0$ such that the solution for radial motion reduces to $\delta r(t) = \delta r_0$.

- At $t = t_1$, the thrust is disabled ($u_\theta = 0$), and the spacecraft is injected into a free-flying orbit of smaller semi-major axis than the reference orbit. The spacecraft now moves with $\delta\dot{\theta}_1$ which is in the opposite direction to $\delta\dot{\theta}_0$.

- At $t = t_2$, the thrust is enabled in the opposite direction to that of $t = t_0$, in order to raise the spacecraft's orbit.

- At $t = t_3$, the thrust is disabled and the spacecraft is returned to the initial free-flying circular orbit.

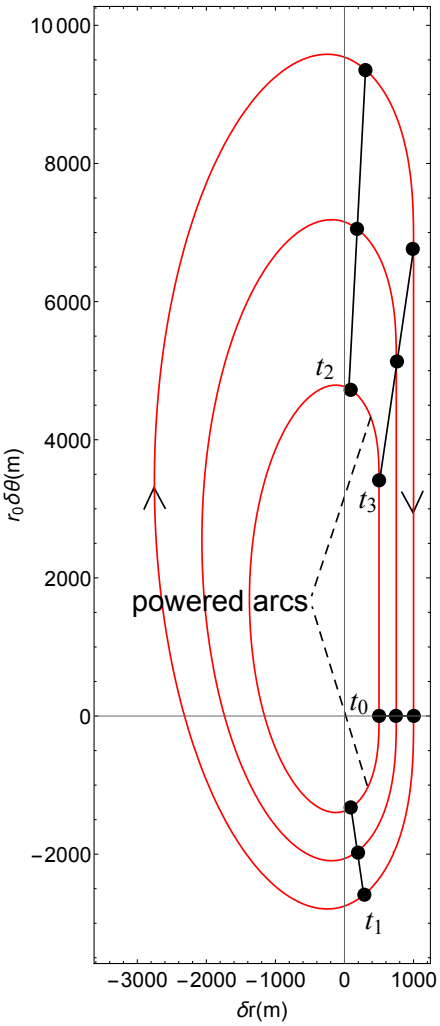

Figure 5.2: Nested horseshoe orbits using along-track thrust-induced acceleration between times t_0 and t_1, then t_2 and t_3. Initial conditions are $r_0 = 42157 \times 10^3$ m, $\delta r_0 = [500, 750, 1000]^T$ m, $\delta\theta_0 = \delta\dot{r}_0 = 0$, $\delta\dot{\theta}_0 = -3n\delta r_0/2r_0$.

- At $t = t_4$, the spacecraft has returned to its initial conditions.

An example of this type of relative orbit is given in Fig. 5.2, (Figure generated using Mathematica's NDSolve and ParametricPlot functions) for which the analytical description is as follows.

5.2.1 The Initial and Final Orbits

For the initial orbit of the spacecraft to be circular in the inertial frame (constant δr in the rotating frame), the necessary initial along-track velocity is $\delta\dot{\theta}_0 = -3n\delta r_0/2r_0$.

To simplify the derivation, it is assumed here that the horseshoe orbit completes after some multiple of $2T$, where T is the reference orbit period. An initial along-track position of $\delta\theta_0 = 0$ is selected for simplicity. The orbit can now be defined with a piecewise function in four parts, where the two free-flying parts use the solution in Eq. (5.2), and the two manoeuvre parts use the solution from Eq. (5.7) and Eq. (5.8), such that the functions describing the position are given by

$$\delta r(t) = \begin{cases} \dfrac{1}{n^2}\Big(2n(u_\theta t + r_0\delta\dot{\theta}_0 + 2n\delta r_0) \\ \quad - n(2r_0\delta\dot{\theta}_0 + 3n\delta r_0)\cos(nt) & \text{if } t_0 \le t \le t_1 \\ \quad + (n\delta\dot{r}_0 - 2u_\theta)\sin(nt)\Big) \\ \\ -\left(\dfrac{2}{n}r_0\delta\dot{\theta}_1 + 3\delta r_1\right)\cos(nt) & \\ \quad + \dfrac{\delta\dot{r}_1}{n}\sin(nt) + 4\delta r_1 + \dfrac{2}{n}r_0\delta\dot{\theta}_1 & \text{if } t_1 \le t \le t_2 \\ \\ \dfrac{1}{n^2}\Big(2n(u_\theta t + r_0\delta\dot{\theta}_2 + 2n\delta r_2) \\ \quad - n(2r_0\delta\dot{\theta}_2 + 3n\delta r_2)\cos(nt) & \text{if } t_2 \le t \le t_3 \\ \quad + (n\delta\dot{r}_2 - 2u_\theta)\sin(nt)\Big) \\ \\ -\left(\dfrac{2}{n}r_0\delta\dot{\theta}_3 + 3\delta r_3\right)\cos(nt) & \\ \quad + \dfrac{\delta\dot{r}_3}{n}\sin(nt) + 4\delta r_3 + \dfrac{2}{n}r_0\delta\dot{\theta}_3 & \text{if } t_3 \le t \le t_4 \end{cases} \tag{5.10a}$$

$$\delta\theta(t) = \begin{cases} \dfrac{1}{2n^2 r_0}\Big(u_\theta(8-3n^2t^2) \\ \quad -2n(2\delta\dot{r}_0 + n(3r_0 t\delta\dot{\theta}_0 + 6nt\delta r_0 - r_0\delta\theta_0)) \\ \quad +(4n\delta\dot{r}_0 - 8u_\theta)\cos(nt) \\ \quad +4n(2r_0\delta\dot{\theta}_0 + 3n\delta r_0)\sin(nt)\Big) & \text{if } t_0 \le t \le t_1 \\ \delta\theta_1 - \left(3\delta\dot{\theta}_1 + \dfrac{6n\delta r_1}{r_0}\right)t \\ \quad +\left(\dfrac{4\delta\dot{\theta}_1}{n} + \dfrac{6\delta r_1}{r_0}\right)\sin(nt) & \text{if } t_1 \le t \le t_2 \\ \quad +\dfrac{2\delta\dot{r}_1}{nr_0}\cos(nt) - \dfrac{2\delta\dot{r}_1}{nr_0} \\ \dfrac{1}{2n^2 r_0}\Big(u_\theta(8-3n^2t^2) \\ \quad -2n(2\delta\dot{r}_2 + n(3r_0 t\delta\dot{\theta}_2 + 6nt\delta r_2 - r_0\delta\theta_2)) \\ \quad +(4n\delta\dot{r}_2 - 8u_\theta)\cos(nt) \\ \quad +4n(2r_0\delta\dot{\theta}_2 + 3n\delta r_2)\sin(nt)\Big) & \text{if } t_2 \le t \le t_3 \\ \delta\theta_3 - \left(3\delta\dot{\theta}_3 + \dfrac{6n\delta r_3}{r_0}\right)t \\ \quad +\left(\dfrac{4\delta\dot{\theta}_3}{n} + \dfrac{6\delta r_3}{r_0}\right)\sin(nt) & \text{if } t_3 \le t \le t_4 \\ \quad +\dfrac{2\delta\dot{r}_3}{nr_0}\cos(nt) - \dfrac{2\delta\dot{r}_3}{nr_0} \end{cases} \tag{5.10b}$$

and the functions describing the velocity terms are given by

$$\delta\dot{r}(t) = \begin{cases} \frac{1}{n^2}\Big(2n(u_\theta t + 2n\delta r_0 + r_0\delta\dot{\theta}_0) & \\ + (n\delta\dot{r}_0 - 2u_\theta)\sin(nt) & \text{if } t_0 \le t \le t_1 \\ - n\cos(nt)(3n\delta r_0 + 2r_0\delta\dot{\theta})\Big) & \\ (2r_0\delta\dot{\theta}_1 + 3n\delta r_1)\sin(nt) & \\ + \delta\dot{r}_1\cos(nt) & \text{if } t_1 \le t \le t_2 \\ \frac{1}{n^2}\Big(2n(u_\theta t + 2n\delta r_2 + r_0\delta\dot{\theta}_2) & \\ + (n\delta\dot{r}_2 - 2u_\theta)\sin(nt) & \text{if } t_2 \le t \le t_3 \\ - n\cos(nt)(3n\delta r_2 + 2r_0\delta\dot{\theta})\Big) & \\ (2r_0\delta\dot{\theta}_3 + 3n\delta r_3)\sin(nt) & \\ + \delta\dot{r}_3\cos(nt) & \text{if } t_3 \le t \le t_4 \end{cases} \tag{5.11a}$$

$$\delta\dot{\theta}(t) = \begin{cases} \delta\dot{\theta}_0 + \frac{2n}{r_0}(\delta r_0 - \delta r) + \frac{u_\theta t}{r_0} & \text{if } t_0 \le t \le t_1 \\ \delta\dot{\theta}_1 + \frac{2n}{r_0}(\delta r_1 - \delta r) & \text{if } t_1 \le t \le t_2 \\ \delta\dot{\theta}_2 + \frac{2n}{r_0}(\delta r_2 - \delta r) + \frac{u_\theta t}{r_0} & \text{if } t_2 \le t \le t_3 \\ \delta\dot{\theta}_3 + \frac{2n}{r_0}(\delta r_3 - \delta r) & \text{if } t_3 \le t \le t_4 \end{cases} \tag{5.11b}$$

In this way, the position and velocity of the spacecraft at any point on the orbit is known. It is then possible to find expressions for the final state of the system in terms of the initial conditions. When the initial and final orbits of the spacecraft

are identical, it can be shown that the final state of the system (when $t = t_4$) is

$$\begin{bmatrix} \delta r_4 \\ \delta\theta_4 \\ \delta\dot{r}_4 \\ \delta\dot{\theta}_4 \end{bmatrix} = \begin{bmatrix} \delta r_0 \\ -\frac{6\pi(u_\theta t_1 + n\delta r_0)}{n r_0} \\ 0 \\ -\frac{3n\delta r_0}{2r_0} \end{bmatrix} \tag{5.12}$$

5.2.2 The Required Thrust

Now that the initial state has been defined and the desired final state of the system has been found using the general solution, it is necessary to find the thrust-induced acceleration required to produce the manoeuvres between the inner and outer orbits. Consider Eq. (5.12), where it can be seen that $\delta\theta_4$ is the only term dependent on u_θ and t_1. It is therefore possible to solve for u_θ. By selecting $\delta\theta_4 = \delta\theta_0$, it is found that

$$u_\theta = \begin{cases} -\frac{n\delta r_0}{t_1} & \text{if } t_0 \leq t \leq t_1 \\ 0 & \text{if } t_1 \leq t \leq t_2 \\ \frac{n\delta r_0}{t_1} & \text{if } t_2 \leq t \leq t_3 \\ 0 & \text{if } t_3 \leq t \leq t_4 \end{cases} \tag{5.13}$$

where the relation $t_3 - t_2 = t_1$ is used, implying that the duration of both manoeuvres is identical. It is seen that the required acceleration can be found by selecting the initial radial displacement and the manoeuvre duration.

Using Eq. (5.13) to define the acceleration and by placing the spacecraft into the initial circular free-flying orbit, it is seen in Fig. 5.2 that the first manoeuvre (from $t = t_0$ to $t = t_1$) places the spacecraft onto an elliptical orbit with smaller semi-major axis than the reference orbit. The spacecraft then moves in the positive $\delta\theta$-direction on a free-flying trajectory. At $t = t_2 = T$, $u_\theta = \frac{n\delta r_0}{t_1}$ is applied until $t = t_3$, and the spacecraft is returned to its initial circular free-flying orbit. At $t = t_4 = 2T$, the relative orbit is completed and the spacecraft has returned

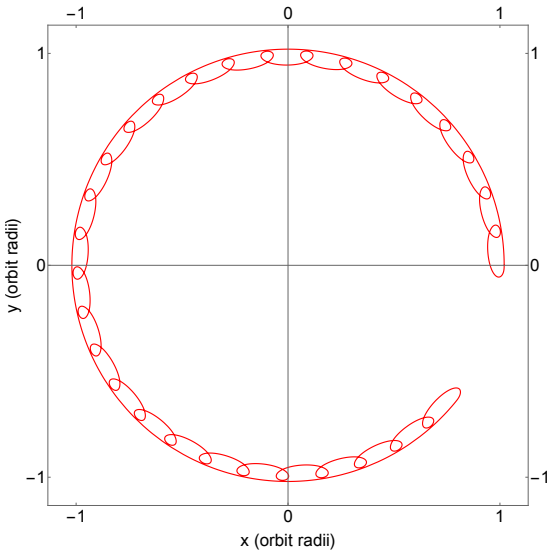

Figure 5.3: Long horseshoe orbit mapped to the Earth-centred rotating frame, using two transfers with single-axis thrust. The unit of measurement is the radius of the reference orbit. The relative orbit period is $60T$. Initial conditions are $r_0 = 1$, $\delta r_0 = r_0/50$, $\delta\theta_0 = \delta\dot{r}_0 = 0$, $\delta\dot{\theta}_0 = -3n\delta r_0/2r_0$.

to its initial conditions.

5.2.3 Longer Horseshoe Orbits

As long as the magnitudes of u_θ and t_1 are kept the same for both the deceleration and acceleration manoeuvres, the result is a repeating orbit of similar shape to the case in Fig. 5.2. However, as stated, the special property given by Eq. (5.13) is that the relative orbit completes in exactly two reference orbit periods. This property can be extended over any integer multiple of 2 orbit periods to form a longer horseshoe orbit. Figure 5.3 shows how this type of orbit maps to the Earth-centred rotating reference frame, with a relative orbit period of $60T$ and $\delta r_0 = r_0/50$.

Since the thrust-induced acceleration for this type of manoeuvre is constant, the required Δv for each manoeuvre can be calculated as $\Delta v = n\delta r_0$. Using the example of an initial radial displacement of 1000 metres above geostationary orbit, as in Fig. 5.2, the Δv required for one full horseshoe orbit (two symmetric

manoeuvres) is less than 0.15 ms^{-1}.

As long as the thrust magnitude and duration obey Eq. (5.13), different initial radial displacements may be selected for a constellation of spacecraft to occupy nested horseshoe orbits, each with the same relative orbit period. This permits the generation of new families of phased constellations with diverse applications. As an example, it can be envisaged that a constellation of spacecraft on synchronised, nested orbits around the geostationary ring could be reconfigured with these simple manoeuvres to provide a greater density of spacecraft over particular longitudes at particular times, permitting enhanced coverage for services such as satellite telecommunications according to demand.

5.3 Transfers Using Dual-Axis Thrust

A geometrically simple and operationally advantageous orbit is one composed of two circular orbits of different radii, connected by powered arcs. As in Section 5.2, thrust is only necessary for the duration of the transfer from the higher to lower orbit or vice-versa. In this Section, it is proposed that these transfers are achieved using continuous thrust along two axes (along-track and radial) to change the semi-major axis and eccentricity of the orbit such that the inner and outer orbits of the horseshoe are circular in the Earth-centred frame.

Normally, bounded motion in the HCW system is elliptical in shape, obtained by cancelling the secular term of the solution by selecting $\delta\dot{\theta} = -2n\delta r_0/r_0$. In Chapter 3, it was shown that thrust-induced acceleration in the radial direction of $u_x = -3n^2x$ results in circular in-plane relative motion with the same initial conditions as the free-flying elliptical case. In cylindrical-polar form, this acceleration has the form $u_r = -3n^2\delta r$. This acceleration alone cannot be used for a transfer, since it is purely radial and therefore does not affect the semi-major axis of the spacecraft's orbit. Furthermore, to ensure that the inner and outer orbits are circular in the Earth-centred frame, the along-track velocity before

and after the transfer must be $\delta\dot{\theta}_0 = -\delta\dot{\theta}_1 = -3n\delta r_0/(2r_0)$, as shown in Section 5.2.1. Figure 5.4 shows the type of trajectory which results from a manoeuvre using only radial thrust, where it can be noted that the semi-major axis of the pre- and post-manoeuvre orbits are the same. This Figure were generated using Mathematica's NDSolve and ParametricPlot functions.

A constant along-track acceleration may be added to this radial acceleration to produce the required transfer. It is first necessary to find the general solutions to the in-plane part of Eq. (5.1) when $u_r = -3n^2\delta r$ and u_θ is constant. These are found to be

$$\begin{aligned}\delta r(t) = &-\frac{1}{4n^2}\Big(-2n(2\delta r_0 n + u_\theta t + r_0\delta\dot{\theta}_0) + 2nr_0\delta\dot{\theta}_0\cos(2nt) \\ &+ (u_\theta - 2n\delta\dot{r}_0)\sin(2nt)\Big)\end{aligned} \tag{5.14a}$$

$$\begin{aligned}\delta\theta(t) = &\frac{1}{4n^2r_0}\Big(u_\theta + 4\delta\theta_0 n^2 r_0 - 2n\delta\dot{r}_0 - (u_\theta - 2n\delta\dot{r}_0)\cos(2nt) \\ &+ 2nr_0\delta\dot{\theta}_0\sin(2nt)\Big)\end{aligned} \tag{5.14b}$$

Taking the derivative yields the general solution for the velocity terms as

$$\delta\dot{r}(t) = \frac{1}{2n}\Big(u_\theta - (u_\theta - 2n\delta\dot{r}_0)\cos(2nt) + 2nr_0\delta\dot{\theta}_0\sin(2nt)\Big) \tag{5.15a}$$

$$\delta\dot{\theta}(t) = \delta\dot{\theta}_0\cos(2nt) + \frac{1}{2nr_0}\Big((u_\theta - 2n\delta\dot{r}_0)\sin(2nt)\Big) \tag{5.15b}$$

It is then necessary to define the initial and final conditions of the manoeuvre. Assuming that the manoeuvre takes place at the crossing of the δr axis, and ends when the spacecraft re-crosses the same axis, the initial and final along-track positions are $\delta\theta_0 = \delta\theta_1 = 0$. Since the initial orbit and final orbits must be circular in the Earth-centred frame, it is necessary that $\delta\dot{\theta}_0 = -\delta\dot{\theta}_1 = -3n\delta r_0/(2r_0)$. Substituting $\delta r_1 = -\delta r_0$ into Eq. (5.14a) and $\delta\dot{r}_0 = 0$ into Eq. (5.15a) and

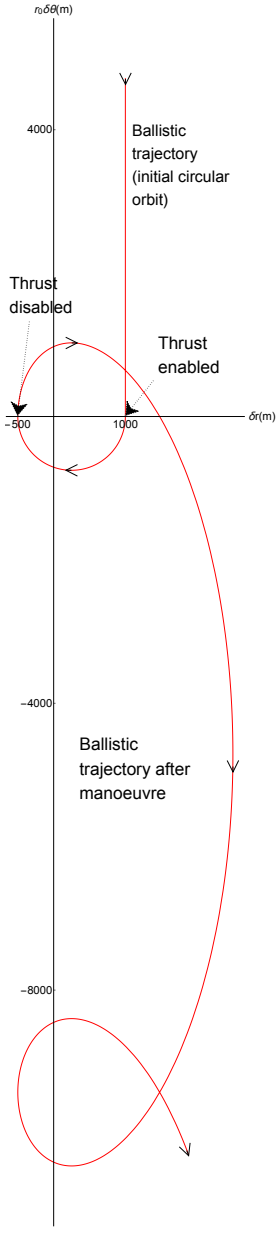

Figure 5.4: Trajectory before and after radial thrust manoeuvre, where $r_0 = 42157 \times 10^3$ m, $\delta r_0 = 1000$ m, $\delta\theta_0 = \delta\dot{r}_0 = 0$, and $\delta\dot{\theta}_0 = -3n\delta r_0/2r_0$.

solving for u_θ in each yields two different expressions for the required thrust-induced acceleration. These are

$$u_\theta = \frac{2n\Big(\delta\dot{r}_0 \cos(2nt) + r_0\delta\dot{\theta}_0 \sin(2nt))\Big)}{\cos 2nt - 1} \tag{5.16a}$$

$$u_\theta = -\frac{2n\Big(r_0\delta\dot{\theta}_0 + 4n\delta r_0 - r_0\delta\dot{\theta}_0 \cos(2nt) + \delta\dot{r}_0 \sin(2nt)\Big)}{2nt - \sin(2nt)} \tag{5.16b}$$

where $t = t_1$.

Letting Eq. (5.16a) equal Eq. (5.16b) and solving for t yields the duration of the manoeuvre. Once t_1 is known, it can be substituted into either equation to find the required acceleration. Furthermore, when $t = t_1$, it can be noted that Eq. (5.16a) and Eq. (5.16b) are equal to Eq. (5.13). It should also be noted that for the dual-axis case, t_1 is dependent only on the dynamics of the system and not the initial displacement of the spacecraft. Therefore, a manoeuvre beginning at any initial radial position will have the same duration. An example showing how these manoeuvres allow for nested equiperiodic orbits is given in Fig. 5.5, for $\delta r_0 = 250$, 500, and 1000 m (Figure generated using Mathematica's NDSolve and ParametricPlot functions). The orbit is completed by performing the opposite manoeuvre after an arbitrary time to return to the original trajectory. A schematic illustrating how this type of relative orbit maps to the Earth-centred rotating frame is given in Fig. 5.6.

A single complete horseshoe orbit using dual-axis transfers (assuming independent axis-aligned thrusters) with $\delta r_0 = 1000$ m requires $\Delta v = 0.64$ ms^{-1}, of which approximately 0.5 ms^{-1} is the radial component. This expenditure is directly proportional to δr_0.

Although thrust which is proportional to displacement is required in the radial direction, and this adds complexity to the spacecraft control, it can be seen that this type of orbit provides great utility since the transfers are geometrically simple and the initial and final orbits are circular. The duration of the manoeuvre is

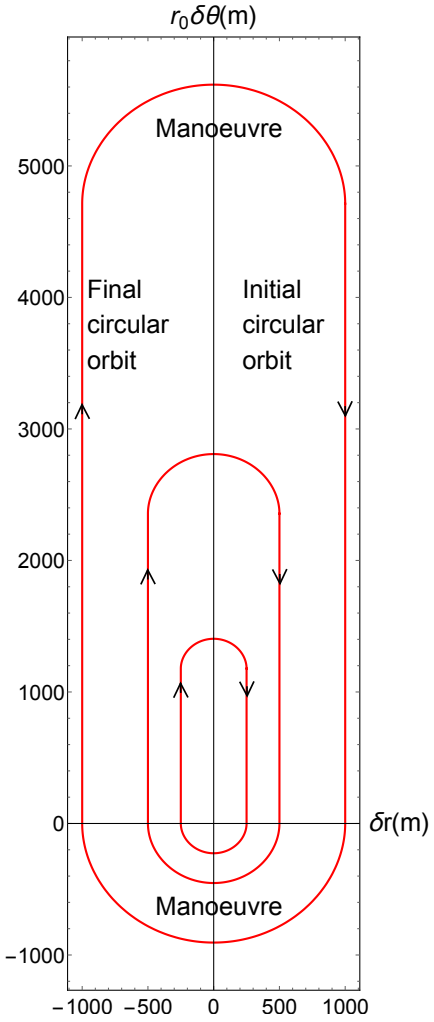

Figure 5.5: Nested orbits with equal period, using manoeuvres with dual-axis thrust. Initial conditions are $r_0 = 42157 \times 10^3$ m, $\delta r_0 = 250, 500$, and 1000 m, $\delta\theta_0 = \delta\dot{r}_0 = 0$, and $\delta\dot{\theta}_0 = -3n\delta r_0/2r_0$. The GEO ring is located at $\delta r = 0$.

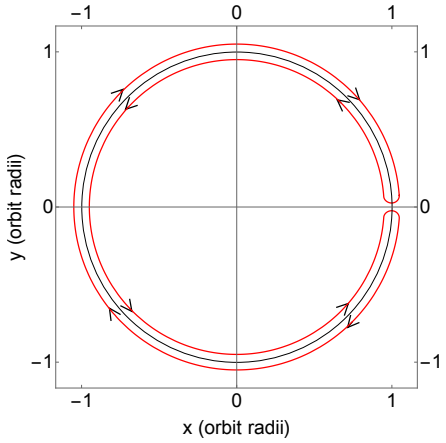

Figure 5.6: Schematic of horseshoe orbit with dual-axis transfers mapped to Earth-centred rotating frame. The radius of the reference orbit is shown as a black circle.

constant regardless of initial displacement from the reference orbit, which allows for synchronised or phased nested formations of spacecraft. Such formations could find applications in space situational awareness missions, by performing an inspection of the entire geostationary ring, or, as already suggested, by permitting constellations with different concentrations of spacecraft over certain longitudes at particular times, according to telecommunications demand.

5.4 Three-Axis Motion

The previous Sections have introduced two different methods for generating artificial horseshoe orbits using low thrust transfers, considering only in-plane motion. In this Section, out-of-plane motion is introduced, adding to the potential utility of the concept. Since δz-axis motion is decoupled from the other two axes, it can be developed entirely separately.

With zero thrust, motion along the δz-axis is that of a simple harmonic oscillator with period equal to that of the reference orbit, i.e. $T_z = 2\pi/n$. Combined with the in-plane artificial horseshoe motion, even this free-flying case generates interesting three-dimensional trajectories and greatly expands the available ar-

chitectures for nested constellations. However, greater versatility can be found when continuous thrust is also used to modify the out-of-plane natural frequency.

As in Chapter 3, it is possible to change the natural frequency of the out-of-plane oscillations by making the thrust-induced acceleration proportional to the displacement δz. Considering Eq. (5.1c), this is achieved by selecting

$$u_z = \lambda^2 \delta z \tag{5.17}$$

where λ is the modified mean motion. It can be shown that, in order to change the period of the out-of-plane motion by a factor k, such that $T_z = kT$, it is necessary to select

$$\lambda = n\sqrt{1 - \left(\frac{1}{k^2}\right)} \tag{5.18}$$

Substituting this into Eq. (5.17) gives

$$u_z = n^2 \delta z \left(1 - \frac{1}{k^2}\right) \tag{5.19}$$

The out-of-plane motion is now given by the augmented equation

$$\delta \ddot{z} = -\frac{n^2 \delta z}{k^2} \tag{5.20}$$

As in Chapter 3, a statically displaced non-Keplerian orbit is achieved when $u_z = n^2 \delta z$ (implying $k \to \infty$). The thrust augmented three-axis motion is exhibited in Fig. 5.7, where the differences between the single- and dual-axis transfers can be clearly seen for $T_z = 5T$. These Figures were generated using Mathematica's NDSolve and ParametricPlot3D functions.

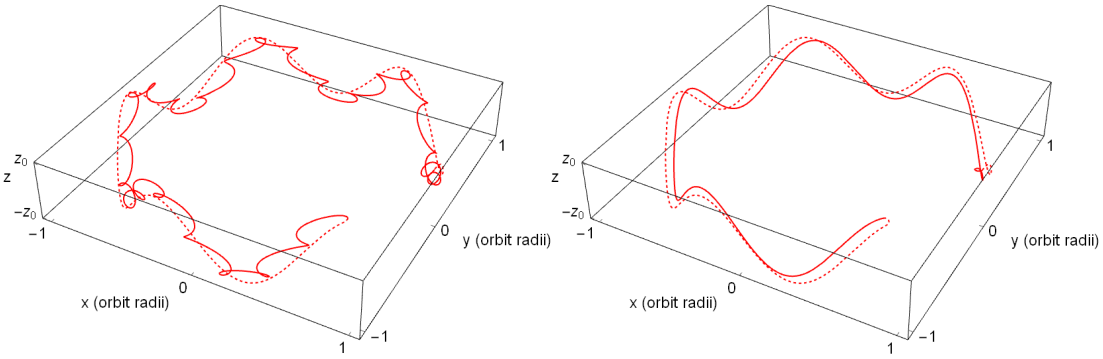

(a) Transfers using single-axis thrust. (b) Transfers using dual-axis thrust.

Figure 5.7: Horseshoe orbits in Earth-centred rotating frame with single-axis thrust transfers and modified-period out-of-plane motion ($T_z = 5T$). Solid line is the inner orbit and dashed line is the outer orbit. The relative orbit has period equal to $50T$, $\delta r_0 = 1000$ km, and $r_0 = 42157$ km in both (a) and (b).

5.5 Discussion

The two methods proposed for providing the orbit transfers necessary to emulate co-orbital motion both offer the possibility of creating constellations of spacecraft on nested relative orbits. The simplest geometrically and arguably most versatile of the two types is the dual-axis thrust version as proposed in Section 5.3. As an example, it would be possible to nest several of these orbits inside each other simply by giving each spacecraft a different initial displacement. Assuming that each spacecraft started on a circular orbit, each would have a different relative velocity, but if the transfer manoeuvres are performed simultaneously the spacecraft relative motion would remain synchronised since the duration of the transfer is constant for all radial displacements. Phased constellations can be achieved simply by varying the along-track displacement of the spacecraft. Additionally, through the addition of out-of-plane thrust which is proportional to displacement, nested horseshoe orbits can be fixed in different planes or with modulated out-of-plane frequency to generate rich new families of spacecraft constellations. It should be noted, however, that the orbit transfers used for this type of orbit require thrust which can be accurately throttled to respond to changing radial

displacement. Concepts for throttled electrostatic and plasma thrusters have existed since the 1980s using pulse-width-modulation (PWM) and other methods [127–130], but at present this is still a technological challenge for electric thrusters, since throttling normally changes the specific impulse (and therefore propellant consumption) of the thruster, and since most possess a lower bound of operating thrust which is greater than zero (e.g. the Qinetiq T5 thruster, which produces a minimum of 5 mN of thrust while operating [33]). It can be expected that the capabilities of this technology will improve with time, in the presence of more mission applications which require such throttling abilities.

It can be envisaged that constellations of small satellites following nested, phased, and displaced-plane orbits could be designed for a wide range of applications including on-orbit inspection and disaggregated spacecraft. As an example which has been suggested throughout this Chapter, reconfigurable constellations using such orbits could be developed to allow, using the example of the geostationary ring, concentrations of spacecraft over certain longitudes at required times, building upon the concepts of McInnes, and Mushet et al. [98, 99].

5.6 Conclusions

It has been shown that certain aspects of co-orbital relative motion in three-body systems can be simply replicated in a linearised two-body system with the addition of continuous low thrust. Using simple thrust commands, two different types of transfer between free-flying orbits have been developed to generate artificial horseshoe orbits: one type which uses single-axis thrust and has a circular outer and elliptical inner orbit, and one type which uses dual-axis thrust and has circular inner and outer orbits. For small Δv, horseshoe orbits of arbitrary length can be generated, and synchronised or phased nested orbits can be achieved since the transfer manoeuvre duration is constant and independent of radial displacement. It has also been shown that thrust augmented out-of-plane motion can be com-

bined with the artificial horseshoe orbits, providing access to rich new families of spacecraft constellations.

Chapter 6

Thrust Augmented Horseshoe Orbits in the Circular Restricted Three-Body Problem

This Chapter addresses Objective 4 as described in Section 1.3, providing analysis of the effects of continuous, conservative thrust-induced acceleration on the generation of horseshoe orbits within a particular three-body system. The Chapter is structured as follows: Section 6.1 describes the equations of motion of the CRTBP augmented with thrust terms, and derives the expressions for the thrust augmented pseudo-potential function and Jacobi integral of the system. Section 6.2 describes the choice of system in which to perform the analyses, Section 6.3 details the method through which the equilibrium points of the system can be located and their stability analysed, and Sections 6.4, 6.5, and 6.6 present the analysis of the effects of thrust on the generation of horseshoe orbits under three different steering laws. Finally, Section 6.7 offers conclusions for the Chapter.

This Chapter primarily aims to extend the work of Dermott and Murray [71, 72], who investigated the dynamics of horseshoe and tadpole orbits in the circular restricted three-body problem, by combining it with that of Dusek [2] who first proposed the generation of artificial libration points through continuous

radial thrust in the CRTBP. It is shown in this Chapter that the existence and stability of horseshoe and tadpole orbits (a schematic of these orbits was shown in Fig. 1.4) are directly linked to the locations of the five equilibrium points, and that continuous radial thrust which modifies the locations of these points also therefore modifies the regions in which such orbits are possible.

An example system is chosen: 243 Ida, a binary asteroid which is assumed here to have mass ratio equal to that of the Sun-Jupiter system. The reasons for this choice are twofold. First, most historical literature investigates the existence of natural tadpole and horseshoe orbits in the Sun-Jupiter system, and so the analysis of these orbits under thrust can be readily compared with existing literature. Second, a binary asteroid system is chosen instead of the Sun-Jupiter system because of the much smaller radial separation between the two primaries. The radial separation governs the orbit period of the system. For a given mass ratio, thrust augmented horseshoe orbits in a system with smaller radial separation are considered more technologically feasible due to the far shorter periods for which a spacecraft would have to remain active and for the associated reduction in Δv.

The analysis performed in this Chapter will later be used to find surface-grazing thrust augmented horseshoe orbits for touch-and-go sampling of binary asteroids in Chapter 7.

6.1 Equations of Motion

A schematic of the thrust augmented CRTBP is shown in Fig. 6.1. The reference frame is again rotating with the line connecting the centres of the two primary masses, forming the x-axis; r_1 and r_2 are the distance of the spacecraft from m_1 and m_2 respectively, and a_1 and a_2 are the magnitudes of constant thrust-induced accelerations directed along the unit radius vector from each primary mass. This steering law is in-keeping with the themes of Chapters 3 and 4. Therefore, fol-

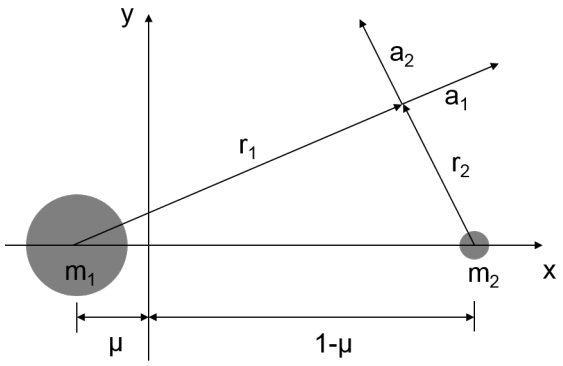

Figure 6.1: Schematic of the thrust augmented circular restricted three-body problem.

lowing Dusek [2], it is assumed that the spacecraft possesses a propulsion system which can produce an acceleration that can be directed along the unit radius vector from either primary. Later, steering laws with $a_1 \neq 0$ and $a_2 = 0$, $a_1 = 0$ and $a_2 \neq 0$, and $a_1 = a_2$ are considered. The simplicity of these steering laws could allow for implementation in relatively low-cost missions with small spacecraft. For example, attitude determination could be provided through the use of cameras and computer vision to obtain the unit vectors from each primary mass.

In agreement with convention, as defined in Section 2.2, $m_1 = 1 - \mu$ and $m_2 = \mu$, with m_1 located at a distance μ from the origin and m_2 located at a distance $1 - \mu$. The angular velocity of the frame, n, is again selected as unity so that the orbital period of the two primary masses is $T = 2\pi$ and the associated gravitational constant is $G = 1$. Considering only the in-plane motion, the equations of motion, augmented with thrust terms, are given by [111]

$$\ddot{x} - 2\dot{y} = x - \frac{\mu(x - 1 + \mu)}{r_2^3} - \frac{(1 - \mu)(\mu + x)}{r_1^3} + a_x \tag{6.1a}$$

$$\ddot{y} + 2\dot{x} = y - \frac{\mu y}{r_2^3} - \frac{(1 - \mu)y}{r_1^3} + a_y \tag{6.1b}$$

where a_x and a_y are thrust-induced accelerations in the x- and y-directions,

respectively. It can be shown geometrically that

$$a_x = \frac{a_1(\mu + x)}{r_1} + \frac{a_2(x - 1 + \mu)}{r_2} \tag{6.2a}$$

$$a_y = \frac{a_1 y}{r_1} + \frac{a_2 y}{r_2} \tag{6.2b}$$

The distances of the spacecraft from m_1 and m_2, respectively, are

$$r_1 = \sqrt{(x + \mu)^2 + y^2} \tag{6.3a}$$

$$r_2 = \sqrt{(x - 1 + \mu)^2 + y^2} \tag{6.3b}$$

and the pseudo-potential of the system, Ω, is given by

$$\Omega = \frac{1}{2}(x^2 + y^2) + \frac{1 - \mu}{r_1} + \frac{\mu}{r_2} + a_1 r_1 + a_2 r_2 \tag{6.4}$$

where the final two terms account for the thrust-induced acceleration. The equations of motion can then be defined in terms of the gradient of the potential such that

$$\ddot{x} - 2\dot{y} = \frac{\partial \Omega}{\partial x} \tag{6.5a}$$

$$\ddot{y} + 2\dot{x} = \frac{\partial \Omega}{\partial y} \tag{6.5b}$$

It can be demonstrated that the system remains conservative, and so it is possible to write a new augmented Jacobi integral of the system as

$$C = 2\Omega - v^2 = (x^2 + y^2) - (\dot{x}^2 + \dot{y}^2) + \frac{2 - 2\mu}{r_1} + \frac{2\mu}{r_2} + 2a_1 r_1 + 2a_2 r_2 \tag{6.6}$$

This new integral, as with the zero-thrust CRTBP, is crucial for determining the boundaries of motion within the system. Setting $v = 0$ in Eq. (6.6) for chosen values of C yields zero-velocity curves for the system. In this respect, the radial

thrust augmented CRTBP can be analysed in the same way as the zero-thrust problem. The zero-velocity curves of the system under zero thrust are the same as those given in Fig. 2.5, showing the locations of the equilibrium points and their associated zero-velocity curves. These contours change when a_1 or a_2 are non-zero.

6.2 Example System: 243 Ida

The formulation of the CRTBP as described in Section 6.1 dictates that the sole parameter necessary to describe the system is the mass ratio of the two primaries, μ. However, it is useful to have a fully dimensional system at hand so that the applications of any results can be quantified.

Much historical literature investigates the existence of tadpole orbits around the L_4 and L_5 points of the Sun-Jupiter system, since the most readily observable and therefore first discovered objects following such orbits were the Jupiter Trojans. It is therefore convenient, when applying the formulation of the CRTBP described in Section 6.1, to use the mass ratio of the Sun-Jupiter system as this readily allows for comparison with analysis in the literature. As such, the mass ratio $\mu = 9.536 \times 10^{-4}$ is used throughout the remainder of this Chapter.

However, the orbit period of the Sun-Jupiter system is approximately 11.86 years. A horseshoe or tadpole orbit in this system could therefore require hundreds of years to complete, and so would be impractical for realistic space missions. However, for a given mass ratio, thrust augmented orbits in systems with a longer orbit period require a smaller dimensional thrust-induced acceleration than those in systems with a shorter orbit period. It can be shown that the dimensional thrust-induced acceleration can be calculated using

$$a_{i_{dim}} = \frac{a_i r_{12_{dim}}}{(\frac{1}{2\pi} T_{dim})^2} \tag{6.7}$$

where the subscript $_{dim}$ denotes the dimensional value of the parameter, r_{12} is the

separation of the two primary masses, T is the orbit period of the system, and $i = 1, 2$. For reference, a constant non-dimensional acceleration of $a_i = \mu$ is equal to the gravitational acceleration produced by m_2 at unit distance. This will be used as the unit of acceleration throughout this Chapter.

A binary asteroid system with an orbit period of the order of one day can now be envisioned, where the two asteroids are assumed to be spherical masses of uniform density. An example is the asteroid 243 Ida and its small satellite, Dactyl. Dactyl was first discovered in images taken by the Galileo spacecraft during its encounter with 243 Ida in August, 1993 [118,119]. Belton et al. described Dactyl's orbit as a function of Ida's mass, yielding an estimate for the density of Ida as $\rho = 2.6 \pm 0.5$ g cm^{-3} [120]. Given the apparent similar composition of Ida and Dactyl, which are both thought to have formed at the breakup of the original Koronis body [121], it is assumed for the purposes of this Chapter that both bodies m_1 and m_2 possess the same density, of 2.6 g cm^{-3}. Using the estimated dimensions of Dactyl [122], the volume of Dactyl is found to be approximately 2.69 km^{-3}. With its density as defined above, Dactyl's mass is estimated as 6.99×10^{12} kg, and the mass ratio of the system is found to be $\mu = 1.66 \times 10^{-4}$. This is of the same order of magnitude as the Sun-Jupiter system, and since the numerical methods used to find periodic horseshoe orbits in Chapter 7 should be verifiable by comparing with orbits found by past authors (e.g. Taylor [74], and Schanzle [75]), the Ida-Dactyl system is herein assumed to have the same mass ratio as the Sun-Jupiter system ($\mu = 9.536 \times 10^{-4}$). Assuming that both bodies are spherical and of uniform density, the radii of m_1 and m_2 are found to be 15.682 km and 1.544 km, respectively. These correspond to non-dimensional radii of $r_{m_1} = 0.1742$ and $r_{m_2} = 0.0172$.

For the purposes of this Chapter, the smaller primary m_2 is also assumed to be in a circular orbit 90 km from the larger primary m_1, consistent with observations [119]. It follows that the distance of m_2 from the origin is 89.914 km, and the distance of m_1 from the centre-of-mass is 0.086 km. It is then possible

	Dimensional	Non-dimensional
m_1	4.2×10^{16} kg	0.9990
m_2	4.01×10^{13} kg	9.536×10^{-4}
r_{m_1}	15.682 km	0.1742
r_{m_2}	1.544 km	0.0172

Table 6.1: Dimensional and corresponding non-dimensional parameters of each primary.

to calculate the orbit period of the binary asteroid system as $T_{dim} \approx 28$ hours.

With a constant non-dimensional acceleration of $a_1 = \mu$, the corresponding dimensional acceleration is found by using Eq. (6.7) to be $a_{1_{dim}} = 3.3 \times 10^{-7}$ m s^{-2}. Thus, a single orbit period of operation in the binary asteroid system would require $\Delta v = 0.033$ m s^{-1}.

The dimensional and corresponding non-dimensional parameters of the two primary masses are summarised in Table 6.1. These values are used throughout this Chapter, although the radii of the primaries are generally only relevant when considering close approaches and rendezvous. Such cases are explored later, in Chapter 7.

6.3 Thrust Augmented Equilibria

Dusek [2] showed that, with constant thrust directed along each of the two unit radius vectors, in general there exist five libration points as in the zero-thrust case. Three of these will be collinear points, and two will be triangular points. In this Chapter, we use the usual labelling convention for these points as defined in Section 2.2.

As with the zero-thrust CRTBP, the locations of the three collinear equilibrium points can be found by setting $\ddot{x} = \dot{y} = y = 0$. The locations of the triangular points, however, are not found in the usual geometric manner, as for $a_i \neq 0$ $(i = 1, 2)$, these two points are not located at the vertex of an equilateral

triangle where the two primary masses form the other two vertices. Regardless, the system retains its symmetry about the x-axis, and the triangular points can still be located by finding the equilibrium points with highest pseudo-potential. Although there usually exist five libration points, two special cases do exist in which the two triangular points are no longer distinct from either the first or third collinear point (i.e. $y_{L_4} = y_{L_5} = 0$), and so either L_1 or L_3 is the point of highest potential in the system in each of these cases.

It is well known that, in the zero-thrust CRTBP, motion close to the three collinear equilibrium points is unstable and motion close to the two triangular points is stable in the sense of Lyapunov for $\mu < 0.0385$, as discussed in Section 2.2.1. In the thrust augmented CRTBP considered here, it should not be assumed that the modified equilibrium points retain the same stability properties as their zero-thrust counterparts. As such, it is useful to consider the stability analysis of the modified equilibria.

First, it is assumed that the spacecraft is positioned close to the equilibrium point in question, so that

$$x = x_e + \delta x \tag{6.8a}$$

$$y = y_e + \delta y \tag{6.8b}$$

$$\dot{x} = \delta\dot{x} \tag{6.8c}$$

$$\dot{y} = \delta\dot{y} \tag{6.8d}$$

where δx and δy are small displacements, and (x_e, y_e) are the coordinates of the equilibrium point. The equations of motion of the system can be written, to linear order, as

$$\delta\ddot{x} - 2\delta\dot{y} = \frac{\partial\Omega}{\partial x}\Big|_{(x_e,y_e)} + \frac{\partial^2\Omega}{\partial x^2}\Big|_{(x_e,y_e)}\delta x + \frac{\partial^2\Omega}{\partial x\partial y}\Big|_{(x_e,y_e)}\delta y \tag{6.9a}$$

$$\delta\ddot{y} + 2\delta\dot{x} = \frac{\partial\Omega}{\partial y}\Big|_{(x_e,y_e)} + \frac{\partial^2\Omega}{\partial y^2}\Big|_{(x_e,y_e)}\delta y + \frac{\partial^2\Omega}{\partial x\partial y}\Big|_{(x_e,y_e)}\delta x \tag{6.9b}$$

Recalling Eq. (6.4), we find that

$$\frac{\partial^2\Omega}{\partial x^2} = 1+\frac{a_2y^2}{r_2^3}-\frac{(\mu-1)(2\mu^2+4\mu x+2x^2-y^2)}{r_1^5}+\frac{a_1y^2}{r_1^3}+\mu\left(\frac{3(x-1+\mu)^2}{r_2^5}-\frac{1}{r_2^3}\right) \tag{6.10a}$$

$$\frac{\partial^2\Omega}{\partial y^2} = 1+\frac{a_2(x-1+\mu)^2}{r_2^3}+\frac{(\mu-1)(\mu^2+2\mu x+x^2-2y^2)}{r_1^5}+\frac{a_1(\mu+x)^2}{r_1^3} + \mu\left(\frac{3y^2}{r_2^5}-\frac{1}{r_2^3}\right) \tag{6.10b}$$

$$\frac{\partial^2\Omega}{\partial x\partial y} = y\left(\frac{3\mu(x-1+mu)}{r_2^5}-\frac{a_2(x-1+\mu)}{r_2^3}-\frac{3(\mu-1)(\mu+x)}{r_1^5}-\frac{a_1(\mu+x)}{r_1^3}\right) \tag{6.10c}$$

From Eq. (6.9) the linear dynamics in the neighbourhood of an equilibrium point can be described in matrix form as

$$\delta\dot{\boldsymbol{x}} = \begin{bmatrix}\dot{\delta x}\\ \dot{\delta y}\\ \delta\ddot{x}\\ \delta\ddot{y}\end{bmatrix} = \begin{bmatrix}0 & 0 & 1 & 0\\ 0 & 0 & 0 & 1\\ \frac{d^2\Omega}{dx^2} & \frac{d^2\Omega}{dxdy} & 0 & 2\\ \frac{d^2\Omega}{dxdy} & \frac{d^2\Omega}{dy^2} & -2 & 0\end{bmatrix}\begin{bmatrix}\delta x\\ \delta y\\ \delta\dot{x}\\ \delta\dot{y}\end{bmatrix} = \boldsymbol{A}\delta\boldsymbol{x} \tag{6.11}$$

As is well established, the solutions to the above system will be of the form

$$\delta\boldsymbol{x} = \sum_{j=1}^{4}\boldsymbol{\eta}_j e^{\lambda_j t} \tag{6.12}$$

where $\boldsymbol{\eta}$ represents the eigenvectors and λ represents the eigenvalues of the system. The characteristic polynomial $p(\lambda)$ of the matrix $\boldsymbol{A}$ is found from

$$p(\lambda) = \det(\boldsymbol{A} - \lambda \boldsymbol{I}) = \begin{vmatrix} -\lambda & 0 & 1 & 0 \\ 0 & -\lambda & 0 & 1 \\ \frac{d^2\Omega}{dx^2} & \frac{d^2\Omega}{dxdy} & -\lambda & 2 \\ \frac{d^2\Omega}{dxdy} & \frac{d^2\Omega}{dy^2} & -2 & -\lambda \end{vmatrix} \tag{6.13}$$

The eigenvalues are then the roots of $p(\lambda)$. Again, if any of the four eigenvalues has a positive real part, then the particular equilibrium point is unstable. Furthermore, since the trace $\mathrm{Tr}(\boldsymbol{A}) = 0$, the system possesses opposite and conjugate pairs of eigenvalues which must sum to zero.

6.3.1 Critical Horseshoe Curve

The locations and nature of the equilibrium points are key to establishing the region in which horseshoe orbits can occur. As a definition, first given by Brown [65], the zero-velocity curve which touches L_3 (and therefore possesses the same Jacobi constant as L_3) will, under normal zero-thrust conditions, form a horseshoe shape consisting of two lobes connected at L_3, each lobe surrounding L_4 or L_5. Orbits within or around a single one of these two lobes are *tadpole* orbits, and they encompass either L_4 or L_5, but not both. This zero-velocity curve is termed the *critical tadpole curve*. Orbits which instead encompass all of the three points L_3, L_4, and L_5, and therefore exist outside of the critical tadpole curve, are termed *horseshoe* orbits. From the definition in the literature [65, 71], the *critical horseshoe curve* passes through L_1 and L_2. Horseshoe orbits should exist, therefore, between the critical tadpole curve and the critical horseshoe curve. It should be noted here that, although past authors considered the critical horseshoe curve to pass through L_1 and L_2, generally these two points possess slightly different Jacobi constants, and therefore have different associated zero-velocity curves. Herein, the literature definition shall be used when applicable, but to avoid confusion both the L_1 and L_2 curves shall be displayed when plotting the critical curves. Indeed, it will be seen that the literature definition of the critical horse-

shoe curve breaks down somewhat when thrust is applied, since the zero-velocity curves of L_1 and L_2 separate considerably under certain thrust conditions.

The critical tadpole and horseshoe curves for a system with $\mu = 9.536 \times 10^{-4}$ are shown in Fig. 6.2, with example tadpole and horseshoe orbits. These Figures were generated using Mathematica's NDSolve and ParametricPlot3D functions. It can be seen that the tadpole orbit (Fig. 6.2a) passes outside of the critical tadpole curve. This is possible because, unlike horseshoe orbits, the tadpole orbit family cannot be bounded by a particular value of Jacobi constant. The critical tadpole curve represents a lower level of potential than that of the tadpole orbit shown, and so the orbit may cross the boundary. Conceptually, the critical tadpole curve can more accurately be considered the limiting curve beyond which, at higher levels of potential, horseshoe motion is no longer possible. For the same system, a natural horseshoe orbit is shown overlaying the critical curves in Fig. 6.2b. This orbit is given initial conditions such that its Jacobi integral is close to that of the critical tadpole curve, and so the orbit also remains close to the critical curve.

6.4 Steering Law 1: $a_1 \neq 0$, $a_2 = 0$

Now that the critical curves have been defined and it has been shown that they are governed by the locations and nature of the three collinear equilibrium points, the effect of thrust on these points and the horseshoe orbit region can be analysed. Three particular situations are to be considered: when $a_1 \neq 0$, $a_2 = 0$, when $a_1 = 0$, $a_2 \neq 0$, and when $a_1 = a_2$. This Section considers the case where the thrust-induced acceleration is directed only along the radius vector from the larger primary, i.e. $a_1 \neq 0$, $a_2 = 0$. Again, the thrust-induced acceleration is constant. From the convention defined in Fig. 6.1, this acceleration is positive if directed away from the primary, and negative if directed towards the primary.

The vector field of the acceleration for this case is shown in Fig. 6.3a (gen-

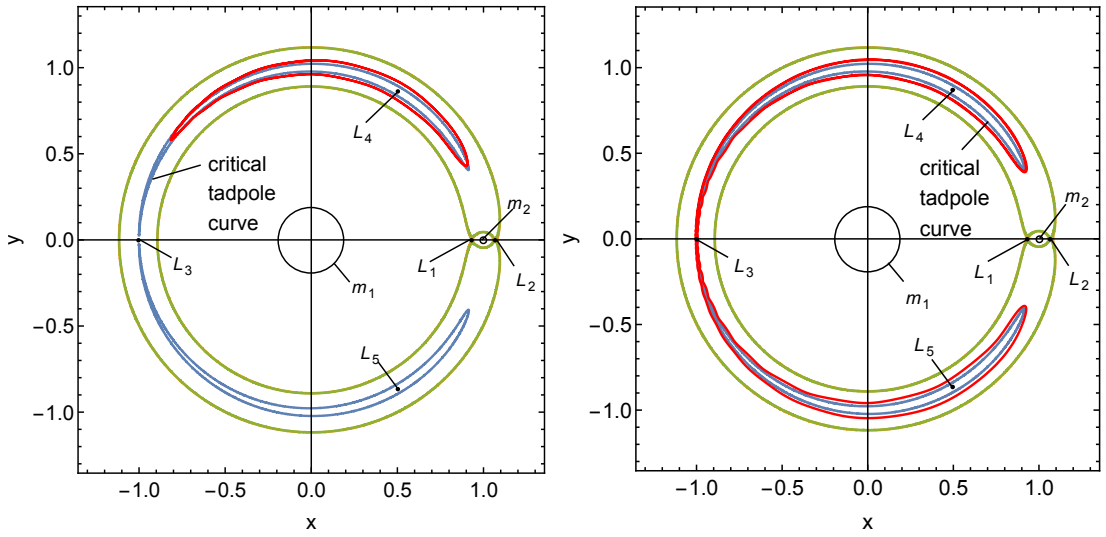

(a) Tadpole orbit.

(b) Horseshoe orbit.

Figure 6.2: Tadpole and horseshoe orbits when $a_1 = a_2 = 0$. The L_3, L_1, and L_2 zero-velocity curves are represented by the blue, orange, and green curves respectively, and the red curve is the trajectory of the spacecraft. Note that the orange and green curves are so close as to be almost indistinguishable.

erated using Mathematica's VectorPlot function). Figure 6.3b shows the evolution of the locations of the three collinear equilibrium points for the range $1000\mu \geq a_1 \geq -1000\mu$ and $a_2 = 0$ where the non-dimensional acceleration is defined in units of μ, as discussed in Section 6.2. The locations of the equilibria were found using Mathematica's NSolve function, and the positions plotted using ListPlot. It can be noted that, for positive a_1, L_1 and L_3 draw markedly closer to the origin, and while L_2 also moves slightly closer the origin, it remains much closer to its original location than the other two points. Conversely, for negative a_1, the points L_2 and L_3 move quickly away from the origin, and L_1 remains relatively close to its zero-thrust location. Accordingly, the critical curves also change location and shape for each value of a_1. Furthermore, the location of L_4 under a range of accelerations is given in Fig. 6.3c, with the location of L_5 being symmetric about the x-axis.

The evolution of the critical tadpole curve for a range of a_1 is shown in Fig. 6.4, generated using Mathematica's ContourPlot function (all subsequent plots of

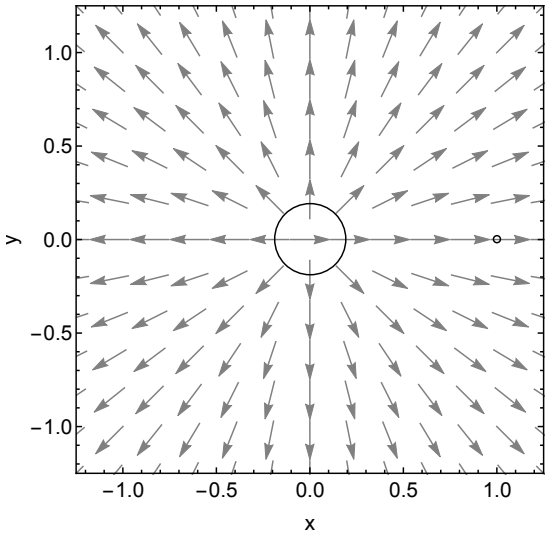

(a) Thrust-induced acceleration vector field.

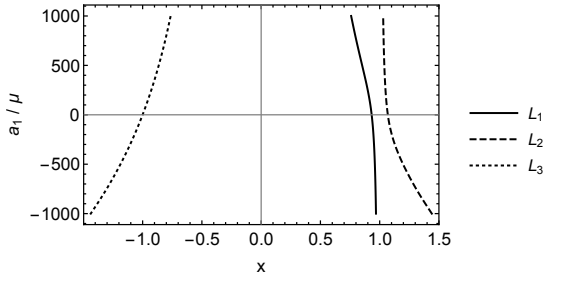

(b) Collinear equilibrium points.

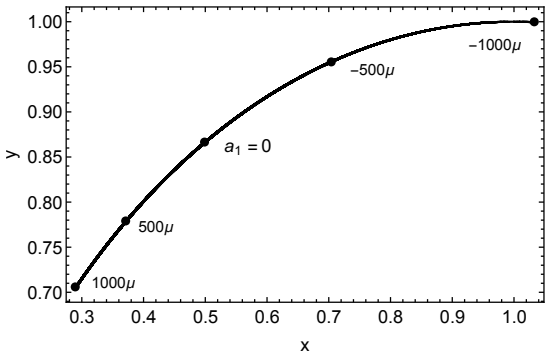

(c) L_4.

Figure 6.3: Thrust-induced acceleration vector field (a) and locations of the equilibrium points (b, c) for Steering Law 1, with $-1000\mu \leq a_1 \leq 1000\mu$.

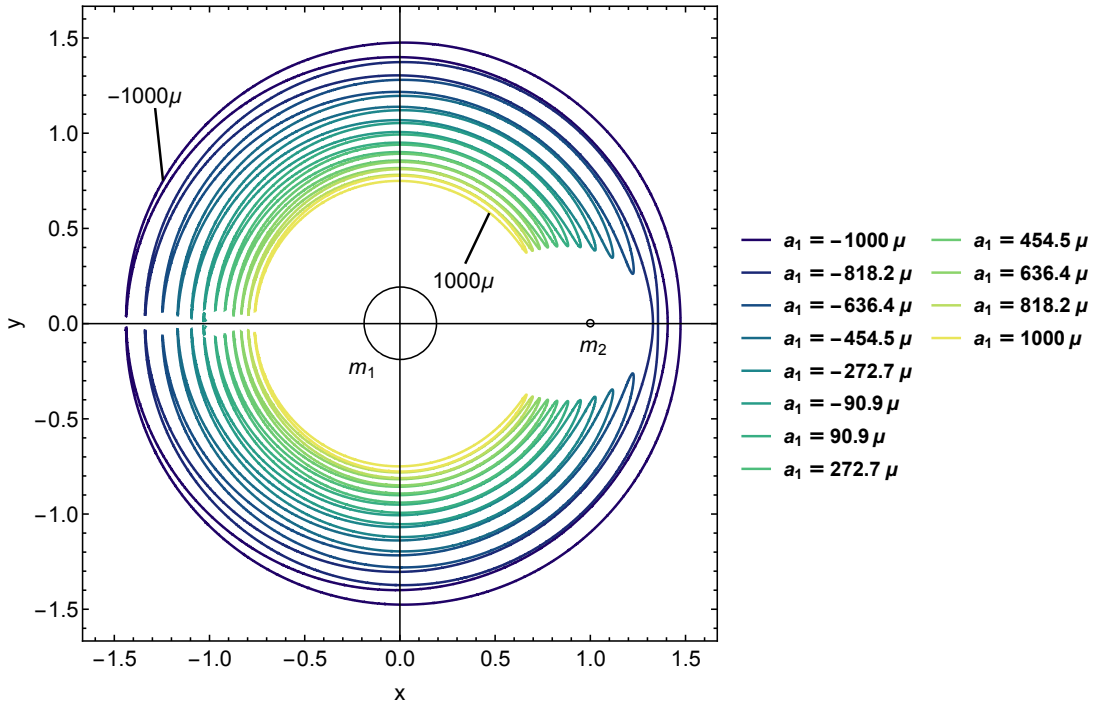

Figure 6.4: Critical tadpole (L_3) curves for $1000\mu \geq a_1 \geq -1000\mu$ and $a_2 = 0$.

zero-velocity curves are also generated in this way). It can be seen that a merge between the two tadpole lobes occurs at a point within the range $-818.2\mu < a_1 < -636.4\mu$. The evolution of the L_1 and L_2 curves is shown in Fig. 6.5 and Fig. 6.6. As expected from inspection of Fig. 6.3b, the two curves which classically mark the critical horseshoe curve become widely separated under this steering law.

In the CRTBP without thrust, tadpole orbits are known to be the stable librations of particles around L_4 and L_5 [71], so it can be supposed that horseshoe orbits, which also librate around L_4 and L_5, also depend on the stability properties of the dynamics at these points. This suggests that horseshoe orbits are unlikely to occur in systems with unstable dynamics at these points, and so helps to limit the range of thrust-induced acceleration which is considered when searching for orbits.

Two extreme cases of this steering law are illustrated in Fig. 6.7 and Fig. 6.8, for $a_1 = 1000\mu$ and $a_1 = -1000\mu$, respectively. In Fig. 6.7, it can be seen

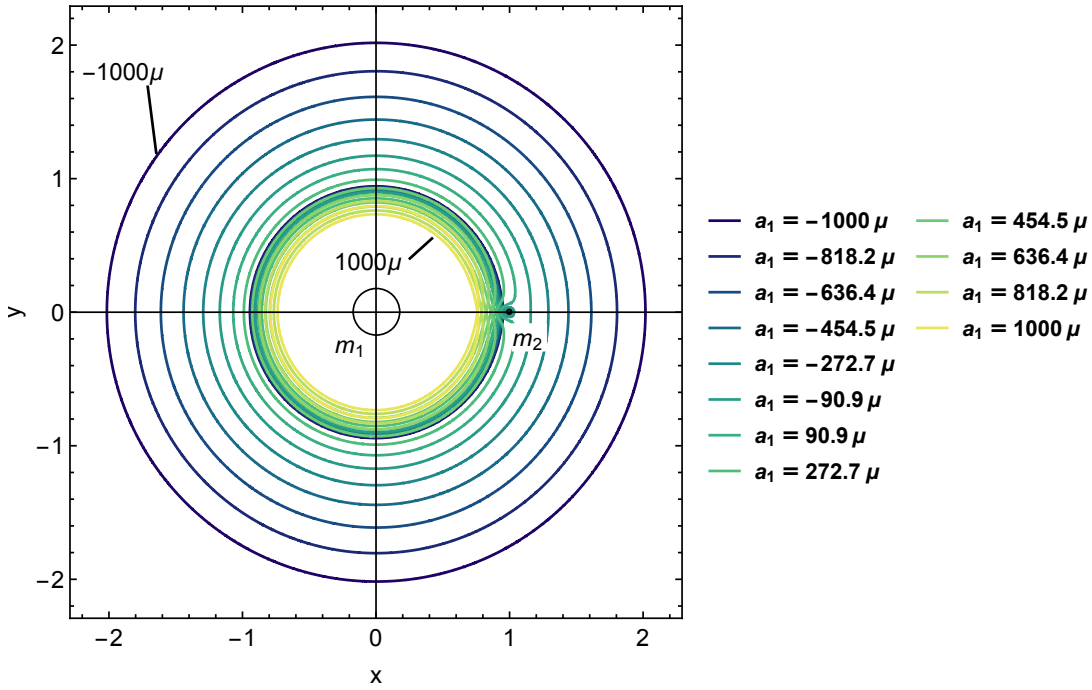

(a) System overview.

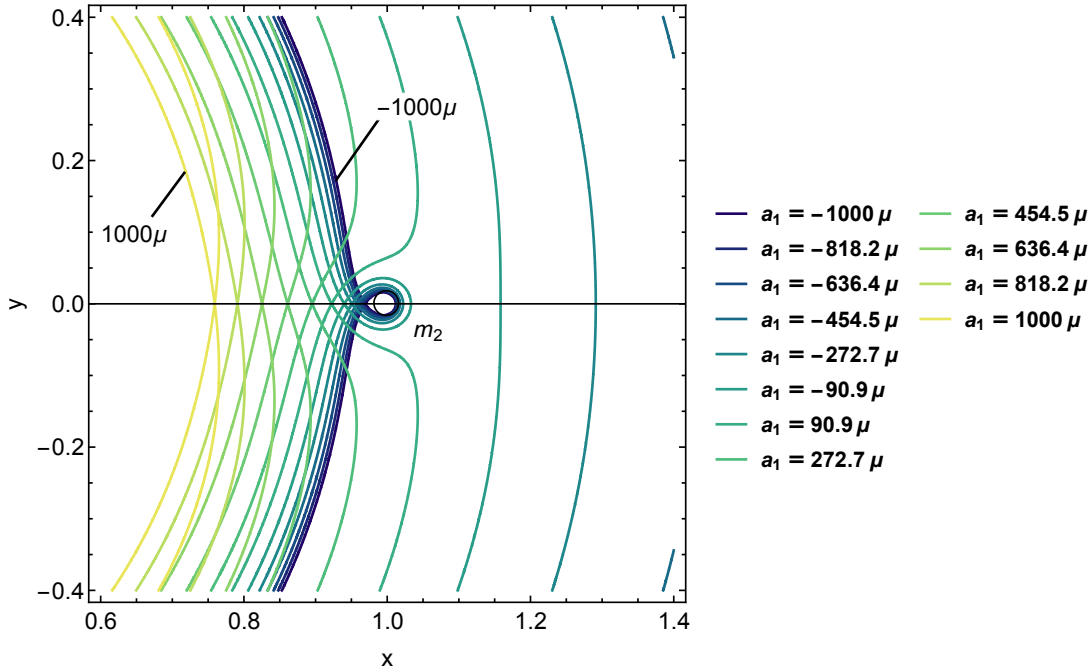

(b) Detail around m_2.

Figure 6.5: Curves of zero velocity for L_1, when $1000\mu \geq a_1 \geq -1000\mu$ and $a_2 = 0$.

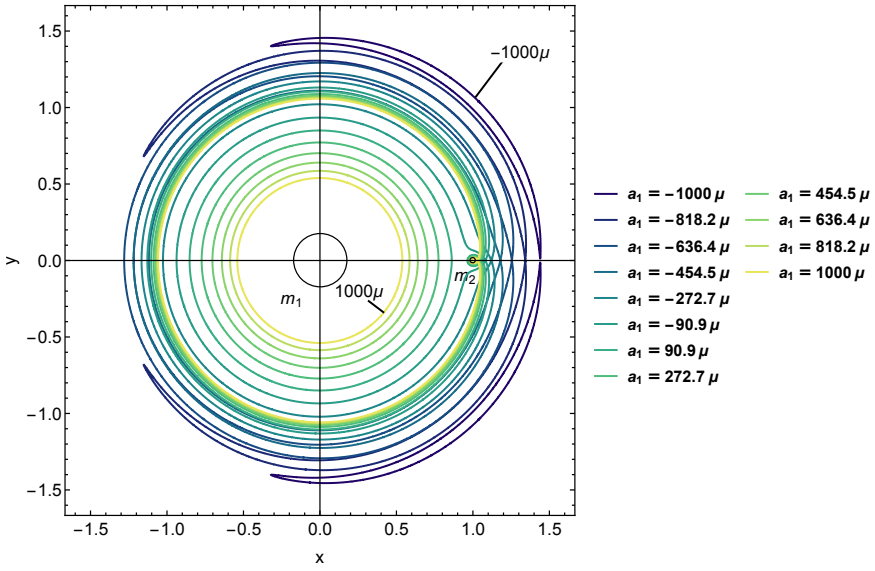

(a) System overview.

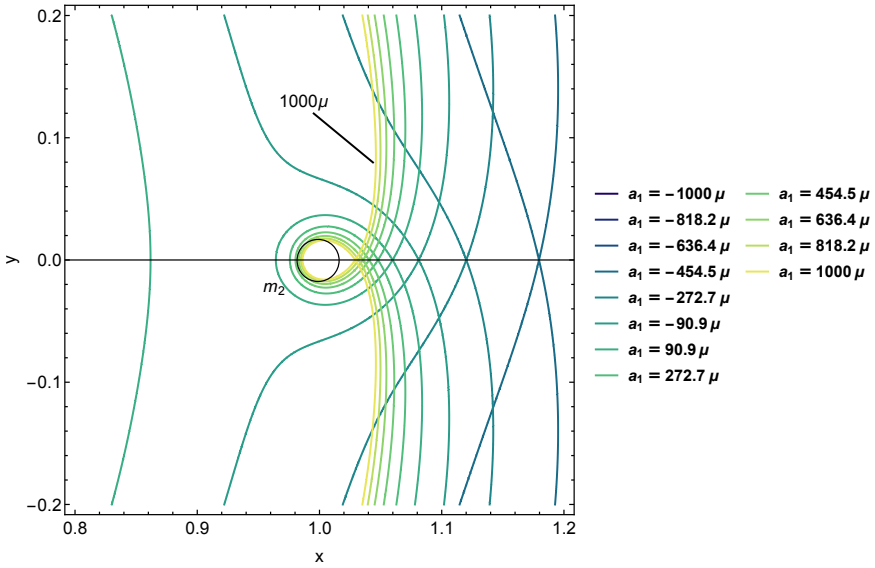

(b) Detail around m_2.

Figure 6.6: Curves of zero velocity for L_2, when $1000\mu \geq a_1 \geq -1000\mu$ and $a_2 = 0$.

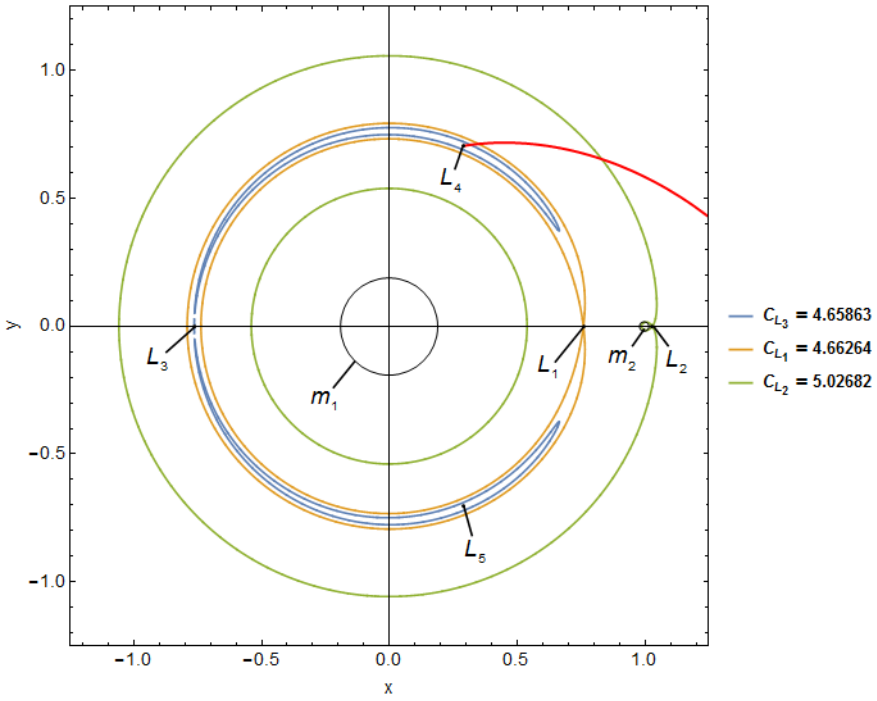

Figure 6.7: Critical curves for $a_1 = 1000\mu$ and $a_2 = 0$. Note that the curves of zero velocity for L_1 (orange) and L_2 (green) have separated considerably. The L_3 curve (blue) is of similar shape to the zero-thrust case, however as L_3 has moved closer to the origin, the curve has also contracted in radius. The red curve is the trajectory of a spacecraft placed with zero velocity close to L_4, clearly showing that motion near the triangular points is no longer stable.

a_1	λ_1	λ_2	λ_3	λ_4
1000μ	-1.22085	1.22085	0.0949449	-0.0949449
500μ	$0.27369 + 0.150981i$	$0.27369 - 0.150981i$	$-0.27369 + 0.150981i$	$-0.27369 - 0.150981i$
0	$0.996758i$	$-0.996758i$	$0.080452i$	$-0.080452i$
-500μ	$1.34206i$	$-1.34206i$	$0.0475089i$	$-0.0475089i$
-1000μ	$1.52487i$	$-1.52487i$	$0.0315107i$	$-0.0315107i$

Table 6.2: Eigenvalues of the system linearised about the artificial L_4 point, using Steering Law 1.

that the two-lobed form of the critical tadpole curve is preserved, though it has shrunk in accordance with the location of L_3. The tadpole curve still encloses the two points of maximum potential, L_4 and L_5, but the L_1 and L_2 curves have become widely separated. It can be seen that a spacecraft placed close to L_4 in this system does not remain close to the equilibrium point, indicating that the triangular points have become unstable. This lack of stability is confirmed by examining the eigenvalues of the linearised system at the equilibrium point, using the method detailed in Section 6.3. The eigenvalues of the system at the artificial triangular equilibrium point for a range of a_1 are given in Table 6.2. It can be seen that, when $a_1 = 1000\mu$, two of the eigenvalues are positive real, and so the dynamics close to the triangular points L_4 and L_5 are unstable in this case.

However, in Fig. 6.8, it can be seen that the two lobes of the L_3 curve of zero velocity have become connected and now form a single continuous crescent. Furthermore, the L_2 curve is now of higher potential than L_3, and it now surrounds L_4 and L_5. Tadpole orbits can still occur in this system, around either L_4 or L_5, and though horseshoe motion in the classical sense is no longer possible, crescent-shaped orbits which enclose L_4, L_2, and L_5 can occur. It can be seen from Table 6.2 that for this case the eigenvalues of the system at L_4 are all imaginary, like the zero-thrust case, indicating stability in the sense of Lyapunov.

The magnitudes of the real and imaginary parts of one eigenvalue from each conjugate pair at the L_4 point are given in Fig. 6.9 for the range $-1000\mu \leq a_1 \leq 1000\mu$. Only one from each pair is required because, in every case where the real part is non-zero, there exists at least one eigenvalue with a positive real part.

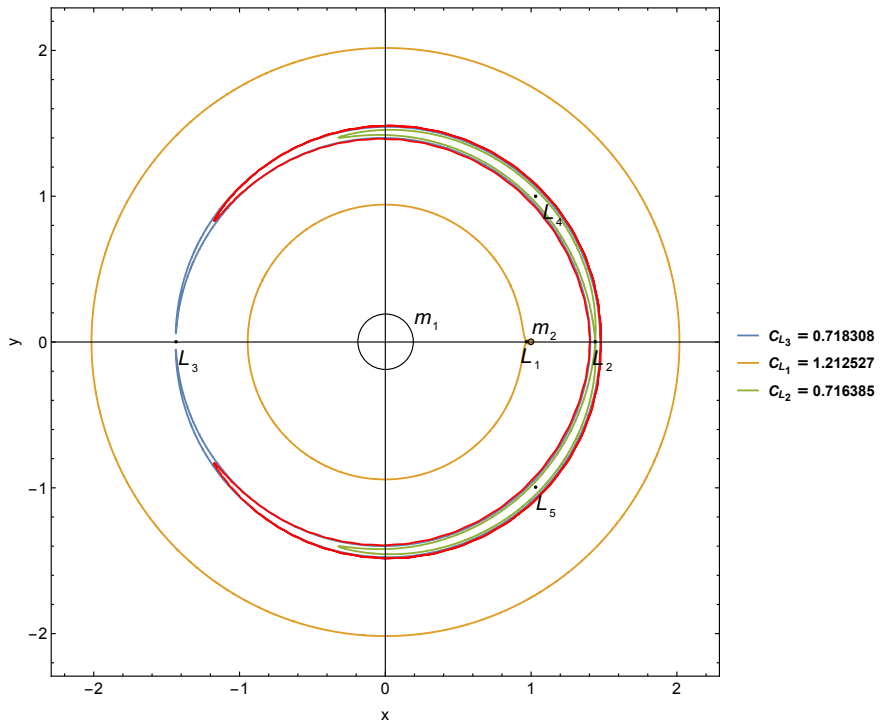

Figure 6.8: Critical curves for $a_1 = -1000\mu$ and $a_2 = 0$. The curves of zero velocity for L_1 (orange) and L_2 (green) are widely separated. The two lobes of the L_3 curve (blue) have connected and now form a single continuous crescent, and the radius of this has expanded in conjunction with the location of L_3. The red curve is a crescent-shaped orbit with greater potential than L_3. Initial conditions are $x_0 = -1.16498$, $y_0 = 0.846411$, and $\dot{x}_0 = \dot{y}_0 = 0$.

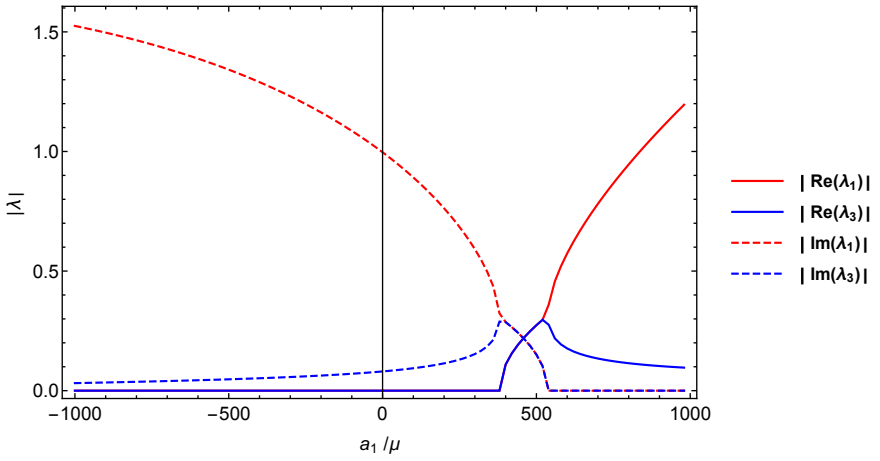

Figure 6.9: Magnitudes of the real and imaginary parts of one of each conjugate pair of eigenvalues for the thrust modified L_4, and Steering Law 1.

a_1	x_{L_3}	x_{L_2}	C_{L_3}	C_{L_2}
-800μ	-1.32927	1.33293	1.24532	1.24518
-798.182μ	-1.32834	1.33202	1.24992	1.2498
-796.364μ	-1.32740	1.33110	1.25452	1.25442
-794.545μ	-1.32647	1.33019	1.25912	1.25904
-792.727μ	-1.32554	1.32928	1.26371	1.26366
-790.909μ	-1.32460	1.32837	1.26831	1.26827
-789.091μ	-1.32367	1.32746	1.27289	1.27288
-787.273μ	-1.32274	1.32655	1.27748	1.27748
-785.455μ	-1.32181	1.32564	1.28206	1.28208
-783.636μ	-1.32089	1.32473	1.28664	1.28668
-781.818μ	-1.31996	1.32382	1.29121	1.29128
-780μ	-1.31903	1.32292	1.29579	1.29587

Table 6.3: Locations and Jacobi constants of L_2 and L_3 for $-800\mu \leq a_1 \leq -780\mu$.

As such, the system possesses no asymptotic stability. It can be shown that the dynamics at L_4 and L_5 become unstable for approximately $a_1 > 380.2\mu$.

Further, it is useful to find the acceleration at which the L_2 and L_3 curves of zero velocity are equal: that is, the value of a_1 which causes both L_2 and L_3 to have the same potential. This acceleration value will be defined as a_{merge}. With $a_1 = a_{merge}$, the two lobes of the L_3 zero-velocity curve touch at L_2. For $a_1 < a_{merge}$, the lobes merge together to form the continuous crescent seen in Fig. 6.8. By setting $\dot{x} = \dot{y} = y = 0$ and solving Eq. (6.1a) to find the locations of L_2 and L_3 for a range of a_1, then substituting these locations for x in Eq. (6.6) to find the Jacobi constant at each point as listed in Table 6.3, it is found by interpolation that $a_{merge} = -787.3\mu$.

6.4.1 Summary of Horseshoe and Tadpole Motion with Steering Law 1

It is now possible to summarise the ranges of thrust-induced acceleration for which horseshoe and tadpole orbits can occur under Steering Law 1, in the binary asteroid system ($\mu = 9.536 \times 10^{-4}$):

- For $a_1 > 380.2\mu$, the dynamics at L_4 and L_5 become unstable. Under these conditions, it is seen that horseshoe and tadpole orbits do not freely occur, as a spacecraft injected close to the triangular points, or close to the L_3 zero-velocity curve, does not remain close to it.

- For $-787.3\mu < a_1 < 380.2\mu$, the dynamics at L_4 and L_5 are stable, and both tadpole and horseshoe orbits can occur.

- For $a_1 < -787.3\mu$, the dynamics at L_4 and L_5 are stable, so tadpole orbits can still occur around these points. However, horseshoe orbits can no longer occur because the two lobes of the L_3 zero-velocity curve have become connected. Crescent-shaped orbits, which encircle L_2, L_4, and L_5, can occur.

6.5 Steering Law 2: $a_1 = 0$, $a_2 \neq 0$

This Section considers the case when the thrust-induced acceleration is directed only along the radius vector from the smaller primary, r_2. Thus, $a_1 = 0$, $a_2 \neq 0$, where a_2 is constant. The thrust-induced acceleration vector field for this steering law is shown in Fig. 6.10a.

The evolution of the locations of the three collinear equilibrium points under this steering law for $1000\mu \geq a_2 \geq -1000\mu$ is given in Fig. 6.10b. It can be seen that, for positive a_2, L_1 and L_2 draw closer to each other (and closer to m_2), and that L_3 also draws inwards towards the origin. Conversely, for negative a_2, L_1 and L_2 separate from each other and from m_2, and L_3 expands away from the origin. It appears that the region in which horseshoe orbits can occur should expand with increasingly negative a_2. The evolution of the location of L_4 under this steering law is given in Fig. 6.10c, where the collapse of L_4 (and, due to the symmetry of the system about the x-axis, L_5) into L_3 can be seen to occur at approximately $a_2 = -2\mu$. For $a_2 < -2\mu$, it can be seen that the y-axis location

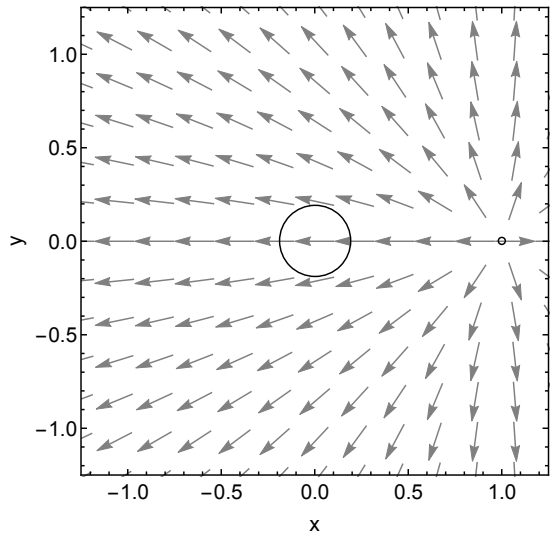

(a) Thrust-induced acceleration vector field.

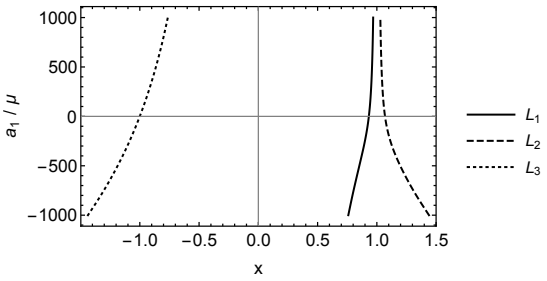

(b) Collinear equilibrium points.

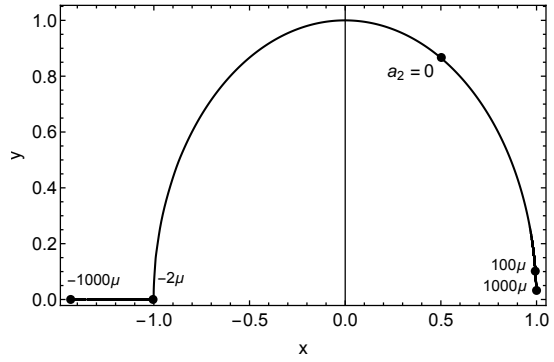

(c) L_4.

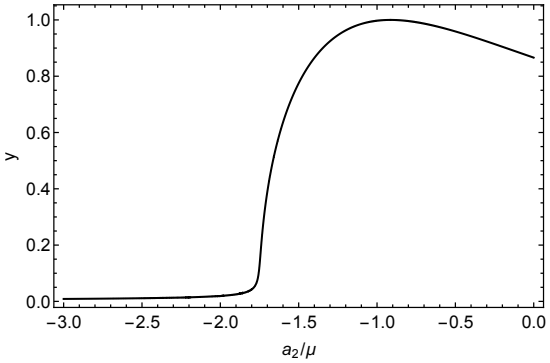

(d) y-coordinate of L_4 at merge with L_3.

Figure 6.10: Thrust-induced acceleration vector field (a) and locations of the equilibrium points (b, c) for Steering Law 2, with $-1000\mu \leq a_2 \leq 1000\mu$. The asymptotic approach of the y-coordinate to zero can be seen in (d).

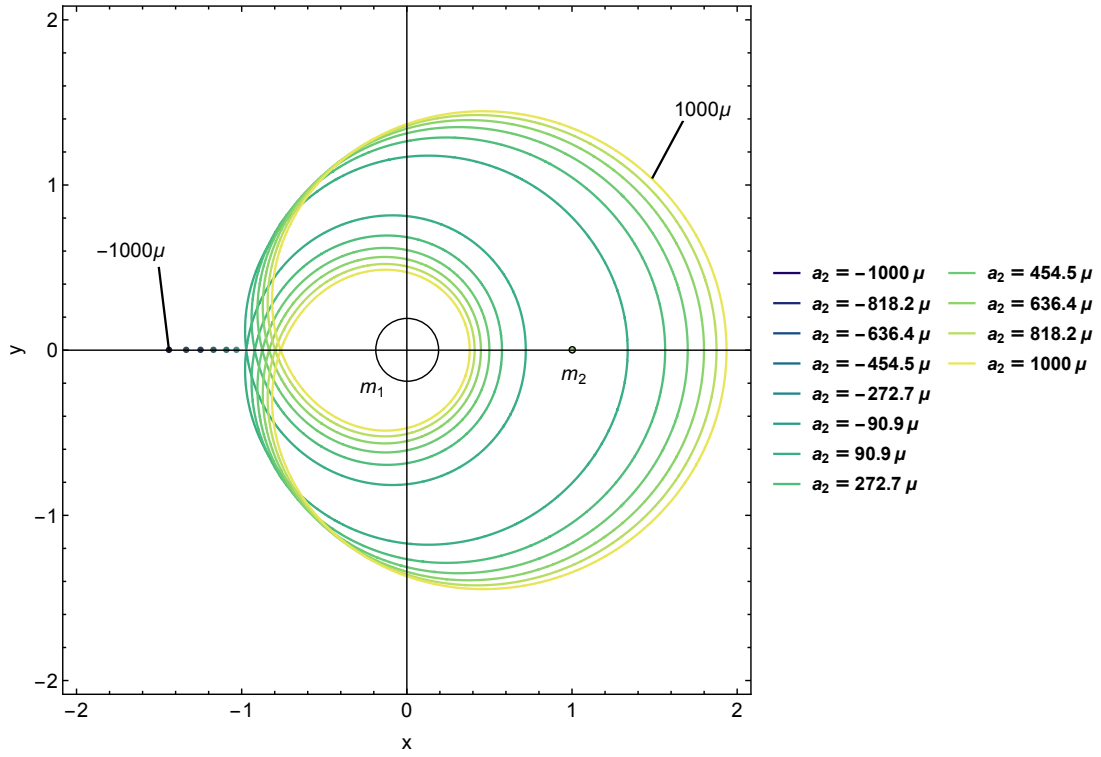

Figure 6.11: Critical tadpole (L_3) curves for Steering Law 2.

of L_4 asymptotically approaches zero.

The evolution of the critical tadpole curve over a range of a_2 is shown in Fig. 6.11. Note that for the values $a_2 \leq -90.9\mu$ the zero-velocity curves are shown only as individual points, since the L_3 curve actually collapses into the L_3 point, indicating furthermore that L_3 has become the point of maximum potential for the system. This collapse of the L_3 curve, which signals the collapse of the triangular libration points into L_3, occurs in the interval $-90.9\mu \leq a_2 \leq 90.9\mu$. A plot of the evolution of the L_3 zero-velocity curve over a smaller range of a_2 ($-10\mu \leq a_2 \leq 10\mu$) is shown in Fig. 6.12a, with a detailed plot showing the L_3 points in Fig. 6.12b.

The evolution of the L_1 zero-velocity curve for a range of a_2 is shown in Fig. 6.13a, with a detailed plot of the region close to m_2 shown in Fig. 6.13b.

As in Section 6.4, the stability of the triangular point L_4 can be evaluated through examination of the eigenvalues of the system linearised at the equilibrium

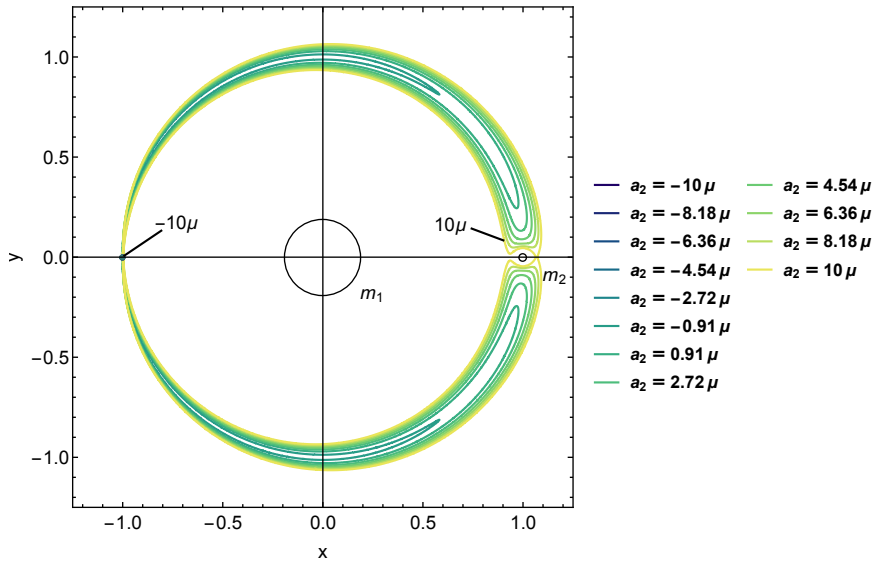

(a) System overview.

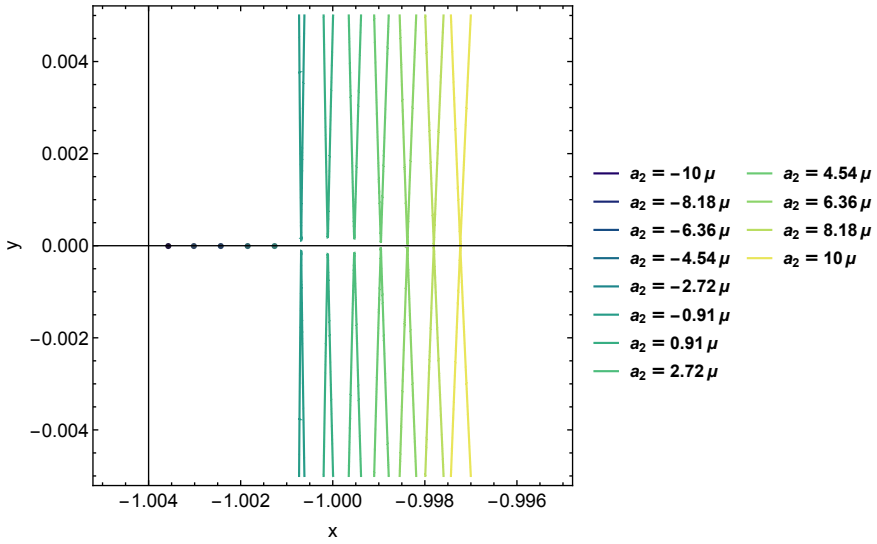

(b) Detail showing evolution of L_3.

Figure 6.12: Curves of zero velocity for L_3, when $a_1 = 0$ and $10\mu \geq a_2 \geq -10\mu$.

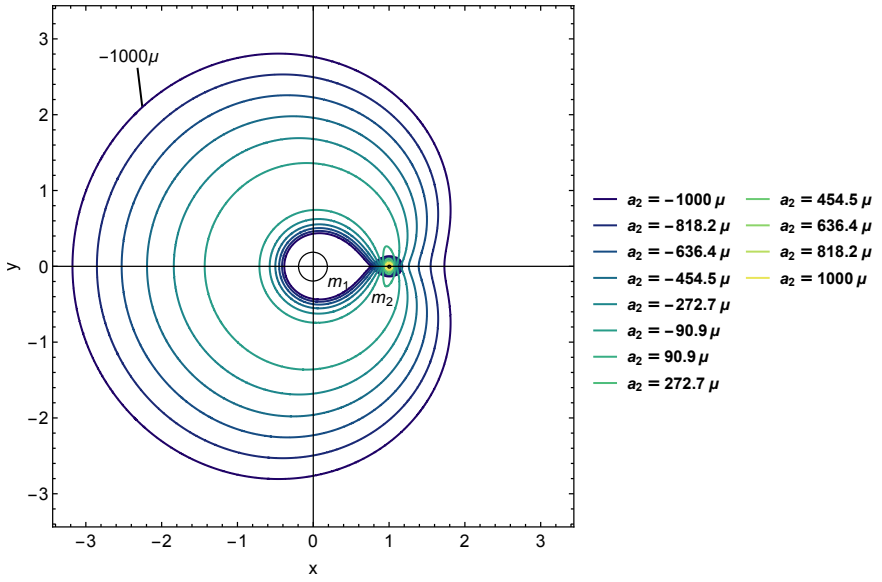

(a) System overview.

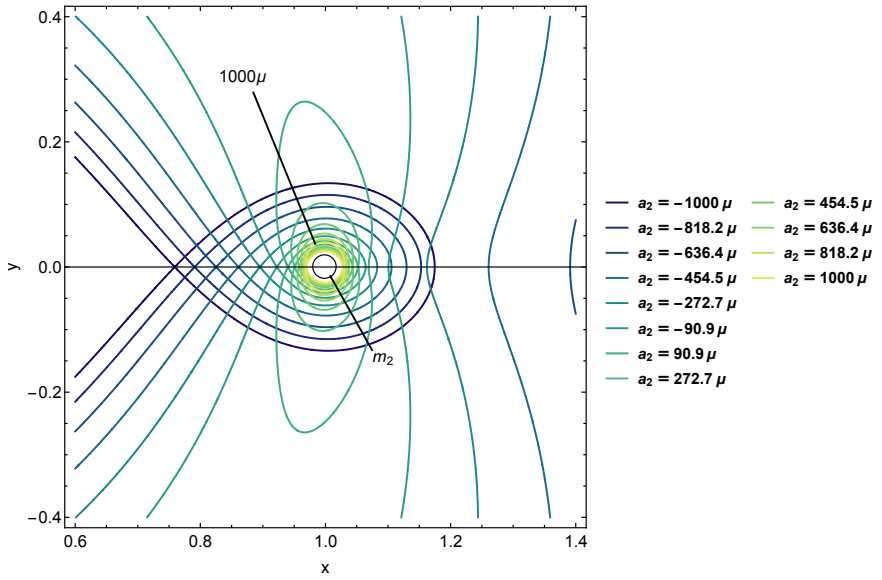

(b) Detail around m_2.

Figure 6.13: Curves of zero-velocity for L_1 when $a_1 = 0$ and $1000\mu \geq a_2 \geq -1000\mu$.

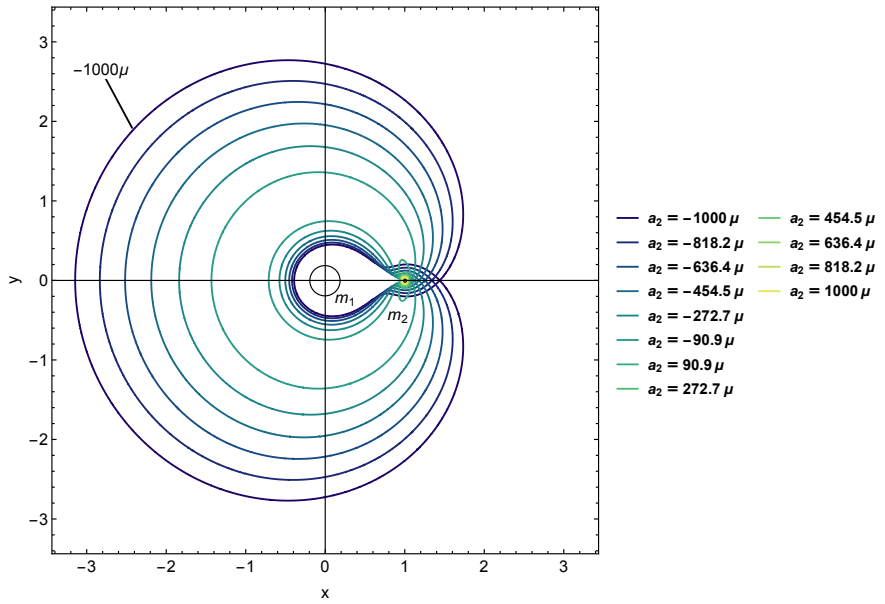

(a) System overview.

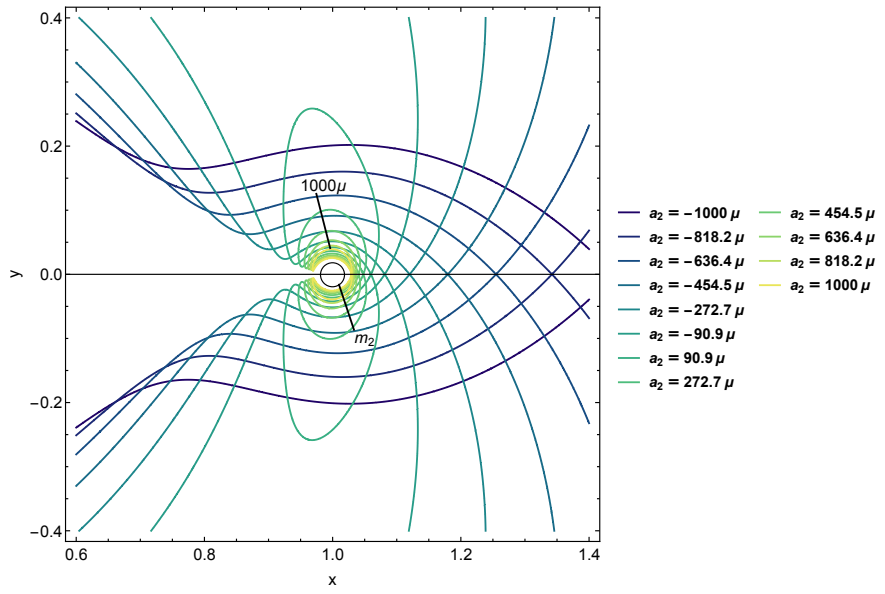

(b) Detail around m_2.

Figure 6.14: Curves of zero-velocity for L_2 when $a_1 = 0$ and $1000\mu \geq a_2 \geq -1000\mu$.

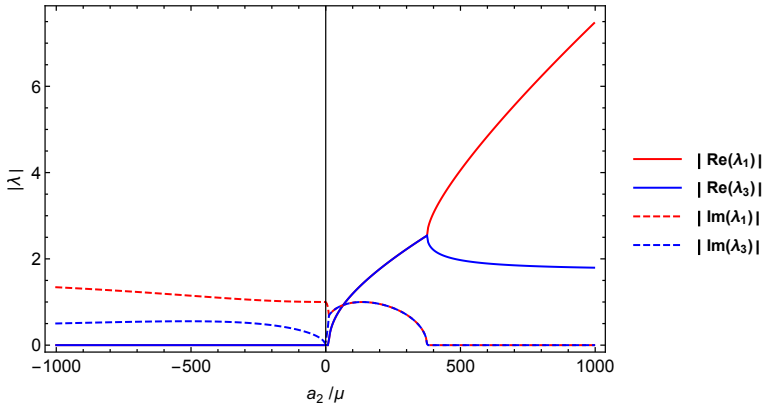

(a) Eigenvalues over a range of a_2.

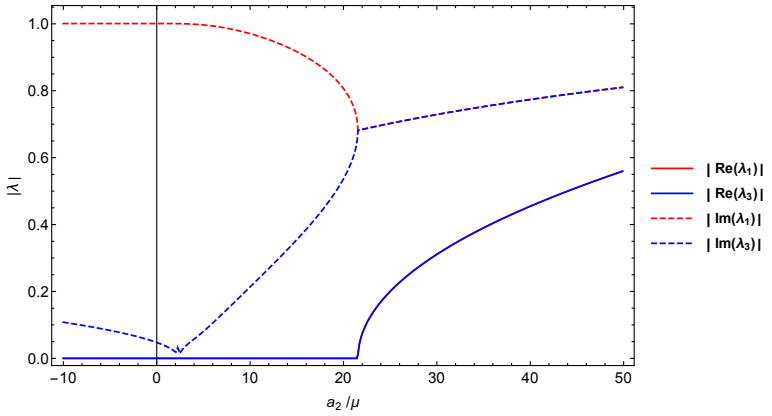

(b) Detailed plot around $a_2 = 20\mu$.

Figure 6.15: Magnitudes of the real and imaginary parts of one of each conjugate pair of eigenvalues for the thrust modified L_4 for Steering Law 2.

point in question. Using the method outlined in Section 6.1 (Eq. (6.13)), the real and imaginary parts of one eigenvalue from each conjugate pair are plotted against a_2 in Fig. 6.15a. In general, it can be seen that the dynamics close to L_4 are stable for $a_2 \leq 0$, however upon inspection it is evident that there also exists a small range of $a_2 > 0$ for which the dynamics remain stable. In fact, certain eigenvalues of the system have a positive real part approximately when $a_2 > 21.5\mu$, as is shown in Fig. 6.15b. This is sufficient to determine the stability of the equilibrium point since whenever one of the eigenvalues possess a non-zero real part, an identical eigenvalue with opposite sign always exists, as confirmed by the trace of the matrix $\boldsymbol{A}$ being equal to zero.

a_2	x_{L_3}	x_{L_1}	x_{L_2}	C_{L_3}	C_{L_1}	C_{L_2}
5μ	-0.99881	0.93285	1.06825	3.02001	3.03939	3.03814
5.91μ	-0.99852	0.93294	1.06815	3.02348	3.0395	3.03826
6.82μ	-0.99824	0.93302	1.06804	3.02694	3.03962	3.03838
7.27μ	-0.99795	0.93311	1.06794	3.0304	3.03973	3.0385
8.64μ	-0.99766	0.93319	1.06784	3.03386	3.03985	3.03862
9.55μ	-0.99737	0.93328	1.06774	3.03733	3.03996	3.03874
10.45μ	-0.99709	0.93337	1.06764	3.04079	3.04007	3.03886
11.36μ	-0.99680	0.93345	1.06754	3.04425	3.04019	3.03898
12.27μ	-0.99651	0.93354	1.06743	3.04771	3.0403	3.03910
13.18μ	-0.99622	0.93362	1.06733	3.05117	3.04041	3.03922
14.09μ	-0.99594	0.93370	1.06723	3.05463	3.04053	3.03934
15μ	-0.99565	0.93379	1.06713	3.05809	3.04064	3.03945

Table 6.4: Locations and Jacobi integral values of, L_1, L_2, and L_3 for $5\mu \leq a_2 \leq 15\mu$.

As with Steering Law 1, there exists a value of acceleration beyond which the L_2 point possesses higher potential than L_3. There also exists, beyond a slightly higher thrust-induced acceleration, a region in which both L_1 and L_2 are points of higher potential than L_3. In Table 6.4, the locations and Jacobi constants of the three collinear equilibrium points are given for a range of a_2 between 5μ and 15μ. The point at which the potential at an equilibrium point becomes greater than L_3 can be found where its Jacobi constant falls below that of L_3. Thus, using linear interpolation, it can be shown that L_2 exceeds the potential of L_3 for approximately $a_2 > 9.93\mu$, and that L_1 exceeds L_3 for approximately $a_2 > 10.25\mu$. Note that both of these values lie within the region where the dynamics at L_4 and L_5 are stable, and so there exists a small region in which both L_1 and L_2 are points of greater potential than L_3 and stable librations around L_4 and L_5 are possible, i.e. $10.25\mu < a_2 < 21.5\mu$. In this case, tadpole orbits around either L_4 or L_5 can occur, but horseshoe orbits are replaced by crescent-shaped orbits which do not contain L_3. An example crescent-shaped orbit within this range of a_2 is shown in Fig. 6.16.

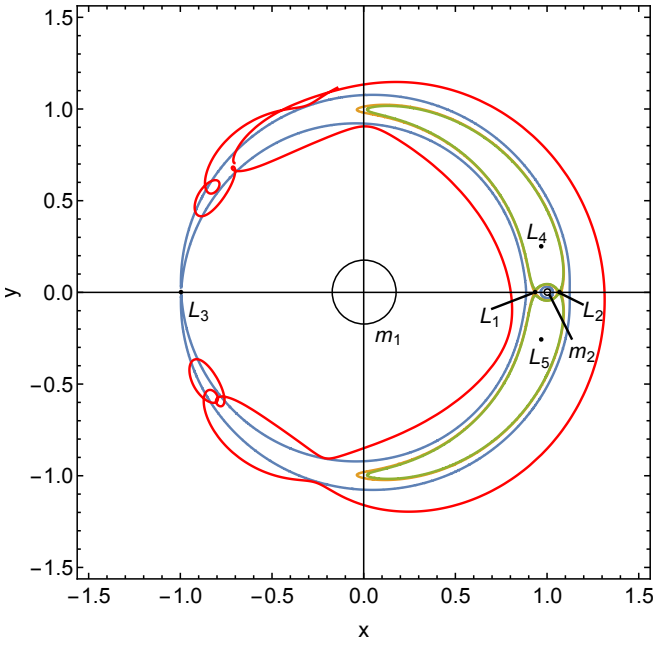

Figure 6.16: Crescent-shaped orbit with $a_1 = 0$ and $a_2 = 15\mu$. The red curve is the spacecraft's trajectory, the blue curve is the L_3 zero-velocity curve, and the orange and green curves are the zero-velocity curves associated with L_1 and L_2, respectively. Initial conditions are $x_0 = -y_0 = -0.705164$, and $\dot{x}_0 = \dot{y}_0 = 0$. Note that the green and orange curves are very similar.

6.5.1 Summary of Horseshoe and Tadpole Motion with Steering Law 2

The available regions of motion with Steering Law 2 in the binary asteroid system ($\mu = 9.536 \times 10^{-4}$), examined over the range $-1000\mu \leq a_2 \leq 1000\mu$, can be summarised as follows:

- For the range $-1000\mu \leq a_2 \leq -2\mu$, the point of maximum potential of the system is located at L_3; L_4 and L_5 are in fact merged with L_3. Orbits around this point are stable, and can have horseshoe shape.

- For the range $-2\mu \leq a_2 \leq 21.5\mu$, the points of maximum potential of the system are located at L_4 and L_5, which are distinct from L_3. L_2 becomes of higher potential than L_3 for $a_2 > 9.93\mu$, and L_1 becomes of higher potential than L_3 for $a_2 > 10.25\mu$. Horseshoe orbits can occur for $a_2 < 9.93\mu$, but for the range $9.93\mu < a_2 < 21.5\mu$, horseshoe orbits are replaced by crescent-shaped orbits which do not contain L_3. Tadpole orbits can still occur.

- For $a_2 > 21.5\mu$, the dynamics at L_4 and L_5 are unstable, growing asymptotically closer to m_2 with increasing a_2. Tadpole, crescent, and horseshoe orbits are no longer seen to freely occur.

6.6 Steering Law 3: $a_1 = a_2$

Under Steering Law 3, the thrust-induced acceleration acting on the spacecraft is assumed to be generated in such a way that it can be decomposed into two vectors of equal magnitude, each directed along the radial vectors r_1 and r_2 from the primary masses. The vector field resulting from this steering law is shown in Fig. 6.17a. Note that the acceleration vectors precisely cancel along the line connecting the two primary masses.

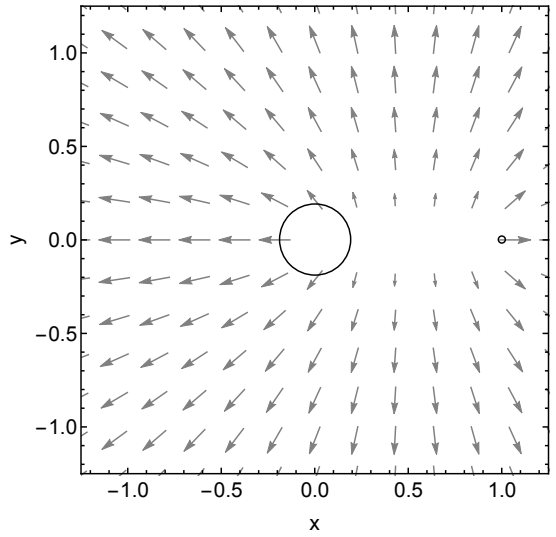

(a) Thrust-induced acceleration vector field.

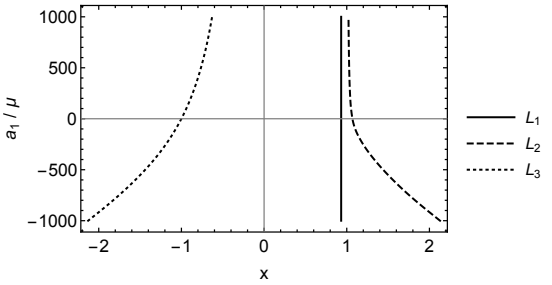

(b) Collinear equilibrium points.

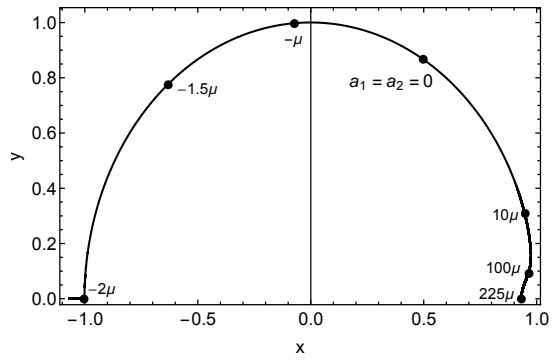

(c) L_4.

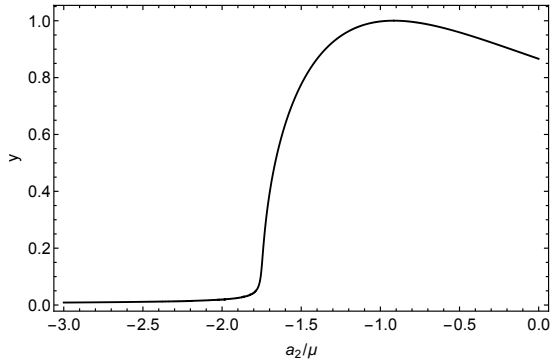

(d) y-coordinate of L_4 at merge with L_3.

Figure 6.17: Thrust-induced acceleration vector field (a), locations of the equilibrium points (b, c), and the merge of L_4 with L_3 (d) for Steering Law 3, with $-1000\mu \leq a_1 = a_2 \leq 1000\mu$.

As in the previous two Sections, a range of thrust-induced accelerations are applied under the current steering law, $-1000\mu \leq a_1 = a_2 \leq 1000\mu$, to examine the evolution of the critical zero-velocity curves of the system. Firstly, the evolution of the locations of the three collinear equilibrium points is shown in Fig. 6.17b. It can be seen that L_2 and L_3 both move towards the origin for $a_1 = a_2 > 0$, and that they grow further apart for $a_1 = a_2 < 0$. Since the acceleration vectors precisely cancel between the two masses, the location of L_1 is unaffected by this steering law.

Then, as in Sections 6.4 and 6.5, the locations of the triangular equilibrium points are located by numerically finding the points of maximum potential of the system. The evolution of the location of L_4 is shown in Fig. 6.17c for a range of accelerations. Note that, as in Section 6.5, there is a point at which the y-coordinate of L_4 collapses to zero, and for increasingly negative thrust-induced acceleration remains at zero. This indicates the point at which the L_4 and L_5 points merge with L_3, and a detailed plot of this region is provided in Fig. 6.17c. It can be shown that the merge, for this particular mass ratio, occurs at approximately $a_1 = a_2 = -2\mu$. A further critical acceleration is found when the L_4 and L_5 points merge with L_1. It can be shown that the merge between these points occurs at approximately $a_1 = a_2 = 224.9\mu$, and for acceleration values greater than this the equilibrium point with greatest potential is L_1.

Figures 6.18a and 6.18b show the regions where the dynamics close to L_4 and L_5 are stable and unstable. It can be noted that the dynamics at these points are unstable for approximately $a_1 = a_2 \geq 10.7\mu$.

The zero-velocity curve associated with the L_3 point is shown in Fig. 6.19 for a range of accelerations. As expected, the zero-velocity curve collapses into a single point for the cases $a_1 = a_2 \leq -90.9\mu$, as they are less than the merging value of $a_1 = a_2 = -2\mu$. The zero-velocity curves associated with L_1 and L_2 for a range of accelerations are shown in Fig. 6.20 and Fig. 6.21, respectively. The L_2 curve of zero velocity, for increasingly positive acceleration, draws into a small

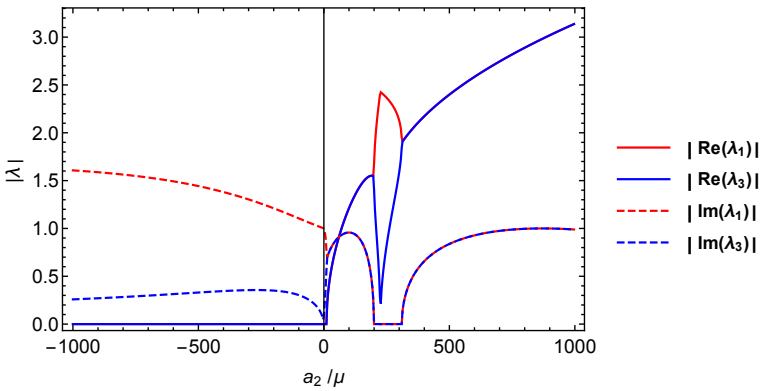

(a) Full range.

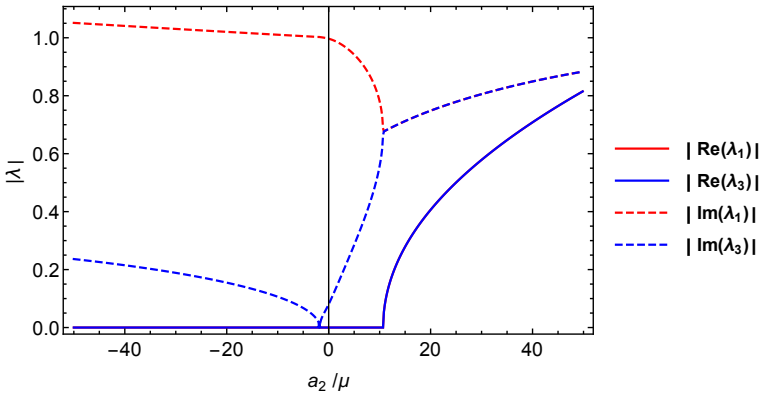

(b) Detailed plot at the unstable transition.

Figure 6.18: Eigenvalues of the linearised dynamics at L_4.

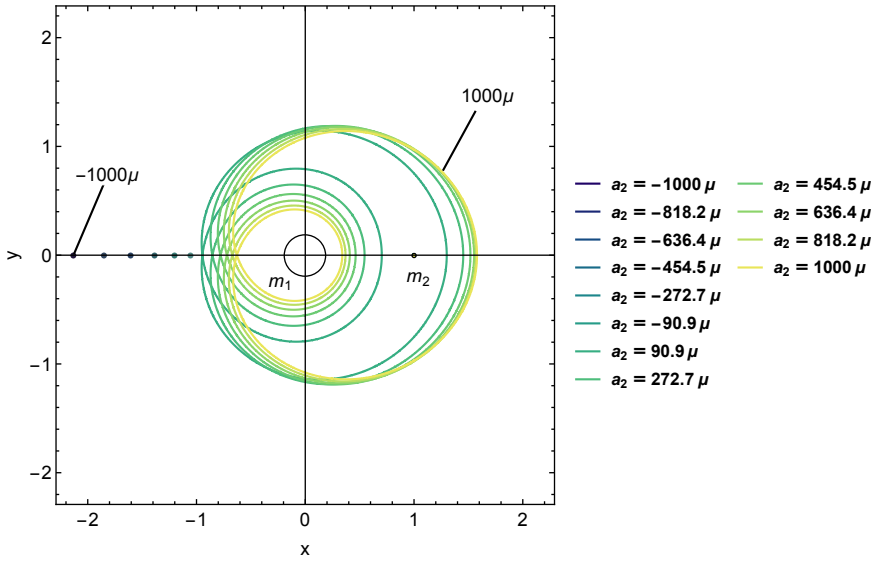

Figure 6.19: Zero-velocity curves associated with L_3 for Steering Law 3. For all contours where $a_1 = a_2 \leq -2\mu$ the curves have collapsed into a single point at L_3.

bubble surrounding the L_1 point, with the L_2 point itself drawing ever closer to m_2.

By examining the Jacobi constant associated with each of the collinear equilibria over a range of accelerations, the points beyond which L_1 becomes of higher potential than L_2 and L_3, and L_2 becomes of higher potential than L_3, can be found. These points are found at the intersection of the three curves in Fig. 6.22: L_1 exceeds the potential of L_2 for approximately $a_1 = a_2 > 4.81\mu$ and the potential of L_3 for approximately $a_1 = a_2 > 9.94\mu$; L_2 exceeds the potential of L_3 for approximately $a_1 = a_2 > 10.3\mu$. This figure also shows the region where the linearised dynamics at L_4 and L_5 become unstable, i.e. $a_1 = a_2 > 10.7\mu$. Thus, there exists a relatively small range of accelerations for which horseshoe motion is no longer possible while motion close to L_4 and L_5 is still stable. In the range $9.94\mu < a_1 = a_2 < 10.7\mu$, tadpole and crescent orbits are possible but horseshoe orbits are not. This occurs because the two lobes of the L_3 curve have become connected at L_1, such that a spacecraft with lower Jacobi constant than L_3 can no longer cross from the inner to outer regions of the system.

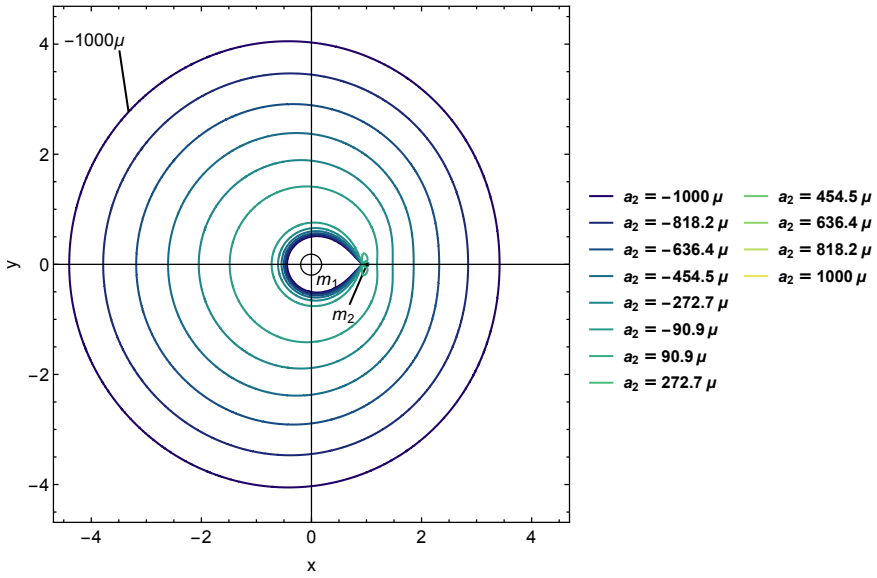

(a) System overview.

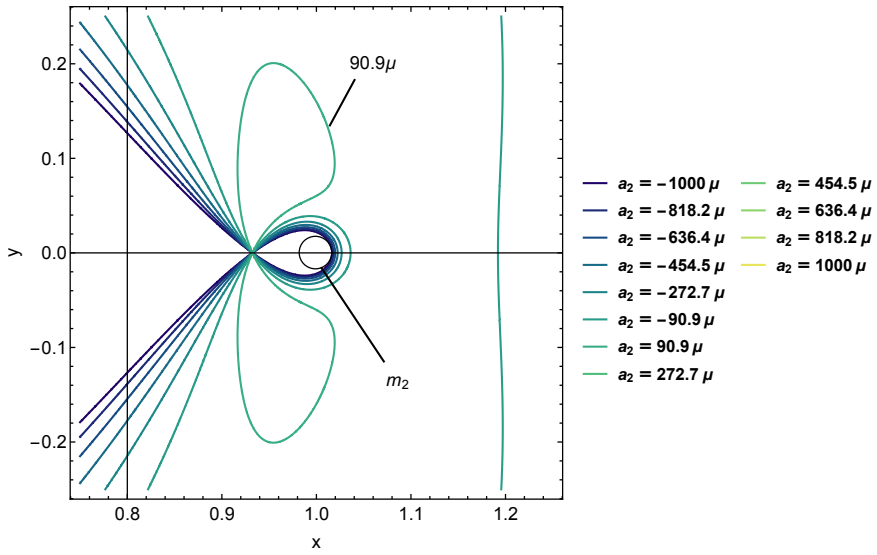

(b) Detailed plot around m_2.

Figure 6.20: Zero-velocity curves associated with L_1 for Steering Law 3.

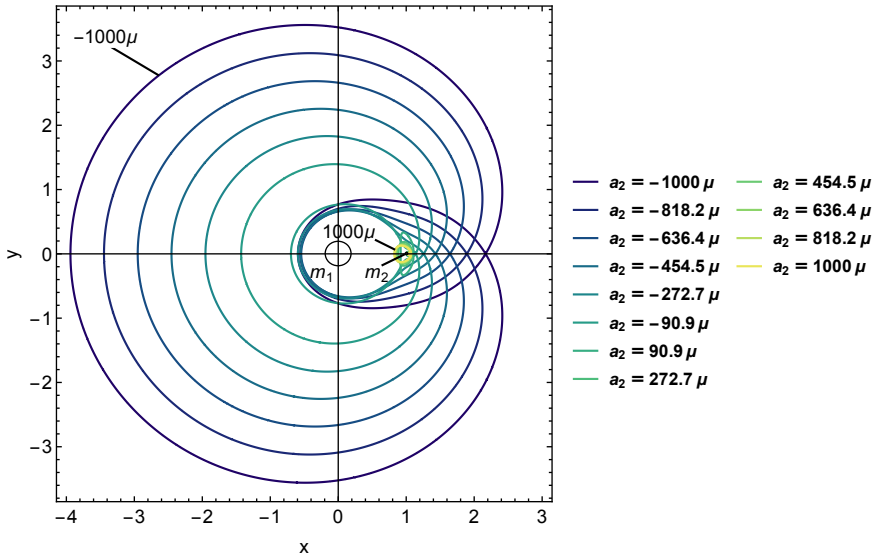

(a) System overview.

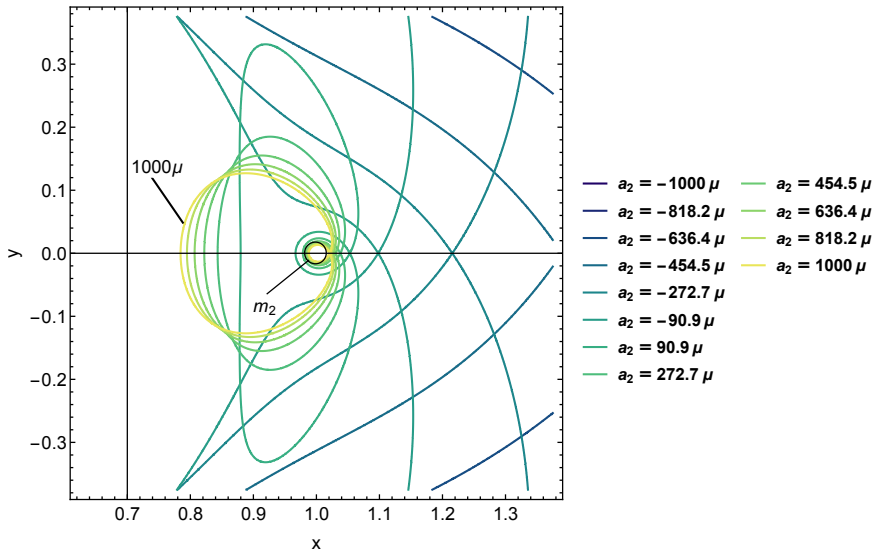

(b) Detailed plot around m_2.

Figure 6.21: Zero-velocity curves associated with L_2 for Steering Law 3.

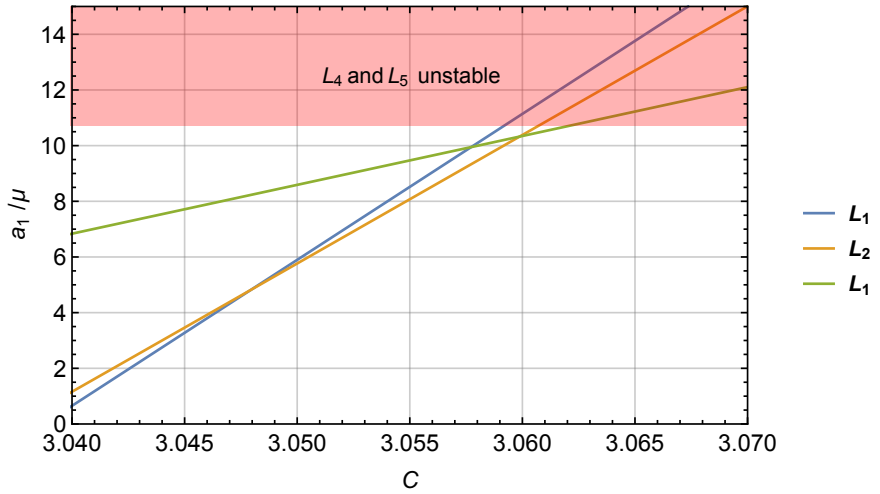

Figure 6.22: Jacobi constants for the collinear equilibria for a range of input thrust values, for Steering Law 3. The shading indicates the region in which the dynamics close to L_4 and L_5 are unstable.

6.6.1 Summary of Horseshoe and Tadpole Motion with Steering Law 3

The regions of motion which are achievable under Steering Law 3 in the binary asteroid system ($\mu = 9.536 \times 10^{-4}$), over the range of thrust-induced acceleration $-1000\mu \leq a_2 \leq 1000\mu$, can be summarised as follows:

- For $-1000\mu \leq a_1 = a_2 \leq -2\mu$, the system possesses only three equilibrium points, which are collinear along the x-axis. The point of maximum potential is located L_3, and motion close to this point is linearly stable. Horseshoe-shaped orbits can occur.

- For $-2\mu < a_1 = a_2 \leq 10.7\mu$ the system possesses five equilibrium points, three of which are collinear and two of which are triangular and symmetric about the x-axis. The points of maximum potential of the system are located at the triangular points, and motion close to these is linearly stable.

  - For $a_1 = a_2 > 4.81\mu$, the potential of L_1 exceeds that of L_2.

  - For $a_1 = a_2 > 9.94\mu$, the potential of L_1 exceeds that of L_3.

  - For $a_1 = a_2 > 10.3\mu$, the potential of L_2 exceeds that of L_3.
  - In the range $-2\mu < a_1 = a_2 < 9.94\mu$, tadpole, horseshoe, and crescent orbits are possible.
  - In the range $9.94\mu < a_1 = a_2 < 10.7\mu$, horseshoe orbits can no longer exist. Tadpole and crescent-shaped orbits may occur.

- For $10.7\mu \leq a_1 = a_2 \leq 224.9\mu$, motion around L_4 and L_5 is linearly unstable. Tadpole, horseshoe, and crescent orbits no longer freely occur, although periodic solutions may exist.

- For $a_1 = a_2 \geq 224.9\mu$, the L_4 and L_5 points have merged with L_1, which is the new location of the point of maximum potential. The motion around this point remains linearly unstable.

6.7 Conclusions

This Chapter has shown that the application of continuous thrust to the circular restricted three-body problem can modify the regions in which horseshoe and tadpole orbits occur, affecting not only the shape and period of such orbits but also the domain of their existence. Under different accelerations, the contours of pseudo-potential can change widely. The critical contour which governs horseshoe motion, the zero-velocity curve with potential equal to L_3, can be made to merge with L_3 and widen the available horseshoe region, or to close upon itself and entirely prevent horseshoe orbits from occurring. It is seen that when the L_3 zero-velocity curve does close, in a trisectrix-like form, a new type of motion replaces horseshoe motion: the crescent-shaped orbit. These orbits enclose L_1, L_2, L_4, and L_5, and exist at higher potential levels than L_3.

The effects of three different steering laws upon the locations of the equilibrium points of a system with the same mass ratio as the Sun-Jupiter system have been analysed in detail, and the locations and linear stability of L_4 and L_5 have been

investigated for a range of accelerations. The transitions at which L_4 and L_5 become stable or unstable have been identified, and the effect of these transitions on the existence of horseshoe orbits has been commented on. In general, negative acceleration (acceleration towards each of the primary masses) results in stable L_4 and L_5, and in two of the three steering laws this also results in a collapse of the L_3 zero-velocity curve, beyond which there exist only three equilibrium points. This widens the region in which horseshoe orbits occur, corresponding to a widening separation of the L_1 and L_2 points.

The analysis performed in this Chapter will be applied to the problem of finding thrust augmented horseshoe orbits which graze the surface of the smaller primary in the 243 Ida binary asteroid system in Chapter 7.

Chapter 7

Surface-Grazing Thrust Augmented Horseshoe Orbits

This Chapter addresses Objective 5 as described in Section 1.3, proposing a method to produce thrust augmented horseshoes orbits which rendezvous with the surface of the smaller primary in the CRTBP, providing new opportunities for touch-and-go sampling, specifically in binary asteroid systems. The structure of the Chapter is as follows: Section 7.1 describes the numerical methods used to find the initial conditions for periodic horseshoe orbits, Section 7.2 uses the analysis performed in Chapter 6 to modify the numerical methods of Section 7.1 for finding the initial conditions of periodic horseshoe orbits which graze the surface of the smaller primary, and finally Section 7.3 offers conclusions for the Chapter.

The same example system as was used in Chapter 6 is considered in this Chapter (243 Ida and Dactyl), with dimensional parameters identical to those established in Section 6.2. Building on the analysis of Chapter 6, which established the regions of thrust-induced acceleration in which horseshoe orbits can occur, a method is proposed for finding periodic horseshoe orbits which are symmetric about the x-axis of the CRTBP. This strategy, adapted from a method used to find Lyapunov orbits, is shown to be applicable to the thrust augmented CRTBP,

and both horseshoe and crescent-shaped orbits are found. A further technique is then proposed which finds the initial conditions for thrust augmented horseshoe orbits with close approaches to the smaller primary. With suitable acceleration under Steering Law 3 ($a_1 = a_2$) two members of a family of horseshoe orbits which rendezvous with the surface of the smaller primary are then shown.

7.1 Periodic Horseshoe Orbits

This Section details the methods used to obtain periodic (and near-periodic) horseshoe orbits in the thrust augmented CRTBP. Attempts are not made to exhaustively search for and define entire families of periodic orbits; instead, the tools described here are used to sample and analyse some of the periodic orbits which occur in the thrust augmented CRTBP. A shooting method is used to find the initial conditions for periodic orbits, with initial guesses produced using a search-and-filter technique which relies on certain simplifying assumptions.

As was pointed out by Deprit and Henrard [73], the search for families of periodic orbits in the CRTBP is often accidentally limited to finding only families of symmetric periodic orbits, since the conditions for periodicity and symmetry are sometimes the same, as defined by the mirror theorem [100]. In fact, the CRTBP allows for large families of periodic orbits which are asymmetric about the x-axis, including asymmetric horseshoe orbits, as was demonstrated numerically by Taylor [74]. However, limiting the search to only symmetric periodic orbits does offer advantages, chiefly in the simplified process for locating initial guesses. Furthermore, symmetric periodic horseshoe orbits could offer operational advantages for space missions, for example by allowing a spacecraft to approach two sides of the smaller primary of a binary asteroid system at equal distance for sampling. As such, the method detailed here for finding periodic orbits only seeks those which are symmetric about the x-axis, and is a modification of the method often used to find Lyapunov orbits.

The search-and-filter method is performed as follows. First, consider a horseshoe orbit which crosses the x-axis at only two points, and each crossing is perpendicular to the x-axis. Choosing a starting position on the x-axis, y_0 and $\dot{x}_0$ are therefore zero, while x_0 and $\dot{y}_0$ are non-zero. A symmetric orbit, which is also therefore periodic in this case, is found when the next crossing of the x-axis is perpendicular. This requires that the velocity in the x-direction at the time of crossing, $\dot{x}_c$, is equal to zero. Selecting x_0, the equations of motion can be numerically integrated for a range of $\dot{y}_0$ until the following x-axis crossing, at which point $\dot{x}_c$ is recorded. Interpolation between the points $(\dot{x}_c, \dot{y}_0)$ will reveal the approximate initial velocity at which $\dot{x}_c = 0$.

The range of $\dot{y}_0$ can be limited so that the Jacobi constant of the spacecraft is greater than the Jacobi constant of L_3, meaning that the potential of the spacecraft is lower than that of L_3. This ensures that the orbits are limited by the critical tadpole curve, and may encircle L_3, L_4, and L_5. The orbits found with perpendicular crossings of the x-axis can then be filtered by only selecting those that cross to the left of m_1, i.e. $x_c < -\mu$, since an orbit crossing to the right of this is unlikely to be a horseshoe orbit. It can be noted that under certain accelerations a horseshoe orbit may have more than two crossings of the x-axis, but this search-and-filter technique disregards these in favour of those with only two crossings.

An example analysis of $\dot{x}_c$ for a range of $\dot{y}_0$ is given in Fig. 7.1, where $x_0 = -1.04$ and $a_1 = a_2 = 0$. The detailed plot in Fig. 7.1b shows the points which were used for initial guesses. Note that some $\dot{y}_0$-axis crossings are ignored: these crossings are close to being perpendicular due to the rapidly changing shape of the function [75], and so do not provide useful initial guesses. These graphs were generated using Mathematica's Reap/Sow, NDSolve, and ListPlot functions. Other similar graphs in this Chapter were also generated using these functions.

The data associated with the initial guesses of Fig. 7.1b can be found in Table 7.1. The estimate of the orbit half-period $T_o/2$ is obtained by noting the time at

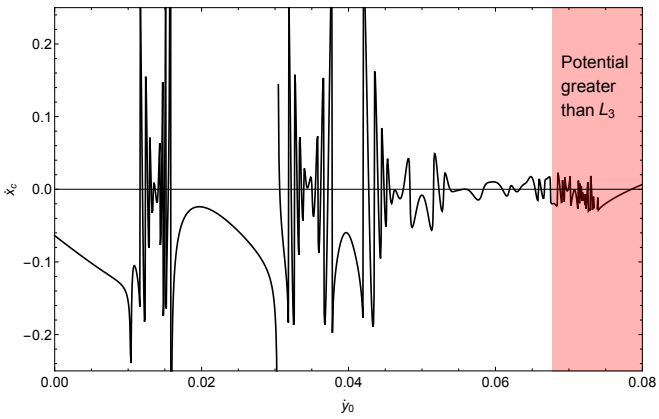

(a) Full range of $\dot{y}_0$ applied to the system.

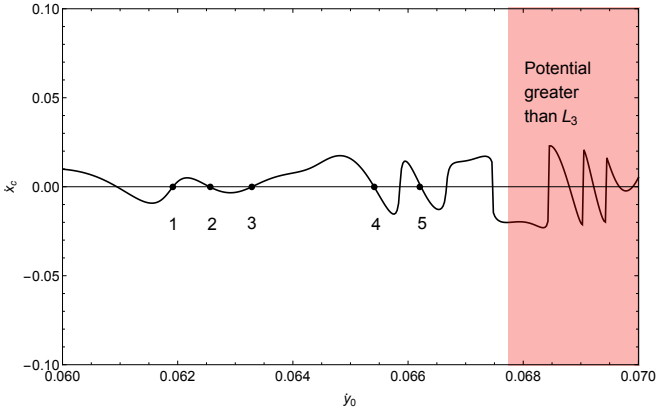

(b) Detailed plot illustrating points used as initial guesses for horseshoe orbits.

Figure 7.1: Component of velocity in x-direction at first x-axis crossing for a range of $\dot{y}_0$, where $x_0 = -1.04$ and $a_1 = a_2 = 0$. Perpendicular crossings of the x-axis are found where $\dot{x}_c = 0$. The red shaded region indicates potential levels greater than that of L_3, where horseshoe orbits are unlikely to occur.

No.	x_0	$\dot{y}_0$	$T_o/2$	x_c
1	-1.04000	0.061927	83.4035	-0.975053
2	-1.04000	0.0625515	86.025	-0.968231
3	-1.04000	0.0632906	88.0239	-0.978787
4	-1.04000	0.0654096	91.9400	-0.95692
5	-1.04000	0.0662243	98.1633	-0.965717

Table 7.1: Details of the initial guesses from Fig. 7.1, where $a_1 = a_2 = 0$.

which the perpendicular x-axis crossing occurs.

A shooting method is then implemented to attempt to find the initial conditions required for a precisely periodic orbit. The initial guesses generated by the search-and-filter process are used as the starting conditions in a boundary value problem, which is solved using the NDSolve function in Wolfram Mathematica. This function uses a shooting method to locate the correct initial conditions.

For a nonlinear second-order problem, the shooting method works as follows. The initial and final conditions of the system can be given in vector form, which for an orbit with perpendicular crossings will be

$$\boldsymbol{x}_0 = \begin{bmatrix} x_0 \\ y_0 \\ \dot{x}_0 \\ \dot{y}_0 \end{bmatrix} = \begin{bmatrix} x_0 \\ 0 \\ 0 \\ \dot{y}_0 \end{bmatrix} = \boldsymbol{x}_{T_o} = \begin{bmatrix} x_{T_o} \\ y_{T_o} \\ \dot{x}_{T_o} \\ \dot{y}_{T_o} \end{bmatrix} = \begin{bmatrix} x_{T_o} \\ 0 \\ 0 \\ \dot{y}_{T_o} \end{bmatrix} \tag{7.1}$$

where the subscript $_{T_o}$ denotes the state after one orbit period. Denote the guess $\dot{y}_0 = s$, where s can be considered the 'shooting angle' [123]. The solution to this initial value problem is found by numerical integration of the equations of motion. The solution to the initial value problem which satisfies the boundary conditions is therefore the solution to the boundary value problem, and is denoted as $\dot{y}_0 = s^*$. To find $s = s^*$ which satisfies $x_0 = x_{T_o}$ and $\dot{y}_0 = \dot{y}_{T_o}$, an iterative method is used, such as Newton's method (which is the default method used by NDSolve for boundary value problems [124]).

No.	x_0	y_0	$\dot{x}_0$	$\dot{y}_0$	Orbit Type
1	-1.04	0	-0.000655090	0.0619706	Horseshoe
2	-1.04	9.70854×10^{-11}	-0.0000142319	0.0625519	Horseshoe
3	-1.04	0	-2.12274×10^{-6}	0.0632904	Horseshoe
4	-1.04	2.0335×10^{-12}	-0.000215065	0.0654221	Horseshoe
5	-1.04	-4.30516×10^{-9}	-3.54953×10^{-6}	0.0662244	Horseshoe

Table 7.2: Outcomes of the attempted solution of the boundary value problems using starting conditions from Table 7.1, where $a_1 = a_2 = 0$.

To further the earlier example, the initial guesses from Table 7.1 are given as the starting conditions for a series of NDSolve boundary value problems. The results of these numerical procedures are given in Table 7.2. Also noted is whether the initial value solutions converged with the boundary value problem within 100 iterations, along with the scaled residual boundary error returned by the function. As can be seen, each of the guesses from Fig. 7.1b converged to a precisely periodic orbit.

It should also be noted that all of the orbits found in Table 7.2 are of horseshoe shape, as seen in the converged orbits of Fig. 7.2, and are therefore indicative of horseshoe behaviour for this range of initial conditions. Convergence depends strongly on the accuracy of the initial guess, particularly in the regions of the $\dot{x}_c$ plot which are less smooth. These graphs were generated using Mathematica's NDSolve and ParametricPlot functions. Other similar graphs in this Chapter were generated in the same way.

Furthermore, it is evident that the orbit period increases with $\dot{y}_0$, which corresponds to the orbits existing closer and closer to the L_3 zero-velocity curve: a horseshoe orbit following this curve would be of infinite period. In agreement with this observation, the orbit guess with the closest approach to m_2 is number 1, which is the leftmost guess in Fig. 7.1. This orbit has the lowest value of Jacobi constant of all the guesses, and is thus bounded by a wider zero-velocity curve. It can therefore be supposed that for any given x_0 through which periodic horseshoe orbits pass, the horseshoe orbit with the closest approach to m_2 is likely to be

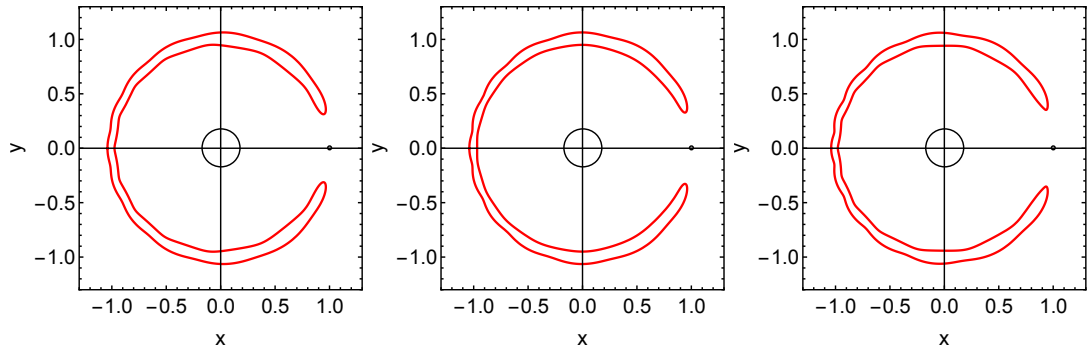

(a) Orbit 1 (b) Orbit 2 (c) Orbit 3

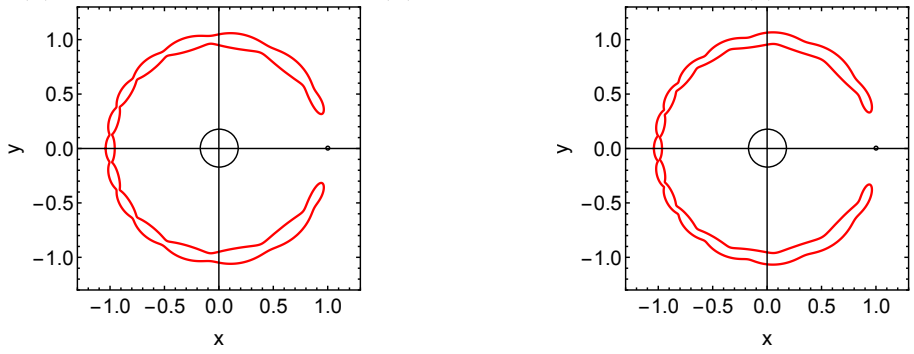

(d) Orbit 4 (e) Orbit 5

Figure 7.2: Converged periodic orbits from Table 7.2. The spacecraft's trajectory is shown in red.

that with the lowest $\dot{y}_0$. This result proves useful in the search for a horseshoe orbit which closely approaches or performs a rendezvous with m_2, as will be seen in the following Section (Section 7.2).

A wider appreciation of the existence and behaviour of periodic orbits in the system can be obtained when the procedure used to generate Fig. 7.1 is repeated over a range of x_0. Figure 7.3 shows $\dot{x}_c$ for a grid of 102×102 orbits (generated using Mathematica's Reap/Sow, NDSolve, and ListPointPlot3D functions), and it can be seen that the region containing the most periodic orbits (where $\dot{x}_c = 0$ crossings occur) takes the form of an approximately diagonal band across the surface generated. Running within this band, there exist many families of discontinuous parallel or near-parallel curves. In this context, a family of periodic orbits can be defined by finding the $\dot{x}_c = 0$ crossings for a single diagonal strip. It can also be seen that, with increasingly negative acceleration under Steering Law 3, the diagonal strip containing the $\dot{x}_c = 0$ crossings becomes more ordered, smooth, and with fewer crossings. This corresponds to a decrease in the number of periodic orbits which can be found in this way.

It is also illuminating to examine the case of positive acceleration under Steering Law 3. Recalling from Section 6.6 that the acceleration at which the L_4 and L_5 stability transition is found is at $a_1 = a_2 = 10.7\mu$, a stable value close to this limit is chosen, $a_1 = a_2 = 10\mu$. The resulting surface for $\dot{x}_c$ is shown in Fig. 7.4a. It can be seen that there are relatively few crossings in the range examined, with the greatest number of crossings occurring close to L_3 for lower values of $\dot{y}_0$. At this acceleration level, as can be found in Section 6.6, the potential of L_1 is greater than L_3, and the points of maximum potential of the system are located at the triangular points, but horseshoe orbits are no longer possible because the two lobes of the L_3 zero-velocity curve have become connected at L_1. For example, sampling the graph at $x_0 = -1.1$, there are four $\dot{x}_c = 0$ crossings with lower potential than L_3, but none of these yield a horseshoe orbit: all x_c crossing locations are positive and beyond the orbit of m_2.

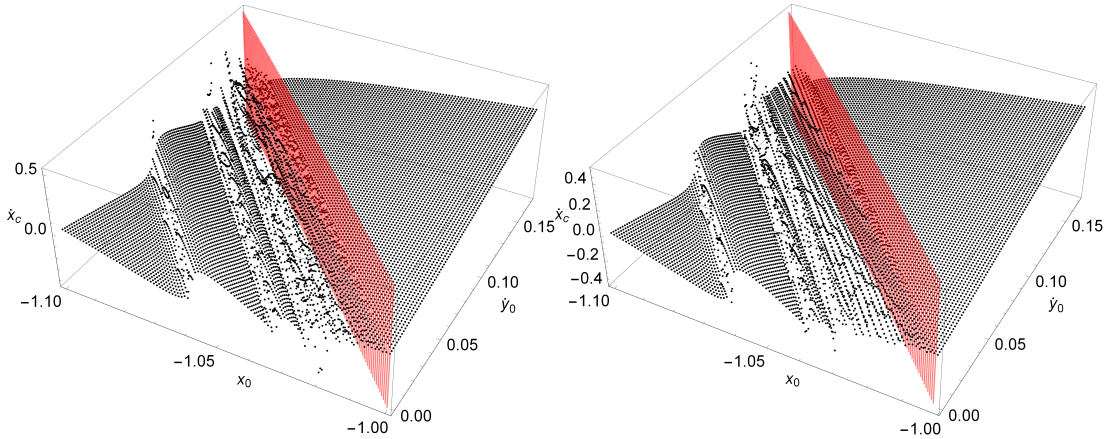

(a) $a_1 = a_2 = 0$

(b) $a_1 = a_2 = -2\mu$

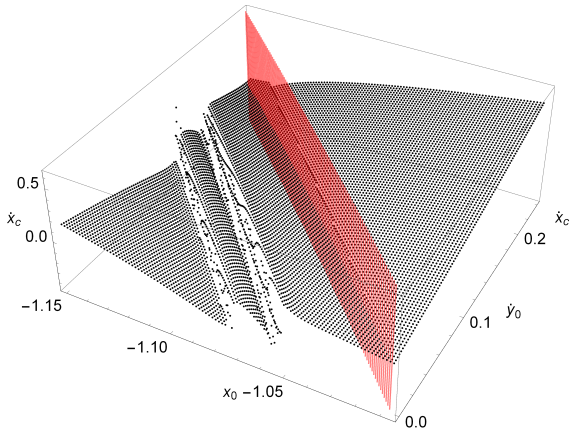

(c) $a_1 = a_2 = -10\mu$

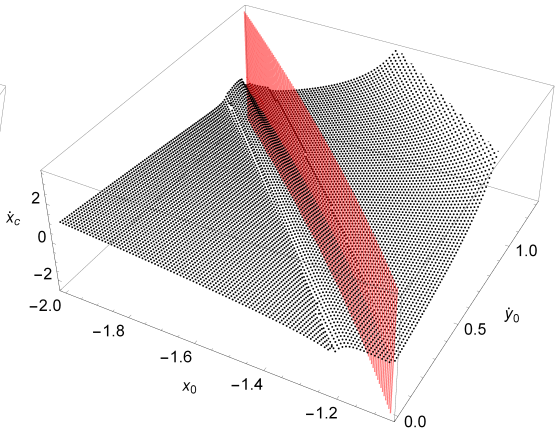

(d) $a_1 = a_2 = -100\mu$

Figure 7.3: Variation in $\dot{x}_c$ over a range of x_0 and $\dot{y}_0$. The red surface indicates the energy level of L_3.

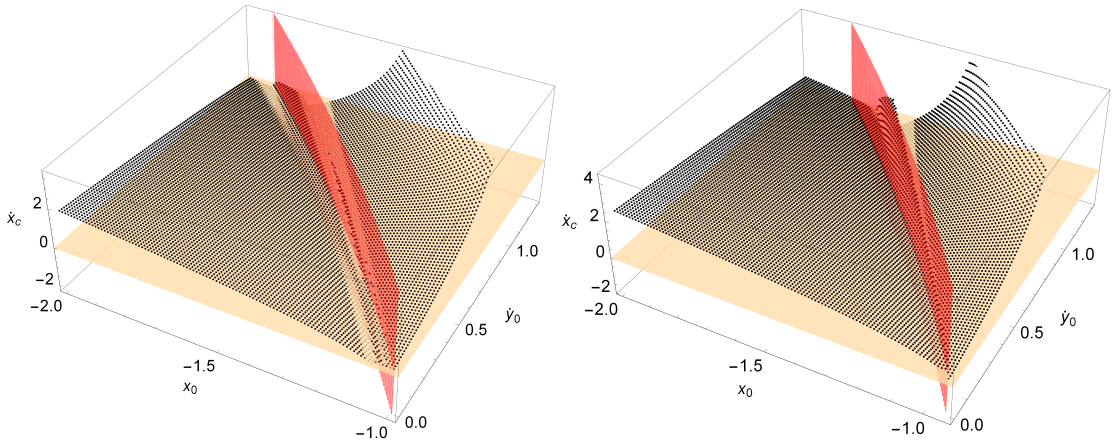

(a) $a_1 = a_2 = 10\mu$ (b) $a_1 = a_2 = 100\mu$

Figure 7.4: Variation in $\dot{x}_c$ over a range of x_0 and $\dot{y}_0$. The red surface indicates the energy level of L_3, and the plane at $\dot{x}_c = 0$ is used to illustrate crossings. Note that there appear to be no crossings with lower potential than L_3 for $a_1 = a_2 = 100\mu$.

If crescent-shaped orbits are sought instead of horseshoe orbits, a different range of x_0 should be used as these orbits do not cross the negative x-axis. In Fig. 7.5a, the range used is $x_0 > x_{L_2}$, and a large region of crossings is readily apparent. Selecting a single initial position, $x_0 = 1.2$, the search-and-filter process is used to locate an initial guess, which is in turn used to seed a shooting method to find precise initial conditions for a periodic orbit. The crescent orbit found in this manner is shown in Fig. 7.6a.

Extending the analysis even further by selecting an acceleration in the range which produces unstable dynamics at L_4 and L_5 also produces interesting results. As has already been stated, horseshoe orbits are not possible with Steering Law 3 for $a_1 = a_2 > 9.94\mu$, because of the trisectrix form of the L_3 zero-velocity curve. When selecting $a_1 = a_2 = 100\mu$, the surface of $\dot{x}_c$ to the right of L_2 possesses fewer $\dot{x}_c = 0$ crossings, as can be seen in Fig. 7.5b. Taking the sample $x_0 = 1.4$, it is found that there are only two crossings of $\dot{x}_c = 0$. The leftmost of these produces a wide crescent orbit, with shape reminiscent of a large-amplitude Lyapunov orbit, and the rightmost crossing produces a wide system-encircling orbit. The crescent orbit found is shown in Fig. 7.6b.

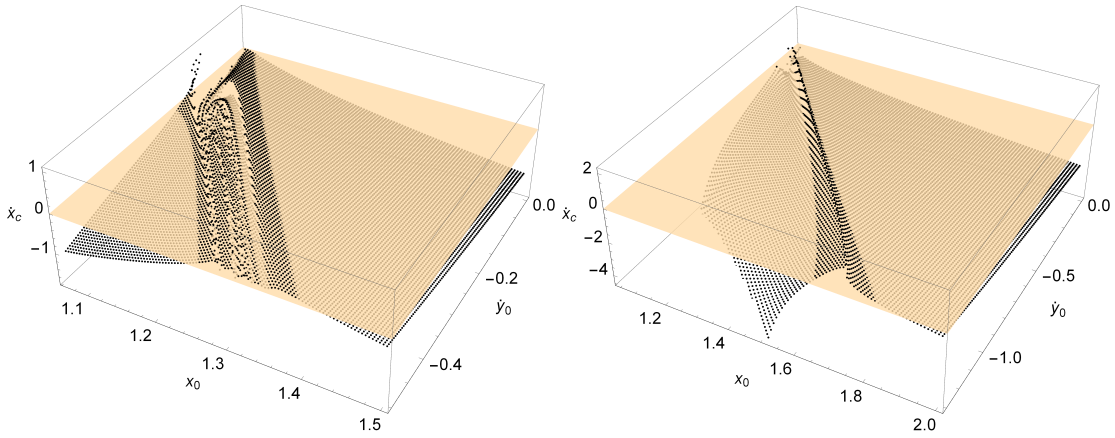

(a) $a_1 = a_2 = 10\mu$ (b) $a_1 = a_2 = 100\mu$

Figure 7.5: Variation in $\dot{x}_c$ over a range of x_0 and $\dot{y}_0$. The plane at $\dot{x}_c = 0$ is used to illustrate crossings. Note that the ranges of x_0 are beyond L_2.

7.2 Rendezvous with the Smaller Primary

The objective stated at the beginning of this Chapter was to investigate the feasibility of a surface-grazing rendezvous with the smaller primary using a thrust augmented horseshoe orbit. This Section addresses this concept, and details the methods used to seek such a rendezvous.

As a basic concept, a horseshoe orbit is envisaged for which the points of closest approach to m_2 almost contact the surface. The points of closest approach occur at the parts of the trajectory where the spacecraft turns from the outer orbit to the inner and vice-versa, which are termed the horns of the horseshoe. These features tend to deform to follow the contours of pseudo-potential around the smaller mass. An orbit with relatively high energy is unlikely to descend close to the primaries, due to the steep gradient of the pseudo-potential near these points.

It was noted in Section 7.1 that, when plotting $\dot{x}_c$ against $\dot{y}_0$, the periodic horseshoe orbit with the closest approach to m_2 is generally the leftmost orbit yielded by the search-and-filter process. This corresponds to the periodic horseshoe orbit with the lowest potential and highest Jacobi constant of all periodic solutions with only two x-axis crossings, for a given x_0. It is possible to perform

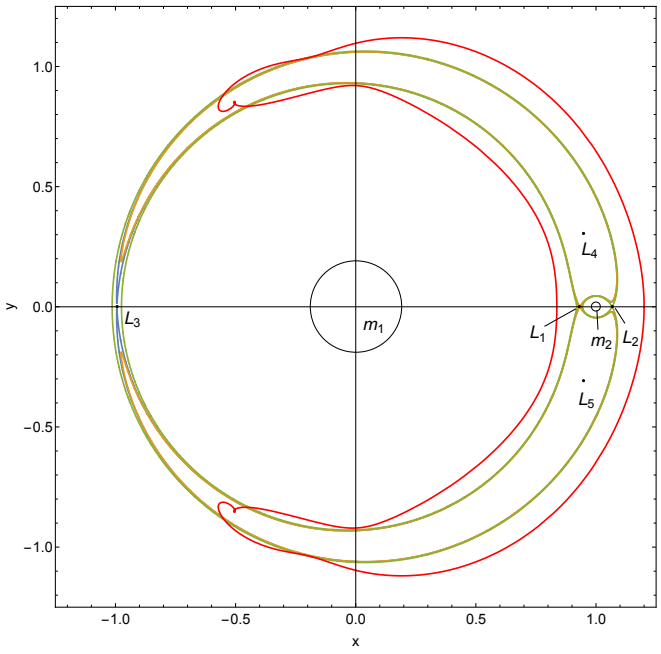

(a) $a_1 = a_2 = 10\mu$, $x_0 = 1.2$, $y_0 = 0$, $\dot{x}_0 = -0.000015$, $\dot{y}_0 = -0.296301$.

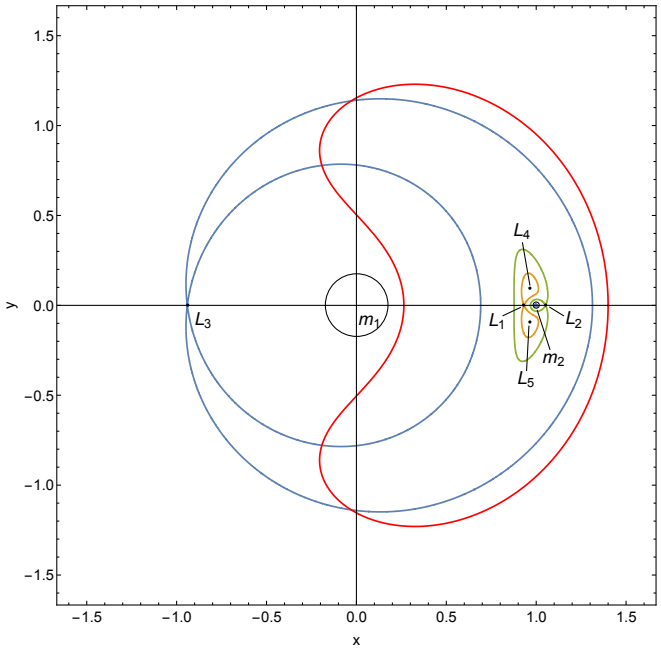

(b) $a_1 = a_2 = 100\mu$, $x_0 = 1.4$, $y_0 = 0$, $\dot{x}_0 = -0.000208$, $\dot{y}_0 = -0.721176$.

Figure 7.6: Periodic crescent-shaped orbits shown in red. The blue curve represents the zero-velocity curve for L_3, the orange for L_1, and the green for L_2. Note that, in (a), the orange and green curves are very similar.

an exhaustive sweep, finding the leftmost periodic horseshoe for each x_0 and checking for a suitably close approach to m_2. However, this method is labour-intensive and may not return a rendezvous solution. Instead, it is recognised that a periodic horseshoe orbit which approaches m_2, due to the deformation of its trajectory close to the mass may in fact cross the x-axis at more than two points. Therefore, the search-and-filter method wherein only the first re-crossing of the axis is recorded misses periodic orbits with more than one crossing. This does not mean that the aforementioned search-and-filter method is without use in this case, rather that it must be adapted for this specific purpose.

It is proposed here that instead of simply looking for $\dot{x}_c = 0$ crossings, the value of $\dot{y}_0$ which is likely to yield a close encounter with m_2 is sought: the value of $\dot{y}_0$ which provides the desired rendezvous will be very close to this value. The rapidly steepening potential gradient close to m_2 results in high sensitivity to initial conditions for trajectories which pass through this region, and so it can be expected that the graph of $\dot{x}_c$ will exhibit rapid change nearby the encounter. In fact, this is usually seen as a spike in the graph, and it delineates the boundary between the range of initial conditions which produce horseshoe orbits and those which produce system-encircling orbits. An example graph of $\dot{x}_c$ against $\dot{y}_0$ is given in Fig. 7.7, where the region of system-encircling orbits is shown along with the point at which the trajectories encounter m_2. For the system shown, a first guess for a non-periodic close-approach horseshoe is marked with the red point. The initial velocity at this point is $\dot{y}_0 = 0.01150$, and as expected produces a non-periodic trajectory with horseshoe-like behaviour and a close approach to m_2. Furthermore, the trajectory does indeed cross the x-axis at more than two points, and in fact passes between m_2 and L_1. This trajectory is shown in Fig. 7.8. However, due to the complexity of this orbit, it is not straightforward to estimate the half-period for the purposes of using a differential corrector to find a periodic solution, and so a smoother trajectory is sought.

It was noted in Section 6.6 that applying negative acceleration with Steering

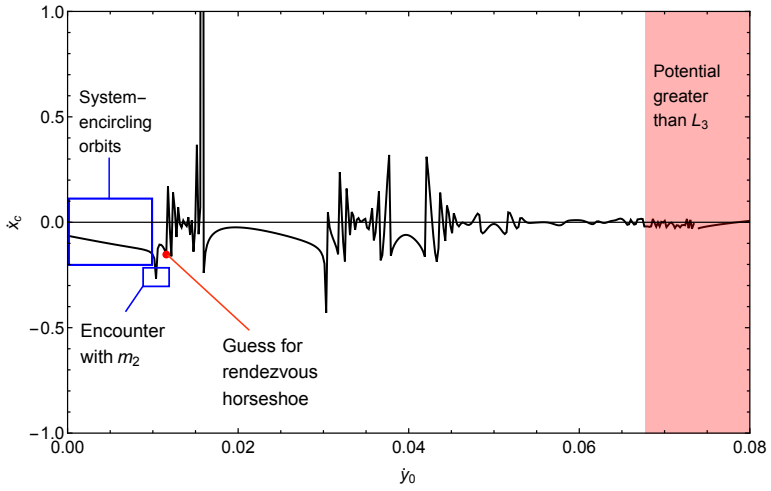

Figure 7.7: Crossing velocity $\dot{x}_c$ against $\dot{y}_0$ for $x_0 = -1.04$ and $a_1 = a_2 = 0$. The point at which the trajectories encounter m_2 and the region in which system-encircling orbits exist are highlighted. Horseshoe orbits exist to the right of the encounter.

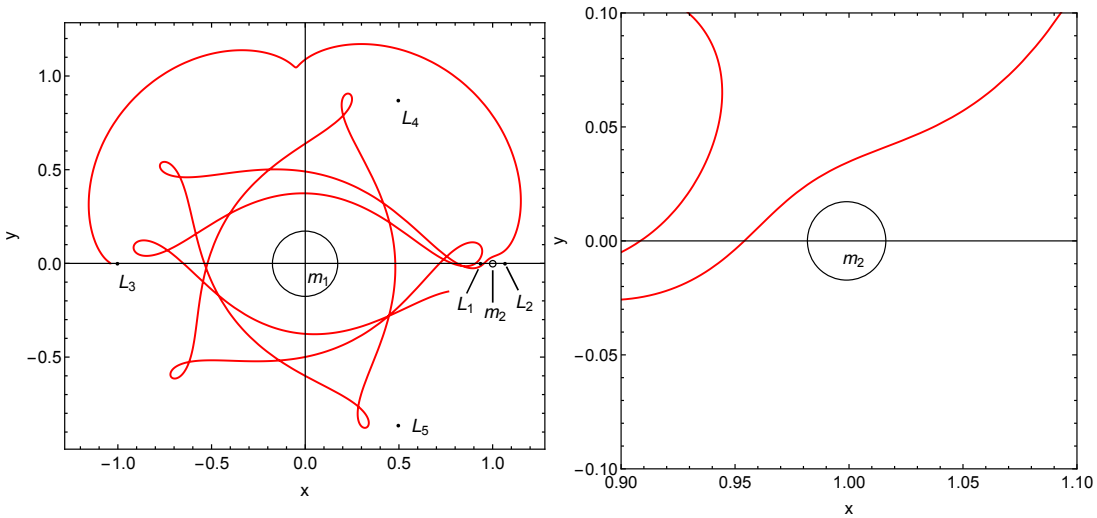

(a) System overview.

(b) Region near m_2.

Figure 7.8: Non-periodic close-approach trajectory (red) exhibiting horseshoe-like behaviour, for $a_1 = a_2 = 0$, $x_0 = -1.04$, $y_0 = 0$, $\dot{x}_0 = 0$, and $\dot{y} = 0.01150$.

Law 3 results in increasing separation of the collinear equilibrium points, with only the L_2 point remaining fixed. This corresponds to a widening of the region in which horseshoe orbits are possible, and horseshoe orbits with greater separation between the inner and outer arcs tend to have a shorter period and therefore fewer loops. This allows for the period of an initial guess to be more accurately estimated, and in turn aids the shooting method to converge on a precisely periodic orbit.

Choosing $a_1 = a_2 = -80\mu$, which merges L_4 and L_5 with L_3 and widens the L_1 and L_2 zero-velocity curves, an initial position distant from L_3 ($x_{L_3} = -1.05390$) but within these curves is first selected, $x_0 = -1.4$. Then $\dot{x}_c$ can be plotted for a range of $\dot{y}_0$ to locate the approximate initial velocity which causes an encounter with m_2. The earlier analysis suggests that this occurs at the leftmost region of rapid change in the graph of $\dot{x}_c$, due to increased sensitivity to initial conditions nearby the encounter. Orbits to the left of the encounter are expected to be system-encircling orbits, while orbits to the right are expected to exhibit horseshoe behaviour.

The graph of $\dot{x}_c$ is given in Fig. 7.9a, where the location of the initial guess for a rendezvous horseshoe orbit is indicated. The encounter with m_2 takes place slightly to the left of this on the edge of the smoother section of the curve. The period T of the orbit is estimated by numerically integrating the equations of motion with this guess until the orbit re-crosses the x-axis close to its starting point. Then, the initial guess (x_0, $\dot{y}_0$, T) is supplied to NDSolve, returning the initial conditions for a precisely periodic horseshoe orbit which closely approaches the surface of m_2.

It is desired to find a closer approach, so a wider horseshoe orbit of the same family is sought. Using $x_0 = -1.5$, the graph of $\dot{x}_c$ is given in Fig. 7.9b. The initial guess is taken from the point which is analogous to that of the previous value of x_0, and NDSolve returns another periodic, symmetric horseshoe orbit which performs an even closer approach to the surface of m_2. This orbit not only

a_1	a_2	x_0	y_0	$\dot{x}_0$	$\dot{y}_0$	$T/(2\pi)$
-80μ	-80μ	-1.40000	0.00000	0.0575745	0.329428	3.85155
-80μ	-80μ	-1.50000	0.00000	-0.0184697	0.472008	3.78789

Table 7.3: Initial conditions for two symmetric, periodic thrust augmented horseshoe orbits which perform a close approach or rendezvous with the smaller primary, m_2.

contains L_3 (and thereby the point of maximum potential of the system), but also L_2 as it crosses and re-crosses the x-axis on either side of this equilibrium point. Furthermore, it is indicative of a family of periodic close-approach orbits whose approach distance may be adjusted by varying x_0. These two orbits, whose initial conditions are listed in Table 7.3, are shown in Fig. 7.10.

The spacecraft's distance from the surface of m_2, and its speed, v, are shown in Fig. 7.11. It can be seen that the orbit with the greater approach distance has a speed at rendezvous of approximately 2.7 ms^{-1}, while the orbit with the closer approach passes m_2 at a lower speed of 2.5 ms^{-1}.

Integrating the magnitude of the thrust-induced acceleration ($|\boldsymbol{a}| = \sqrt{a_x^2 + a_y^2}$) over a single orbit period for each horseshoe orbit yields the Δv expended by the spacecraft. It is found that the orbit with the furthest approach requires 18.5 ms^{-1} per orbit, and the orbit with the closer approach requires 18.1 ms^{-1} per orbit.

The maximum magnitude of the acceleration when $a_1 = a_2 = -80\mu$ occurs at all points on the x-axis to the left of m_1. The value is simply $|\boldsymbol{a}| = 160\mu$, which is equivalent to a dimensional acceleration of 5.28×10^{-5} ms^{-2}. For a 100 kg spacecraft, this would require a maximum thrust of 5.28 mN, which is readily achievable with existing electrostatic thruster technology. Assuming that the spacecraft is equipped with a single thruster, an additional advantage of $a_1 = a_2 < 0$ is that the exhaust plume is never directed towards m_2, and so impingement and contamination of the surface is avoided. Although the thrust must be accurately throttled, the simplicity of the steering law could allow a

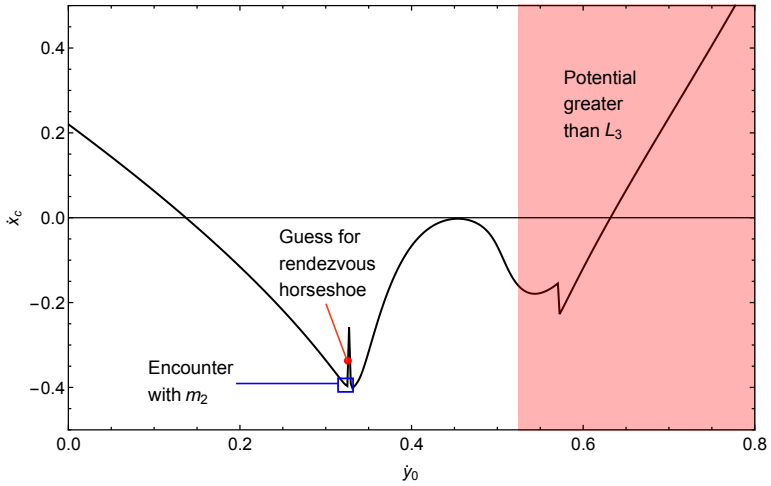

(a) $x_0 = -1.4$

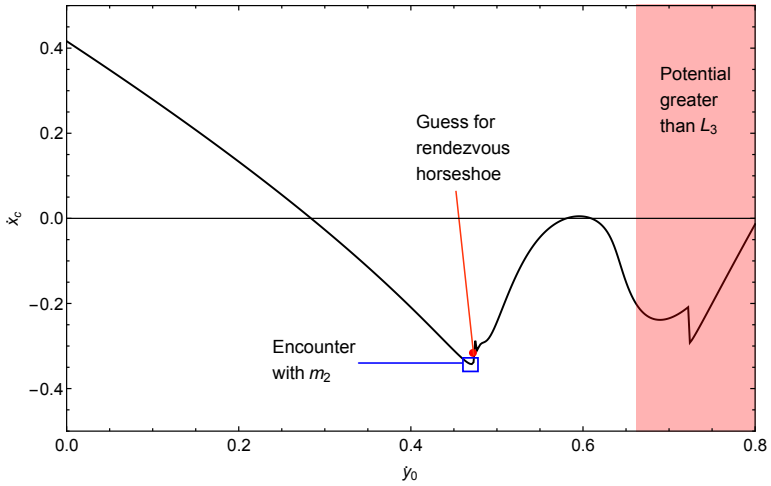

(b) $x_0 = -1.5$

Figure 7.9: Crossing velocity $\dot{x}_c$ against $\dot{y}_0$ for $x_0 = -1.4, -1.5$, and $a_1 = a_2 = -80\mu$. The approximate region in which the trajectories encounter m_2 and the initial guesses for rendezvous horseshoe orbits are highlighted.

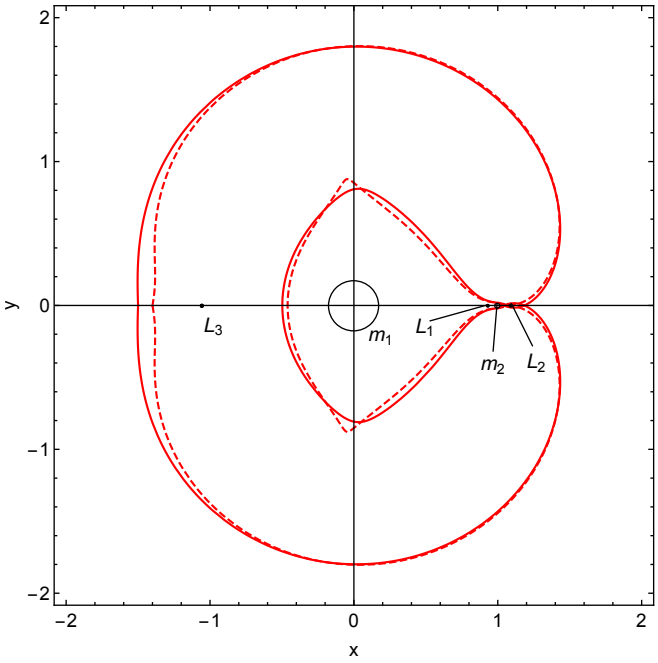

(a) System overview.

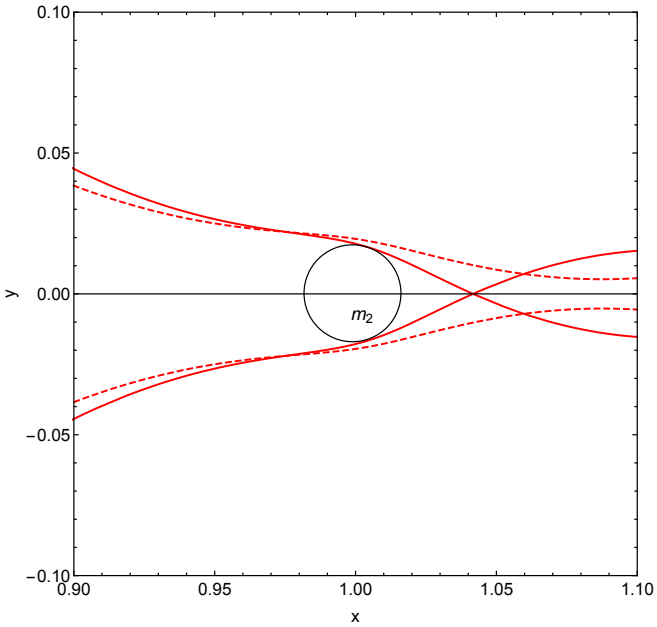

(b) Region near m_2.

Figure 7.10: Two members of a family of periodic, symmetric horseshoe orbits with close approaches to m_2, for $a_1 = a_2 = -80\mu$. The full orbits are shown in (a), and a detailed plot showing the trajectories close to m_2 is shown in (b). The dashed and solid red curves correspond to the first and second orbits in Table 7.3, respectively.

spacecraft to find the unit vectors to m_1 and m_2 using a camera, as discussed in Section 6.1.

7.3 Conclusions

A method for locating initial conditions for symmetric periodic orbits, adapted from that used to find Lyapunov orbits, is employed to find periodic horseshoe and crescent orbits. However, this method is shown to miss periodic orbits with more than two crossings of the axis which connects the primary masses. The method is adapted to locate the initial conditions for thrust augmented horseshoe orbits which rendezvous with the smaller primary, and two members of a family of symmetric, periodic orbits which approach closely to or rendezvous with the smaller primary are found using this method. The speed of a spacecraft at rendezvous on each of these two orbits is found to be relatively small, the maximum thrust magnitude is readily achievable using existing technology, and the Δv requirements are shown to be modest.

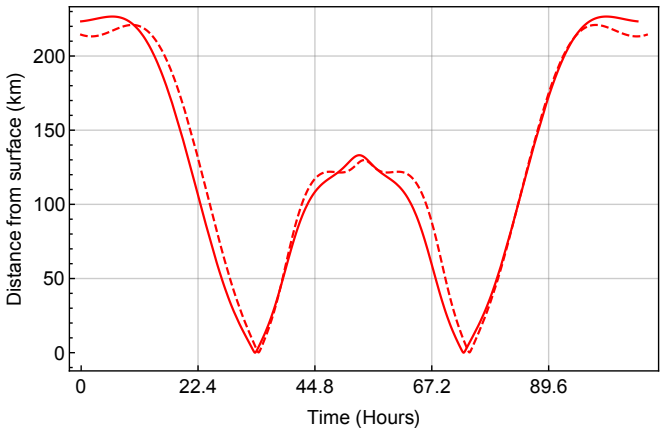

(a) Distance from the surface of m_2.

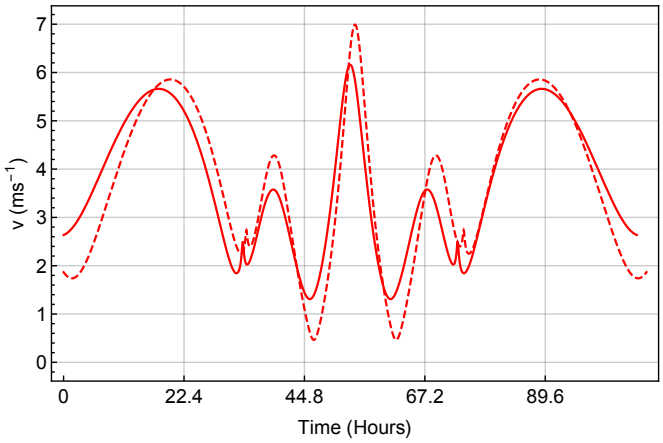

(b) Speed of the spacecraft.

Figure 7.11: Distance of the spacecraft from the surface of m_2 is shown in (a), and the spacecraft's speed relative to m_2 is shown in (b) for two members of a family of periodic, symmetric horseshoe orbits with close approaches to m_2, with $a_1 = a_2 = -80\mu$, in dimensional units. The dashed and solid lines correspond to the first and second orbits in Table 7.3, respectively.

Chapter 8

Conclusion

This Thesis has presented rich new families of thrust augmented orbits in both the two-body problem (Hill-Clohessy-Wiltshire approximation) and the circular restricted three-body problem. Continuous low thrust has been used to generate modified-period non-Keplerian orbits, halo-type orbits, and artificial horseshoe orbits, with potential applications in stellar interferometry, on-orbit inspection, constellation forming, and binary asteroid sampling. Each new orbit type has been developed using assumptions derived from the use of small, low-cost spacecraft, recognising that such spacecraft typically have limited on-board sensing and computational power. The strategies used to develop these new families of orbits have taken these limitations into account, by assuming the use of position-only feedback to control the continuous thrust and through the use of simple steering laws. This Thesis has thus proposed that great utility can be derived from the application of continuous thrust to the two-body and circular restricted three-body problems. The conclusions drawn from each Chapter are given as follows.

8.1 Chapter 3

In Chapter 3, it was shown that low thrust can augment the capabilities of formations of spacecraft through enabling motion on forced non-Keplerian orbits. The Hill-Clohessy-Wiltshire approximation of spacecraft motion relative to a target on a circular two-body orbit was made closed-loop, using position-only feedback to modify the eigenvalues and, therefore, the natural frequencies of spacecraft relative motion. Such a control strategy enables small, low-cost spacecraft to access rich new families of thrust augmented orbits. Due to the decoupling of the in-plane and out-of-plane dynamics for small displacements, the two natural frequencies can be made distinct with thrust, enabling new multiply-periodic orbits. Additionally, the thrust commands required for a circular orbit of arbitrary radius, orientation, and period relative to a target were derived parametrically. When combined with modified-period out-of-plane motion, cylindrical relative orbits are enabled, including an orbit in which the spacecraft tracks the Sun vector around a geostationary target. Such a family of orbits has wide-ranging applications, from space situational awareness to solar observation or shielding. Furthermore, the propellant requirements for the new families of orbits are small when the use of electrostatic propulsion is assumed.

8.2 Chapter 4

In Chapter 4, continuous low thrust was used to generate interesting new families of stable orbits in the vicinity of a libration point in the circular restricted three-body problem, using the strategy proposed in Chapter 3. Through the linearisation of the dynamics of a spacecraft relative to a collinear libration point, position-only feedback was used to manipulate the system eigenvalues and therefore the natural frequencies of motion. Although the dynamics close to the collinear libration points are normally unstable, they can be made stable through the ap-

propriate selection of feedback gains such that new quasi- and multiply-periodic orbits can be designed. In addition, the gain conditions required to synchronise the in-plane and out-of-plane natural frequencies were derived, enabling stable, three-dimensional, halo-type orbits of arbitrary dimensions. Such an orbit could provide a constantly visible communications relay, if around the Earth-Moon L_2 point, for lunar far-side missions. Similarly to Chapter 3, such a control strategy would enable low-cost spacecraft to access these new families of orbits, and the propellant required to maintain such orbits is also small when using electrostatic propulsion.

8.3 Chapter 5

In Chapter 5, certain aspects of three-body co-orbital motion (specifically horseshoe orbits) were replicated in the Hill-Clohessy-Wiltshire approximation by using low thrust manoeuvres. Thrust commands were derived to enable two different types of artificial horseshoe orbit. The first type required only thrust in the along-track direction to transfer a spacecraft between a circular outer orbit and an elliptical inner orbit, and the second type used thrust in both the along-track and radial directions to generate a horseshoe orbit with circular inner and outer orbits. Using only two manoeuvres, it is possible to generate horseshoe orbits of arbitrary length. Furthermore, since the duration of both types of low thrust transfers are constant, synchronised constellations of spacecraft on nested horseshoe orbits are enabled. Using the strategy for modulation of the out-of-plane frequency from Chapter 3, constellations can also be nested in three dimensions. This concept provides interesting new opportunities for telecommunications or Earth-observation constellations which can be reconfigured according to local demand.

8.4 Chapter 6

In Chapter 6, continuous thrust was applied to a spacecraft in the circular restricted three-body problem to modify the domain of existence of horseshoe orbits. The existence of such orbits was shown to be governed by the zero-velocity curve associated with the L_3 point, and by the linear stability of the L_4 and L_5 points. In the 243 Ida binary asteroid system, three steering laws were analysed in which constant thrust-induced acceleration was directed along either or both of the unit radius vectors from the two primary bodies. The effects of the steering laws on the locations of the five equilibrium points of the three-body system were recorded in detail, and the stability of the linearised dynamics at L_4 and L_5 under different accelerations was analysed. It was shown that thrust directed towards the two primaries generally resulted in Lyapunov-stable dynamics at L_4 and L_5, while thrust directed away from the two primaries generally resulted in unstable dynamics at these points. Furthermore, thrust-induced acceleration caused the shape of the L_3 zero-velocity curve to change, and can be made to either close entirely upon itself and prevent horseshoe orbits, or to merge with L_3 and widen the region in which horseshoe orbits occur. When the L_3 zero velocity curve does close upon itself, it was found that crescent-shaped orbits (a new type of orbit which encloses the L_1, L_2, L_4, and L_5 points) replace horseshoe orbits.

8.5 Chapter 7

In Chapter 7, the analysis of Chapter 6 was applied to find periodic horseshoe orbits which rendezvous with the surface of the smaller asteroid of a binary pair (243 Ida). A strategy similar to that used to find the initial conditions for symmetric periodic Lyapunov orbits was used to locate horseshoe orbits, however this strategy missed orbits which cross the axis connecting the two primary bodies at more than two points. Since orbits which approach the smaller primary

closely are likely to cross this axis at more than two points, the strategy was adapted by instead selecting initial conditions from the range which produced horseshoe orbits with the lowest pseudo-potential. As was shown in Chapter 6, wider horseshoe orbits with lower pseudo-potential could be found using thrust directed towards the two primaries, since this widened the region in which horseshoe orbits were likely to occur. Using low thrust and the adapted method, two members of a family of symmetric, thrust augmented, periodic horseshoe orbits with close approaches to the smaller primary were presented. Additionally, the speed of the spacecraft at rendezvous was found to be small in both cases, offering interesting new opportunities for touch-and-go sampling of binary asteroids.

8.6 Future Work

The research presented in this Thesis satisfied the objectives described in Chapter 1, by developing rich new families of thrust augmented orbits for spacecraft motion relative to a target on a circular two-body orbit and relative to a collinear libration point in the CRTBP. Certain aspects of three-body co-orbital motion were replicated in the HCW approximation using low thrust, and by analysing the effects of continuous thrust on the generation of horseshoe orbits in the CRTBP surface-grazing orbits for binary asteroid sampling were also found. These objectives were achieved, however each Chapter represents only the first steps into potentially rich new avenues of research, and there is scope for further investigation in these areas.

A common objective shared by all Chapters in this Thesis is the use of simple techniques and steering laws to enable access to these new families of orbits for small, low-cost spacecraft. Reference has been made to the low mass and limited complexity of such spacecraft, and the resulting limited sensing and on-board computation capabilities. As such, a useful extension of the research in this Thesis would be the investigation of the relative navigation systems which would

enable the new families of orbits. RADAR and LIDAR are often used for relative navigation by larger spacecraft, however few such solutions exist for nanosatellites due to insufficient mass, power, and computational capabilities. Cameras offer an interesting potential solution, due to the miniaturisation of such technology for modern smartphones and other applications, and although some authors have considered these (e.g. [87]) there is room for further development of the concept. Such concepts usually rely on retroreflection of light emitted by a beacon [87] or a projection of a pattern by a laser source [132], since passive sensing concepts such as the Universal Docking Port have proven to lack robustness against varied ambient light conditions [86] for close proximity operation applications. For the three steering laws proposed in Chapter 6, only knowledge of the direction to each of the primaries in a binary asteroid system is required. This has been considered in part by Torre et al., who investigated the stationkeeping of one or more spacecraft at the L_4 point in a binary asteroid system, where each spacecraft is equipped with a camera to observe both primaries for angles-only navigation [133]. Although this was primarily for stationkeeping purposes, the concept could be developed further for co-orbital motion in the binary asteroid system.

With the continuing miniaturisation of computers, it can be expected that on-board image processing and computer vision capabilities will improve, allowing for the development of more accurate and sophisticated relative navigation systems for miniature spacecraft. However, in the absence of ideal sensors and image processing capabilities, it would be useful to consider the effects of uncertainty of relative position measurement on the generation and stability of the new families of orbits. State estimation techniques can be applied, such as Kalman filters, in order to make the system more robust to uncertainty. For example, in the presence of nonlinear three-body dynamics, Torres et al. used an Unscented H-infinity Filter for state estimation [133], and similar methods can be applied to two-body dynamics under orbital perturbations.

It was suggested in Chapter 1 that a camera unit on-board a nanosatellite

could be used for both relative navigation and on-orbit inspection of a target, and so a future research avenue could be the development and demonstration of such a multipurpose system. Interesting challenges would be found in the provision of adequate illumination and image fidelity for both purposes, including the selection of imager wavelength bands and an assessment of the associated power and mass requirements.

In addition to the future work proposed above, suggestions for each Chapter are given as follows:

- The research in Chapter 3 and Chapter 4 will benefit from the inclusion of perturbations in both the two-body and three-body approximations, in order to find the control accelerations required to counteract these for each of the new families of orbits. Additionally, if it is assumed that the spacecraft cannot counteract these perturbations, it will be useful to find the stability and lifetime of the thrust augmented orbits to ascertain their feasibility under these conditions.

- While the artificial horseshoe orbits of Chapter 5 offer useful new opportunities for phased and nested constellations, it would be interesting to extend the concept through the use of artificial potential fields centred on a spacecraft or reference point, such that the influence of the potential field could be used to shepherd a ring system of small satellites, much in the same way that certain small moons shepherd the rings of planets such as Saturn or Uranus [112, 113]. Such a system could be used to provide a truly reconfigurable constellation, adjusting the density of satellites over particular longitudes through the adjustment of the artificial potential field instead of synchronised low thrust manoeuvres.

- The work in Chapter 6 could be extended by including steering laws with thrust which varies with radial displacement, in order to analyse the effects of varying acceleration on the zero-velocity curves and associated co-orbital

motion types. Such a development could allow for interesting cases where the triangular equilibrium points are brought closer to the smaller primary and yet remain stable, permitting interesting new hovering and librating orbits in the circular restricted three-body problem. Furthermore, the system could be replaced by the elliptic restricted three-body problem, in order to provide analysis which is more applicable to real systems.

- Chapter 7 could also be extended by searching for crescent-shaped orbits which rendezvous with the surface of the smaller primary body, allowing for the sampling of different faces of an asteroid in a binary pair. Additionally, a more exhaustive search for families of horseshoe and crescent-shaped orbits with close approaches could be performed, allowing for optimisation of propellant expenditure, orbit period, and speed relative to the body at rendezvous.

Bibliography

[1] J.-L. Lagrange, Essai sur le probleme des trois corps, *Prix de lacadémie royale des Sciences de paris*, vol. 9, p. 292, 1772.

[2] H. M. Dusek, Motion in the vicinity of libration points of a generalized restricted three-body model, *Progress in Astronautics and Aeronautics*, Vol. 17, pp. 37-54, 1966.

[3] C. R. McInnes, A. J. C. McDonald, J. F. C. Simmons, E. W. McDonald, Solar sail parking in restricted three-body systems, *Journal of Guidance, Control and Dynamics*, vol. 17, no. 2, pp. 399-406, 1994.

[4] M. Y. Morimoto, H. Yamakawa, K. Uesugi, Artificial equilibrium points in the low-thrust restricted three-body problem, *Journal of Guidance, Control, and Dynamics*, Vol. 30, No. 5, 2007. doi: 10.2514/1.26771

[5] R. L. Forward, Light-levitated geostationary cylindrical orbits using perforated light sails, *Journal of the Astronautical Sciences*, vol. 32, no. 2, pp. 221-226, 1984.

[6] S. Baig, C. R. McInnes, Artificial three-body equilibria for hybrid low-thrust propulsion, *Journal of Guidance, Control, and Dynamics*, Vol. 31, No. 2, pp. 1644-1655, 2008.

[7] C. Bombardelli, J. Peláez, On the stability of artificial equilibrium points in the circular restricted three-body problem, *Celestial Mechanics and Dynamical Astronomy*, Vol. 109, No. 1, pp. 13-26, 2011. doi: 10.1007/s10569-010-9317-z

[8] G. Aliasi, G. Mengali, A. A. Quarta, Artificial equilibrium points for a generalized sail in the elliptic restricted three-body problem, *Celestial Mechanics and Dynamical Astronomy*, Vol. 114, No. 1-2, pp. 181-200, 2012. doi: 10.1007/s10569-012-9425-z

[9] H. Lei, B. Xu, Invariant manifolds around artificial equilibrium points for low-thrust propulsion spacecraft,*Astrophysics and Space Science*, vol. 362, no. 75, 2017.

[10] A. K. de Almeida Jr., A. F. B. A. Prado, D. M. Sanchez, T. Yokoyama, Searching for artificial equilibrium points to place satellites "above and below" L_3 in the Sun-Earth system, *Revista Mexicana de Astronomia y Astrofisica*, vol. 53, pp. 349-359, 2017.

[11] A. K. de Almeida Jr., A. F. B. A. Prado, T. Yokoyama, D. M. Sanchez, Spacecraft motion around artificial equilibrium points, *Nonlinear Dynamics*, vol. 91, pp. 1473-1489, 2018.

[12] H. Yang, X. Bai, S. Li, Artificial equilibrium points near irregular-shaped asteroids with continuous thrust, *Journal of Guidance, Control, and Dynamics*, vol. 41, no. 6, pp. 1308-1319, 2018.

[13] R. L. Forward, Statite: a spacecraft that does not orbit, *Journal of Spacecraft and Rockets*, vol. 28, no. 5, pp. 606-611, 1991.

[14] C. R. McInnes, *Solar Sailing: Technology, Dynamics and Mission Applications*, Springer Praxis, London, 1999.

[15] R. Austin, R. Dod, C. Terwilliger, The ubiquitous solar electric propulsion stage, *Acta Astronautica*, vol. 4, no. 5, pp. 671-694, 1977.

[16] K. T. Nock, Rendezvous with Saturns rings, *Planetary rings: 1st international meeting*, CNES, Toulouse, France, pp. 743-759, 1984.

[17] G. J. Yashko, D. E. Hastings, Analysis of thruster requirements and capabilities for local satellite clusters, *10th AIAA/USU Conference on Small Satellites*, AIAA, Logan, Utah, 1996.

[18] C. R. McInnes, The existence and stability of families of displaced two-body orbits, *Celestial Mechanics and Dynamical Astronomy*, Vol. 67, No. 2, pp. 167-180, 1997. doi: 10.1023/A:1008280609889

[19] C. R. McInnes, Dynamics, stability, and control of displaced non-Keplerian orbits, *Journal of Guidance, Control, and Dynamics*, Vol. 21, No. 5, pp. 799-805, 1998. doi: 10.2514/2.4309

[20] D. J. Scheeres, Stability of hovering orbits around small bodies, *Advances in the Astronautical Sciences*, Vol. 102, pp. 855-875, 1999.

[21] M. Xu, S. Xu, Nonlinear dynamical analysis for displaced orbits above a planet, *Celestial Mechanics and Dynamical Astronomy*, Vol. 102, No. 4, pp. 327-353, 2008. doi: 10.1007/s10569-008-9171-4

[22] M. Ceriotti, C. R. McInnes, Natural and sail-displaced doubly-symmetric Lagrange point orbits for polar coverage, *Celestial Mechanics and Dynamical Astronomy*, Vol. 114, No. 1-2, pp. 151-180, 2012. doi: 10.1007/s10569-012-9422-2

[23] R. J. McKay, M. Macdonald, J. Biggs, C. R. McInnes, Survey of highly non-Keplerian orbits with low-thrust propulsion, *Journal of Guidance, Control, and Dynamics*, Vol. 34, No. 3, pp. 645-666, 2011. doi: 10.2514/1.52133

[24] J. Heiligers, C. R. McInnes, J. D. Biggs, M. Ceriotti, Displaced geostationary orbits using hybrid low-thrust propulsion, *Acta Astronautica*, Vol. 71, pp. 51-67, 2012. doi: 10.1016/j.actaastro.2011.08.012

[25] Y. Tsuda, O. Mori, R. Funase, H. Sawada, T. Yamamoto, T. Saiki, T. Endo, K. Yonekura, H. Hoshino, J.I. Kawaguchi, Achievement of IKAROSJapanese deep space solar sail demonstration mission, *Acta Astronautica*, Vol. 82, No. 2, pp. 183-188, 2013. https://doi.org/10.1016/j.actaastro.2012.03.032

[26] D. Alhorn, J. Casas, E. Agasid, C. Adams, G. Laue, C. Kitts, S. O'Brien Nanosail-d: The small satellite that could! *25th Annual AIAA/USU Conference on Small Satellites*, Ogden, UT, 2011. https://doi.org/10.1016/j.actaastro.2012.03.032

[27] P. Janhunen, Electric sail for spacecraft propulsion, *Journal of Propulsion and Power*, Vol. 20, No. 4, pp. 763-764, 2004.

[28] G. Mengali, A. A. Quarta, P. Janhunen, Electric sail performance analysis, *Journal of Spacecraft and Rockets*, Vol. 45, No. 1, pp. 122-129, 2008. https://doi.org/10.2514/1.31769

[29] G. Mengali, A. A. Quarta, Non-Keplerian orbits for electric sails, *Celestial Mechanics and Dynamical Astronomy*, Vol. 105, No. 1-3, pp. 179-195, 2009.

[30] W. Wang, G. Mengali, A. A. Quarta, J. Yuan, Formation flying for electric sails in displaced orbits. Part I: Geometrical analysis, *Advances in Space Research*, 2017. http://dx.doi.org/10.1016/j.asr.2017.05.015

[31] W. Wang, G. Mengali, A. A. Quarta, J. Yuan, Formation flying for electric sails in displaced orbits. Part II: Distributed coordinated control, *Advances in Space Research*, 2017. http://dx.doi.org/10.1016/j.asr.2017.06.017

[32] R. Wirz, M. Gale, J. Mueller, C. Marrese, Miniature ion thrusters for precision formation flying, *40th AIAA/ASME/SAE/ASEE Joint Propulsion Conference and Exhibit*, Fort Lauderdale, Florida, AIAA 2004-4115, 2004 doi: 10.2514/6.2004-4115

[33] P. N. Randall, R. A. Lewis, S. D. Clark, QinetiQ T5 based electric propulsion system and architectural options for future applications, *35th International Electric Propulsion Conference*, Atlanta, GA, 2017.

[34] M. Hutchins, H. Simpson, J. P. Jiménez, QinetiQ's T6 and T5 ion thruster electric propulsion system architectures and performances, *Joint Conference of 30th International Symposium on Space Technology and Science, 34th International Electric Propulsion Conference, and 6th Nano-satellite Symposium*, Hyogo-Kobe, Japan, 2015.

[35] D. M. Goebel, I. Katz, *Fundamentals of electric propulsion: ion and Hall thrusters*, vol. 1, John Wiley & Sons, 2008.

[36] K. Alfriend, S. R. Vadali, P. Gurfil, J. How, L. Breger, *Spacecraft Formation Flying: Dynamics, Control and Navigation*, vol. 2, Elsevier, 2009.

[37] W. H. Clohessy, Terminal guidance system for satellite rendezvous, *Journal of the Aerospace Sciences*, vol. 27, no. 9, pp. 653-658, 1960.

[38] NASA Program Gemini Working Paper No. 5035, *Composite Air-to-Ground and Onboard Voice Tape Transmission of the GT-4 Mission*, NASA Manned Spacecraft Centre, Houston, Texas, pp. 11-13, 1965.

[39] B. C. Hacker, J. M. Grimwood, *On the Shoulders of Titans: A History of Project Gemini*, NASA SP-4203, 1977.

[40] G. B. Sholomitsky, O. F. Prilutsky, and V. G. Rodin, Infra-red space interferometer, *28th International Astronautical Federation Congress*, Prague, Czechoslovakia, IAF-77-68, 1977.

[41] A. Labeyrie, Stellar interferometry methods, *Annual Review of Astronomy and Astrophysics*, vol. 16, no. 1, pp. 77-102, 1978.

[42] K. Danzmann, LISA Study Team, LISA mission overview, *Advances in Space Research*, vol. 25, no. 6, IEEE, pp. 1129-1136, 2000.

[43] *Gravitational wave mission selected, planet-hunting mission moves forward*, Retrieved 11 September, 2018, from http://sci.esa.int/cosmic-vision/59243-gravitational-wave-mission-selected-planet-hunting-mission-moves-forward/

[44] M. Armano, H. Audley, G. Auger, J. Baird, M. Bassan, P. Binetruy, M. Born, D. Bortoluzzi, N. Brandt, M. Caleno, A. Cavalleri, LISA Pathfinder: First steps to observing gravitational waves from space, In *11th International LISA Symposium*, IOP Publishing, 2017.

[45] J. S. Llorente, A. Agenjo, C. Carrascosa, C. de Negueruela, A. Mestreau-Garreau, A. Cropp, A. Santovincenzo, PROBA-3: precise formation flying demonstration mission, *Acta Astronautica*, vol. 82, no. 1, pp. 38-46, 2013.

[46] M. G. Taylor, C. P. Escoubet, H. Laakso, A. Masson, M. Hapgood, T. Dimbylow, J. Volpp, S. Sangiorgi, M. L. Goldstein, The science of the Cluster mission, In *Magnetospheric Plasma Physics: The Impact of Jim Dungey's Research*, Springer, pp. 159-179, 2015.

[47] J. L. Burch, T. E. Moore, R. B Torbert, B. L. Giles, Magnetospheric Multiscale overview and science objectives, *Space Science Reviews*, vol. 199, no. 1-4, pp. 5-21, 2016.

[48] D. P. Scharf, F. Y. Hadaegh, S. R. Ploen, A survey of spacecraft formation flying guidance and control (part I): Guidance, In *Proceedings of the 2003 American Control Conference*, vol. 2, IEEE, pp. 1733-1739, 2003.

[49] D. P. Scharf, F. Y. Hadaegh, S. R. Ploen, A survey of spacecraft formation flying guidance and control (part II): Control, In *Proceedings of the 2004 American Control Conference*, vol. 4, IEEE, pp. 2976-2985, 2004.

[50] J. W. Cen, J. L. Xu, Performance evaluation and flow visualization of a MEMS based vaporizing liquid micro-thruster, *Acta Astronautica*, Vol. 67, No. 3-4, pp. 468-482, 2010.

[51] A. Natarajan, H. Schaub, Linear dynamics and stability analysis of a two-craft Coulomb tether formation, *Journal of Guidance, Control, and Dynamics*, Vol. 29, No. 4, pp. 831-839, 2006. doi: 10.2514/1.16480

[52] H. Schaub, I. I. Hussein, Stability and reconfiguration analysis of a circularly spinning two-craft Coulomb tether, *IEEE Transactions on Aerospace and Electronic Systems*, Vol. 46, No. 4, pp. 1675-1686, 2010. doi: 10.1109/AERO.2007.352670

[53] L. B. King, G. G. Parker, S. Deshmukh, J.-H. Chong, Study of interspacecraft Coulomb forces and implications for formation flying, *Journal of Propulsion and Power*, Vol. 19, No. 3, pp. 497-505, 2003. doi: 10.2514/2.6133

[54] H. Schaub, C. D. Hall, J. Berryman, Necessary conditions for circularly-restricted static Coulomb formations, *The Journal of the Astronautical Sciences*, Vol. 54, No. 3 & 4, pp. 525-541, 2006. doi: 10.1007/BF03256504

[55] D. J. Scheeres, F.-Y. Hsiao, N. X. Vinh, Stabilizing motion relative to an unstable orbit: applications to spacecraft formation flight, *Journal of Guidance, Control, and Dynamics*, Vol. 26, No. 1, 2003.

[56] F. Y. Hsiao, D. J. Scheeres, Design of spacecraft formation orbits relative to a stabilized trajectory, *Journal of Guidance, Control, and Dynamics*, Vol. 28, No. 4, 2005.

[57] D. Cielaszyk, B. Wie, New approach to halo orbit determination and control, *Journal of Guidance, Control, and Dynamics*, Vol. 19, No. 2, pp. 266-273, 1996.

[58] M. Bando, A. Ichikawa, Active formation flying along an elliptic orbit, *Journal of Guidance, Control, and Dynamics*, Vol. 36, No. 1, 2013. doi: 10.2514/1.57703

[59] C. S. Arnot, C. R. McInnes, Low thrust augmented spacecraft formation-flying for on-orbit inspection, *66th International Astronautical Congress*, IAC-15-C1.8.1.x28589, 2015.

[60] C. S. Arnot, C. R. McInnes, Low thrust augmented spacecraft formation-flying, *25th International Symposium on Space Flight Dynamics: ISSFD 2015*, Munich, Germany, 2015.

[61] C. S. Arnot, C. R. McInnes, R. J. McKay, M. Macdonald, J. Biggs, Orbit period modulation for relative motion using continuous low thrust in the two-body and restricted three-body problems, *Celestial Mechanics and Dynamical Astronomy*, vol. 130, no. 2, p. 12, 2018

[62] R. W. Farquhar, The control and use of libration-point satellites, PhD thesis, Stanford University, Stanford, California, 1968.

[63] K. C. Howell, Three-dimensional, periodic, 'halo' orbits, *Celestial Mechanics*, vol. 32, pp. 53-71, 1984.

[64] D. L. Richardson, Halo orbit formulation for the ISEE-3 mission, *Journal of Guidance, Control, and Dynamics*, vol. 3, no. 6, pp. 543-548, 1980.

[65] E. W. Brown, On a new family of periodic orbits in the problem of three bodies: (plates 6, 7.), *Monthly Notices of the Royal Astronomical Society*, vol. 71, no. 5, pp. 438-454, 1911.

[66] E. Rabe, Determination and survey of periodic trojan orbits in the restricted problem of three bodies, *The Astronomical Journal*, vol. 66, no. 9, pp. 500-513, 1961.

[67] B. Garfinkel, Theory of the Trojan asteroids Part I, *The Astronomical Journal*, vol. 82, pp. 368-379, 1977.

[68] S. P. Synnott, C. F. Peters, B. A. Smith, L. A. Morabito, Orbits of the small satellites of Saturn, *Science*, vol. 212, no. 4491, p. 191, 1981.

[69] E. C. Stone, E. D. Miner, Voyager 1 encounter with the Saturnian system, *Science*, vol. 212, no. 4491, pp. 159-163, 1981.

[70] B. A. Smith, L. Soderblom, R. Beebe, J. Boyce, G. Briggs, A. Bunker, S. A. Collins, C. J. Hansen, T. V. Johnson, J. L. Mitchell, and others, Encounter with Saturn: Voyager 1 imaging science results, *Science*, vol. 212, no. 4491, pp. 163-191, 1981.

[71] S. F. Dermott, C. D. Murray, The dynamics of tadpole and horseshoe orbits: I. Theory, *Icarus*, vol. 48, no. 1, pp. 1-11, 1981.

[72] S. F. Dermott, C. D. Murray, The dynamics of tadpole and horseshoe orbits: II. The coorbital satellites of Saturn, *Icarus*, vol. 48, no. 1, pp. 12-22, 1981.

[73] A. Deprit and J. Henrard, Natural families of periodic orbits, *The Astronomical Journal*, vol. 72, pp. 158-172, 1967.

[74] D. Taylor, Horseshoe periodic orbits in the restricted problem of thee bodies for a Sun-Jupiter mass ratio, *Astronomy and Astrophysics*, vol. 103, pp. 288-294, 1981.

[75] A. F. Schanzle, Horseshoe-shaped orbits in the Jupiter-Sun restricted problem, *The Astronomical Journal*, vol. 72, p. 149, 1967.

[76] R. A. Broucke, Motion near the unit circle in the three-body problem, in *International Astronomical Union Colloquium*, vol. 172, 281290, 1999.

[77] C. S. Arnot, C. R. McInnes, Artificial horseshoe orbits using low thrust propulsion, *67th International Astronautical Congress*, IAC-16-C1.1.2x34607, 2016.

[78] K. Woellert, P. Ehrenfreund, A. J. Ricco, H. Hertzfeld, Cubesats: Cost-effective science and technology platforms for emerging and developing nations, *Advances in Space Research*, vol. 47, no. 4, pp. 663-684, 2011.

[79] N. H. Crisp, K. Smith, P. Hollingsworth, Launch and deployment of distributed small satellite systems, *Acta Astronautica*, vol. 114, pp. 65-78, 2015.

[80] J. R. London III, M. E. Ray, D. J. Weeks, A. B. Marley, The first US army satellite in fifty years: SMDC-ONE first flight results, in *The 25th Annual AIAA/USU Conference on Small Satellites*, American Institute of Aeronautics and Astronautics (AIAA), Logan, Utah, 2011.

[81] F. M. Pranajaya, R. E. Zee, Nanosatellite tracking ships: from concept to launch in 7 months, in *23rd Annual AIAA/USU Conference on Small Satellites*, American Institute of Aeronautics and Astronautics (AIAA), Logan, Utah, pp. 1-6, 2009.

[82] S. Kenyon, C. P. Bridges, STRaND-1: use of a $500 smartphone as the central avionics of a nanosatellite, in *The 62nd International Astronautical Congress*, International Astronautical Federation (IAF), Cape Town, South Africa, 2011.

[83] S. Kim, T. Eishima, N. Miyashita, Y. Nojiri, Y. Nakamura, WNISAT-nanosatellite for north arctic routes and atmosphere monitoring, in *The 24th Annual AIAA/USU Conference on Small Satellites*, American Institute of Aeronautics and Astronautics (AIAA), Logan, Utah, 2010.

[84] C. R. Boshuizen, J. Mason, P. Klupar, S. Spanhake, Results from the Planet Labs Flock constellation, in *The 28th Annual AIAA/USU Conference on Small Satellites*, American Institute of Aeronautics and Astronautics (AIAA), Logan, Utah, 2014.

[85] *Sky and Space Global Details Vision for 200 Satellite LEO Network*, Retrieved 13 September, 2018, from https://www.satellitetoday.com/telecom/2016/07/26/sky-space-global-details-vision-200-satellite-leo-network/

[86] B. E. Tweddle, A. Saenz-Otero, Relative computer vision-based navigation for small inspection spacecraft, *Journal of Guidance, Control, and Dynamics*, vol. 38, no. 5, pp. 969-978, 2014.

[87] F. Sansone, F. Branz, A. Francesconi, A relative navigation sensor for CubeSats based on retro-reflective markers, *2017 IEEE International Workshop on Metrology for AeroSpace*, IEEE, Padua, Italy, 2017.

[88] NASA Goddard Space Flight Centre, On-Orbit Satellite Servicing Study Project Report, NASA Project Report NP-2010-08-162-GSFC, Greenbelt, Maryland, 2010.

[89] D. C. Woffinden, On-orbit satellite inspection, MSc thesis, Massachusetts Institute of Technology, Cambridge, Massachusetts, 2004.

[90] K. Lee, H. Oh, H. E. Park, S. Y. Park, C. Park, Laser-based relative navigation using GPS measurements for spacecraft formation flying, *Journal of Astronomy and Space Sciences*, vol. 32, no. 4, pp. 387-393, 2015.

[91] A. Renga, M. Grassi, U. Tancredi, Relative navigation in LEO by carrier-phase differential GPS with intersatellite ranging augmentation, *International Journal of Aerospace Engineering*, 2013.

[92] M. T. Erdner, Smaller satellite operations near geostationary orbit, MSc thesis, Naval Postgraduate School, Monterey, California, 2007.

[93] C. S. Arnot, C. R. McInnes, Thrust-augmented horseshoe orbits in the circular restricted three-body problem, Submitted to*Celestial Mechanics and Dynamical Astronomy*, May 2018.

[94] M. Bando, A. Ichikawa, Formation flying near the libration points in the elliptic restricted three-body problem, *5th International Conference on Spacecraft Formation Flying Missions and Trajectories*, Munich, Germany, 2013.

[95] K. Tanaka, J. Kawaguchi, Small-amplitude periodic orbit around Sun-Earth L1/L2 controlled by solar radiation pressure, *Transactions of the Japan Society for Aeronautical and Space Sciences*, Vol. 59, No. 1, 2016.

[96] S. Baig, Non-Keplerian orbits for low-thrust propulsion, PhD thesis, Department of Mechanical Engineering, University of Strathclyde, 2009.

[97] R. Broucke, A. Konopoliv, Some models for the motion of the co-orbital satellites of Saturn, In *Long-Term Dynamical Behaviour of Natural and Artificial N-Body Systems*, Springer, pp. 155-169, 1988.

[98] C. R. McInnes, Autonomous ring formation for a planar constellation of satellites, *Journal of Guidance, Control, and Dynamics*, vol. 18, no. 5, pp. 1215-1217, 1995.

[99] G. Mushet, G. Mingotti, C. Colombo, and C. McInnes, Self-organising satellite constellation in geostationary earth orbit, *IEEE Transactions on Aerospace and Electronic Systems*, vol. 51, no. 2, pp. 910-923, 2015.

[100] A. E. Roy, *Orbital Motion*, CRC Press, 2004.

[101] B. Garfinkel, Theory of the Trojan asteroids, *Celestial Mechanics*, vol. 22, no. 3, pp. 267-287, 1980.

[102] B. Garfinkel, Theory of the Trojan asteroids Part II, *Celestial Mechanics*, vol. 18, no. 3, pp. 259-275, 1978.

[103] A. A. Christou, A numerical survey of transient co-orbitals of the terrestrial planets, *Icarus*, vol. 144, no. 1, pp. 1-20, 2000.

[104] U. Walter, *Astronautics: the physics of space flight*, John Wiley & Sons, 2012

[105] M. H. M. Morais, A. Morbidelli, The population of near-Earth asteroids in coorbital motion with the Earth, *Icarus*, vol. 160, no. 1, pp. 1-9, 2002.

[106] M. H. M. Morais, A. Morbidelli, The population of near-Earth asteroids in coorbital motion with Venus, *Icarus*, vol. 185, no. 1, pp. 29-38, 2006.

[107] P. Robutel, A. Pousse, On the co-orbital motion of two planets in quasi-circular orbits, *Celestial Mechanics and Dynamical Astronomy*, vol. 117, no. 1, pp. 17-40, 2013.

[108] C. A. Giuppone, C. Beugé, T. A. Michtchenko, S. Ferraz-Mello, Dynamics of two planets in co-orbital motion, *Monthly notices of the Royal Astronomical Society*, vol. 407, no. 1, pp. 390-398, 2010.

[109] G. Bonin, N. Roth, S. Armitage, J. Newman, B. Risi, R. E. Zee, CanX-4 and CanX-5 precision formation flight: Mission accomplished! *29th Annual AIAA/USU Conference on Small Satellites*, SSC15-I-4, 2015.

[110] W.E. Wiesel, *Spaceflight Dynamics*, McGraw-Hill, 1997.

[111] V. Szebehely, *Theory of orbits: The restricted problem of three bodies*, Academic Press, 1967.

[112] S. F. Dermott, T. Gold, A. T. Sinclair, The rings of Uranus: Nature and origin, *Astronomy Journal*, vol. 84, pp. 1225-1234, 1979.

[113] S. F. Dermott, C. D. Murray, A. T. Sinclair, The narrow rings of Jupiter, Saturn and Uranus, *Nature*, vol. 284, pp. 309-313, 1980.

[114] V. Domingo, B. Fleck, A. I. Poland, SOHO: the solar and heliospheric observatory, *Space Science Reviews*, vol. 72, no. 1-2, pp. 81-84, 1995.

[115] E. C. Stone, A. M. Frandsen, R. A. Mewaldt, E. R. Christian, D. Margolies, J. F. Ormes, F. Snow, The advanced composition explorer, *Space Science Reviews*, vol. 86, no. 1-4, pp. 1-22, 1998.

[116] T. A. Collard, J. P. Sheehan, A. D. Gallimore, Pressurized Xenon propellant management system for the CubeSat Ambipolar Thruster, *Joint Conference*

of 30th International Symposium on Space Technology and Science, 34th International Electric Propulsion Conference and 6th Nano-satellite Symposium, Hyogo-Kobe, Japan, 2015.

[117] S. W. Evans, Natural environment near the Sun/Earth-Moon L2 libration point, *Next Generation Space Telescope Program*, NASA Marshall Space Flight Center (MSFC), AL, 2002.

[118] C. R. Chapman, The Galileo encounters with Gaspra and Ida, In *Asteroids, Comets, Meteors 1993*, IAU Symposium, vol. 160, p. 357, 1994.

[119] J.-M. Petit, D. D. Durda, R. Greenberg, T. Hurford, P. Geissler, The long-term dynamics of Dactyl's orbit, *Icarus*, vol. 130, no. 1, pp. 177-197, 1997.

[120] M. J. Belton, C. R. Chapman, K. P. Klaasen, A. P. Harch, P. C. Thomas, J. Veverka, A. S. McEwen, R. T. Pappalardo, Galileo's encounter with 243 Ida: An overview of the imaging experiment, *Icarus*, vol. 120, no. 1, pp. 1-19, 1996.

[121] Z. Ceplecha, P. Brown, R. L. Hawkes, G. Wetherill, M. Beech, K. Mossman, Video observations of the Peekskill meteorite fireball: Atmospheric trajectory and orbit, *Meteoritics*, vol. 29, p. 455, 1994.

[122] C. R. Chapman, S-type asteroids, ordinary Chondrites, and space weathering: The evidence from Galileo's fly-bys of Gaspra and Ida, *Meteoritics & Planetary Science*, vol. 31, no. 6, pp. 699-725, 1996.

[123] U. M Ascher, R. M. Mattheij, R. D. Russell, *Numerical solution of boundary value problems for ordinary differential equations*, vol. 13, Siam, 1994.

[124] Numerical solution of boundary value problems, http://reference.wolfram.com/language/tutorial/NDSolveBVP.html, accessed: 29/03/2018

[125] B.-G. June, Poincaré and the three body problem, *American Mathematical Society*, vol. 2, 1997.

[126] W. L. Brogan, *Modern control theory*, Pearson Education India, 1982.

[127] R. Zappulla, J. Virgili-Llop, M. Romano, Spacecraft thruster control via sigma-delta modulation, *Journal of Guidance, Control, and Dynamics*, vol. 40, pp. 2928-2933, 2017.

[128] A. D. Challoner, R. L. Poeschel, Spacecraft with modulated thrust electrostatic ion thruster and associated method, US Patent 4,825,646, 02/05/1989.

[129] J. R. Beattie, Electrostatic ion thruster with improved thrust modulation, US Patent 4,838,021, 13/06/2017.

[130] R. L. Burton, P. J. Turchi, Pulsed plasma thruster, *Journal of Propulsion and Power*, vol. 14, no. 5, pp. 716-735, 1998.

[131] N. G. Orr, J. Eyer, B. Larouche, and R. Zee, Precision formation flight: the CanX-4 and CanX-5 dual nanosatellite mission, In *4S Symposium Small Satellites Systems and Services*, vol. 660, 2008.

[132] C. P. Bridges, B. Taylor, N. Horri, C. I. Underwood, S. Kenyon, J. Barrerra-Ars, L. Pryce, R. Bird, STRaND-2: Visual inspection, proximity operations & nanosatellite docking, In *Aerospace Conference, 2013 IEEE*, IEEE, pp. 1-8, 2013.

[133] F. Torre, R. Serra, S. Grey, M. L. Vasile, Angles-only navigation of a formation in the proximity of a binary system, *2018 Space Flight Mechanics Meeting*, AIAA SciTech Forum, Kissimmee, Florida, 2018.